

**Femtosecond Laser Fabricated Moth-eye Structures
for Antireflection in Terahertz Region**

**フェムト秒レーザー加工による
テラヘルツ帯モスアイ型反射防止構造**

2021

YU Xi

**Femtosecond Laser Fabricated Moth-eye Structures
for Antireflection in Terahertz Region**

**フェムト秒レーザー加工による
テラヘルツ帯モスアイ型反射防止構造**

A dissertation submitted to the Department of Physical Science and Engineering

NAGOYA INSTITUTE OF TECHNOLOGY

in partial fulfillment of the requirements for the degree of

DOCTOR OF PHILOSOPHY IN ENGINEERING

BY

2021

YU Xi

To my parents, wife, and son.

Abstract

Terahertz (THz) radiation (0.1–10 THz) has been researched for applications in a wide range of fields, including communications, security, food inspection, and biomedical diagnosis. Most materials for THz components have relatively high refractive indices leading to a sudden refractive change when THz waves propagating from air to THz components. This mismatch of refractive index in the interface will result in non-negligible reflection loss. For example, high-resistivity silicon (Si) has a refractive index of 3.42, and almost 30% of the power will be reflected when THz waves propagate from air to Si substrate surface in a normal incident. This undesired reflection loss limits the use of THz technology in many applications. Consequently, reducing reflection loss is a key aspect of improving the performance of THz systems. Antireflective (AR) coatings have been used to reduce reflection at the air–substrate interface. Today, the most widely used AR coating is the quarter-wavelength coating made of just a single layer, which is easy to fabricate. However, they are only effective for a narrow frequency band. Multilayer coatings are efficient for preventing reflection over a broader frequency band, but the thicker coating can render the absorption non-negligible, and materials with a refractive index suitable for THz radiation are less common. Alternatively, subwavelength surface-relief structures, known as moth-eye structures, can be used to reduce Fresnel reflection loss over a broad frequency band. For fabricating such moth-eye structures in the THz region, machining, etching, laser processing-based methods have been proposed and reported for several years. Benefitting from the simplicity, processing efficiency, and flexibility, ultrafast lasers processing was employed to fabricate moth-eye structures on actual THz applications, such as THz lens and THz generators. Although it seems no technical barrier to fabricating a moth-eye structure for THz waves, the practical uses of moth-eye structures are still limited by its weak mechanical stability. This dissertation focuses on the development of the moth-eye and related AR structures for the antireflection in the THz region and aiming at achieving a high-performance stable AR structure for the actual applications.

Fabricating the micro tapers of moth-eye structure with a special profile may increase the mechanical stability. Moreover, beyond the concept of alleviating the

sudden refractive index change in the interface of air and THz components, the changing pattern of effective refractive index (n_{eff}) can also affect the AR characteristic, which can be controlled by adjusting the profile (fill fraction of substrate material) of such micro tapers. Femtosecond (10^{-15} s) laser processing is outstanding for precision processing. Benefitting from the ultrashort pulse duration in femtosecond order, the heat-affected zone will be suppressed during laser ablation resulting in a neat surface. Due to such machining accuracy, the femtosecond laser has been widely used for the research of micro-and nano-machining on surface modification. Additionally, its exemplary processing efficiency keeps increasing with the development of the high power femtosecond laser.

First of all, to realize the moth-eye structure in THz region, a femtosecond laser processing system was built for the fabricating such structures. Thermal influence during laser processing on a high-resistivity Si substrate was studied, and neat moth-eye structures with different pitches and aspect ratios were successfully fabricated. Both samples showed AR characteristic in a broadband from 0.1 to 2.5 THz, and the power reflectance can be reduced to almost 0 for some specific frequencies. Simultaneously, simulation results showed that the profile of the micro tapers has a strong influence on the AR characteristic of moth-eye structures. **(Related Paper [1])**

Improving the diversification of THz light sources is important for promoting the applications of THz waves in daily life. Such femtosecond laser fabricated moth-eye structure was applied to improve the output of a THz generator which is designed to meet the needs of developing a compact and high-power coherent THz wave source. This THz generator consists of a one-dimensional array of photoconductive antennas on a low-temperature-grown Gallium Arsenide (GaAs) substrate. By fabricating the moth-eye structures on the reverse of the antenna substrate, this THz generator had a 2.5-4.4 times improvement of the output at the theoretical and experimental output frequencies comparing to that of the generator without moth-eye structure. Zinc oxide (ZnO) is also a potential material for THz generator, which has a high refractive index of more than 2.8 in the THz region. Consequently, we fabricated the moth-eye structures on ZnO substrates to reduce the high reflection loss. The AR characteristics of ZnO moth-eye structure are not as good as that of Si or GaAs. The surface of ZnO substrates may be modified under the high-temperature high-pressure condition in the focused laser spot during laser ablation. Such surface modification can affect the

surface defect and consequently increase the absorption of THz waves. The formation and changing of surface defects during laser processing on ZnO substrate were studied in detail, and annealing was performed for these ZnO moth-eye structures to eliminate such undesired defects. Finally, it was demonstrated that the AR performance can be improved by annealing these structures in the air. Moreover, peculiar laser-induced surface cleavage on the ZnO surface was observed and discussed with a 3-photon absorption model. **(Related Proceedings [1] and Paper [2])**

To further improve the performance and characterize the shape dependence, moth-eye structures that comprise periodically arranged tapers with varying sizes and profiles (triangle, parabola, stair, and triangle–stair) were fabricated using femtosecond laser ablation via a fine adjustment of the processing pattern. The profile dependence of the AR characteristics was experimentally proven, and an index to describe the refractive index changes along with the taper height ($\Sigma[n'/n]$) was proposed to evaluate the total power reflectance in a broad THz band: a profile with lower $\Sigma[n'/n]$ will result in a lower total power reflectance. Likewise, both samples showed broadband AR characteristics in the range of 0.1-1 THz, which may be useful for the next generation of mobile communication. The stair profile samples showed the lowest $\Sigma[n'/n]$ and the most stable AR distribution without fluctuating for the broadband region from 0.5-1.0 THz, which also has a flat top of the taper with a relatively higher mechanical stability than that of other samples. **(Related Paper [3])**

Finally, for improving the mechanical stability of moth-eye structures, we proposed a polymer-coated moth-eye hybrid structure, which was made by attaching a polymer-based two-layer coating onto a moth-eye structure on a silicon substrate. The flat cleanable surface inherited from the coating can work as an AR coating for reducing the reflection and a shield for protecting the moth-eye structure. Consequently, this hybrid AR structure can greatly improve the practical applicability of the moth-eye structure. This hybrid AR structure also has excellent AR characteristics due to the quarter-wavelength coating effect in the first polymer layer and the graded-index features in the polymer-filled moth-eye layer. The measured power reflectance of this hybrid ARS remained less than 6% for frequencies from 0.6 to 2.5 THz and corresponded to the simulated transmittance. The total power reflectance from 0.1 to 2.5 THz was reduced to 20% of the unprocessed Si surface. This high-transmittance

and cleanable flat AR surface should be useful for a lot of THz components in actual applications. **(Related Paper [4])**

This dissertation described the establishment of a method for fabricating the moth-eye structures by using femtosecond laser processing for antireflection in the THz region. The femtosecond laser ablated moth-eye structure was successfully applied to a THz generator and achieved a good performance at improving its output. Moreover, an index for the AR performance of moth-eye structures was proposed and quantitatively analyzed based on the experiment and simulation results, which can be an important reference for the design of moth-eye structures for various applications. At last, a polymer-coated moth-eye hybrid structure with a flat surface was proposed to reduce the reflection loss and simultaneously improve the mechanical stability. High-performance in a super broadband THz region was proved by experiments and simulations for this hybrid AR structure. This work can not only promote the practical application of THz but also contribute to ultrafast laser precision processing technology.

Related Paper

[1] **Xi Yu**, Michiharu Ohta, Nobuhito Takizawa, Kazuhisa Mikame, Shingo Ono, and Jongsuck Bae, “Femtosecond-laser-fabricated periodic tapered structures on a silicon substrate for terahertz antireflection”, *Applied Optics* **58**, 9595(2019)
DOI: 10.1364/AO.58.009595

[2] **Xi Yu**, Fumihito Itoigawa, Shingo Ono, “Femtosecond laser-pulse-induced surface cleavage of zinc oxide substrate”, *Micromachines* **12**, 596(2021)
DOI: 10.3390/mi12060596

[3] **Xi Yu**, Yuki Yasunaga, Kazusa Goto, Dejun Liu, Shingo Ono, “Profile control of femtosecond laser-fabricated moth-eye structures on Si substrate”, *Optics and Lasers in Engineering* **142**, 106584(2021)
DOI: 10.1016/j.optlaseng.2021.106584

[4] **Xi Yu**, Kazusa Goto, Yuki Yasunaga, Junshi Soeda, Shingo Ono, “Polymer-coated moth-eye hybrid structure for broadband antireflection in the terahertz region”, *Optics Letters*, under review
DOI:

Related Proceedings

[1] **Xi Yu**, Shingo Ono, Jongsuck Bae, “Application of laser generated moth-eye structure for a periodic terahertz-wave generator”, *Proceedings of International Conference on Infrared, Millimeter, and Terahertz Waves 2019*, **Tu-Po2-37**, September 2019, Paris, France
DOI: 10.1109/IRMMW-THz.2019.8874269

Table of contents

Chapter 1 Background and motivation

1.1 THz waves	1
1.2 Reflection loss and antireflection strategies	2
1.3 Motivation	3
1.4 Thesis overview	3

Chapter 2 Realization of moth-eye structure by using femtosecond laser processing

2.1 Theoretical computation	5
2.2 Fabrication of moth-eye structures	7
2.3 AR characteristics based on the THz-TDS measurement	10
2.4 Conclusions	15

Chapter 3 Application of moth-eye structures for THz generators

3.1 Introduction	16
3.2 Periodic terahertz-wave generator on LT-GaAs substrate	16
3.2.1 Introduction	16
3.2.2 Experiment and results	16
3.2.3 Conclusions (GaAs-based moth-eye structure)	19
3.3 Femtosecond-laser-induced cleavage on a zinc oxide substrate	20
3.3.1 Introduction	20
3.3.2 Experimental details	22
3.3.3 Results and discussion	23
3.3.4 Conclusions (ZnO-based moth-eye structure)	33
3.4 Conclusions	34

Chapter 4 Profile control of moth-eye structures

4.1 Introduction	35
4.2 Material and Methods	35

4.2.1 Fabrication of moth-eye structures.....	35
4.2.2 Evaluation of the moth-eye structures.....	38
4.3 Results and discussion	41
4.4 Conclusions.....	45
Chapter 5 Polymer-coated moth-eye hybrid ARS	
5.1 Introduction.....	46
5.2 Experiment and results	47
5.3 Conclusion	50
Chapter 6 Conclusions and future perspectives	
6.1 Conclusion	52
6.2 Future perspectives.....	52
References	54
Acknowledgements	61
Publication List	62
Awards and Funding	66

Chapter 1

Background and Motivation

1.1 THz Waves

Terahertz (THz) radiation (typically, 0.1–10 THz), with the spectrum located between the well-developed microwave region and the visible light region, was historically known as the “THz gap” because of the difficulties for its generating and detecting (Figure. 1.1)[1–3]. However, THz technologies have been greatly promoted benefitting from the development of ultrafast optics and semiconductor technology since the 1980s[4,5]. The low-energy (compared to visible optics), non-ionizing, penetration for most non-conductive materials, and higher frequencies features made the THz waves suitable to realize a wide range of applications, such as molecular spectroscopy[6–9], security[10], diagnostic imaging[11–18], high-speed broadband communication[19–23], astronomical observation[24] and so on. Due to such functional applications, documents containing “terahertz” in the abstract, title, or keywords doubles every 3.23 years from 1975 to 2013, and more than 3000 such documents were published in 2013[25]. Since 2014, more than thousands of conference publications containing the keyword of “terahertz” have been reported every year. Figure 1.2 shows the number of journal articles containing “terahertz” in their titles, which are published by the main publisher of academic journals from 2014 (according to the search engine of each publisher from their homepage). This number has exceeded 1000 from 2015 and increased to 1500 in 2020.

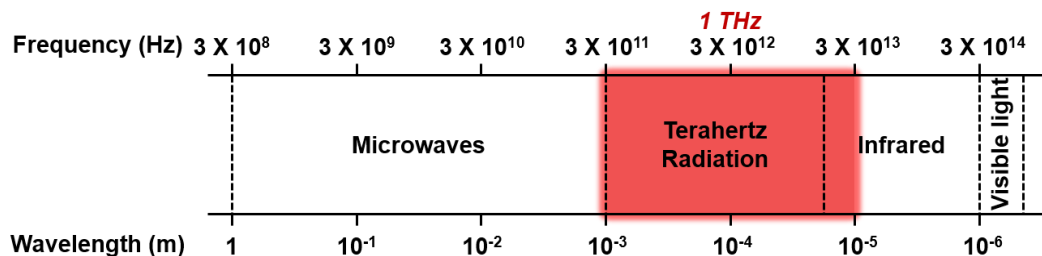


Figure 1.1. location of THz waves as electromagnetic waves.

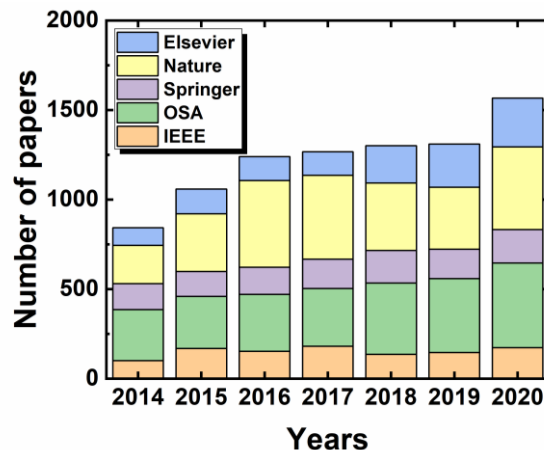


Figure 1.2. the number of journal articles containing “terahertz” from 2014 to 2020.

1.2 Reflection loss and antireflection strategies

Despite the full of vigor, the applications of THz waves have been hindered by the lack of a tabletop THz generation system[26,27], and THz applications remain out of reach in daily life. Moreover, the high reflection loss of power from THz components will make the matters worse. Most materials for THz components have relatively high refractive indices leading to a sudden refractive change when THz waves propagating from air to THz components. This mismatch of refractive index in the interface will result in non-negligible reflection loss. For example, high-resistivity silicon (Si) has a refractive index of 3.42, and almost 30% of the power will be reflected when THz waves propagate from air to Si substrate at a normal incidence. This undesired reflection loss limits the use of THz technology in many applications. Table 1.1 shows the refractive indices and the power reflectance of materials generally used in the THz region[28–33]. The power reflectance was calculated amusing that the THz waves were propagating from air to the THz components at a normal incidence. Consequently, reducing reflection loss is a key aspect of improving the performance of THz systems.

Table 1.1 Refractive indices and power reflectance (normal incidence) of materials generally used in the THz region.

Material	Refractive index @ 1 THz	Power reflectance
LiNbO ₃	6.72	54.9%
GaAs	3.63	32.3%
Si	3.42	30.0%
Sapphire	3.07	25.9%
SiO ₂	2	11.1%
PTFE	1.43	3.1%

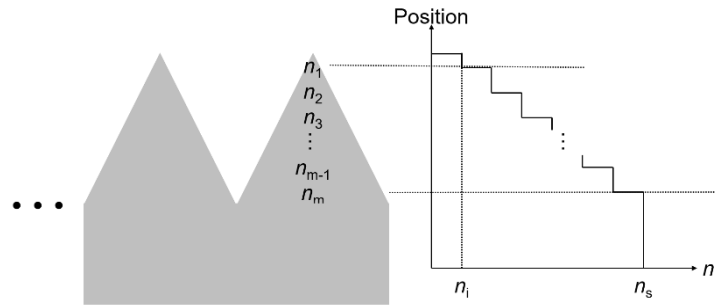


Figure 1.3 profile image of moth-eye structures and its effective refractive index distribution. n_m is the effective refractive index, and subscript is the layer number. n_i is the refractive index of the atmosphere and n_s is the refractive index of the substrate.

AR coatings have been used to reduce reflection at the air–substrate interface. Lord Rayleigh was the first to discover a thin film AR coating when he observed the improvement in transmittance that was gained by tarnishing the surface of the glass; he also investigated how reflectance is affected by the incident wavelength and the effective layer thickness[34]. Today, the most widely used AR coating is the quarter-wavelength coating, which consists of a single layer on a substrate. Although these coatings are easy to fabricate, they are only effective for signals in a narrow frequency band[35–37]. Multilayer coatings are efficient for preventing reflection over a broader frequency band[38], but the thicker coating can render the absorption. Alternatively, subwavelength surface-relief structures, also known as moth-eye structures, can be used

to reduce Fresnel reflection loss over a broad frequency band[39,40]. The sub-wavelength structure comprises countless periodically arranged protuberances that resemble the compound eyes of moths, thus the term moth-eye structure[41,42]. The moth-eye structures also can be considered as an AR coating with infinite layers, and the effective refractive index of each layer is related to the fill fraction of the substrate material. Figure 1.3 shows a sectional image of the moth-eye structure, the effective refractive index changes gradually from the tapered top to the bottom, which connects the condition medium and substrate. Due to this, the moth-eye structure can also be called graded-index structures. Moreover, the moth-eye structures can suit any spectral range when the period of tapers is adjusted to be smaller than the wavelength of incident waves thus enhance the zero-order diffraction[40], and finally improve the intensity of the transmitted signal. For fabricating such moth-eye structures, several methods based on machining[43–45], etching[46–49], and laser processing[50–56] have been reported. Benefitting from the simplicity, processing efficiency, and flexibility, ultrafast laser processing was employed to fabricate moth-eye structures on actual THz applications, such as lens[51] and THz generators[53,57].

1.3 Motivation

Although it seems no technical barrier to fabricating a moth-eye structure for THz waves, the practical uses of moth-eye structures are still limited by weak mechanical stability[51,58]. Fabricating the micro tapers of moth-eye structure with a special profile may increase the mechanical stability[59–61], but the brittle microstructures make the AR structure (ARS) difficult to be cleaned[62]. The motivation of this study is to develop broadband THz-ARSs with high AR performance and high mechanical stability, which can be used to promote the actual applications of THz waves.

1.4 Thesis overview

The organization of this thesis is as follows and shown as an image in Figure 1.4.

Chapter 1 briefly introduces the THz waves and their applications. The reflection loss which has hindered the actual applications of THz devices in daily life is also introduced with conventional antireflection strategies. Moreover, the motivation and organization of this thesis are also described in chapter 1.

Chapter 2 describes the realization of moth-eye structure by using femtosecond laser processing. A processing system was built for the fabrication of moth-eye structures in the THz region. Thermal influence during laser processing on a high-resistivity Si substrate was studied, and neat moth-eye structures with different pitches and aspect ratios were successfully fabricated. The evaluation method based on a terahertz time-domain spectroscopy (THz-TDS) was established.

Chapter 3 introduces the applications of moth-eye structures to improve the output of a THz generator which is designed to meet the needs of developing a compact and high-power coherent THz wave source. This THz generator consists of a one-dimensional array of photoconductive antennas on a low-temperature-grown Gallium arsenide (GaAs) substrate. The challenge to the antireflection of Zinc Oxide (ZnO) substrate is also performed because ZnO is also a potential material for THz generators. Results of ZnO are not as good as desired, but the possible cause for the undesired results was discussed with the formation of defects on the laser-irradiated spots. Moreover, laser processing physics about this wide-bandgap material was also

discussed with a multi-photon absorption model. Although without any post-processing, the laser-fabricated ZnO moth-eye structures did not achieve the desired AR performance, it was demonstrated that the AR performance can be improved by annealing such structures in the air.

Chapter 4 introduces further work for controlling the effective refractive index of moth-eye structures, which is aiming at the control of AR characteristics to improve their performance. Micro tapers with special profiles should have higher AR performance and mechanical stability than that of single-line laser-scanned moth-eye structures. An index was proposed to evaluate the total power reflectance in a broad THz band, and this index should be an important reference for the design of AR structures in the THz region.

Chapter 5 proposed a polymer-coated moth-eye structure with high AR performance and high mechanical stability. This hybrid ARS was made by attaching a polymer-based two-layer coating onto a moth-eye structure on a silicon substrate. This high-transmittance and cleanable flat antireflective (AR) surface should be useful for a lot of THz components in actual applications, such as the THz lens and generators.

Chapter 6 is the summary of this thesis. Future perspectives of moth-eye structures are also discussed in this chapter.

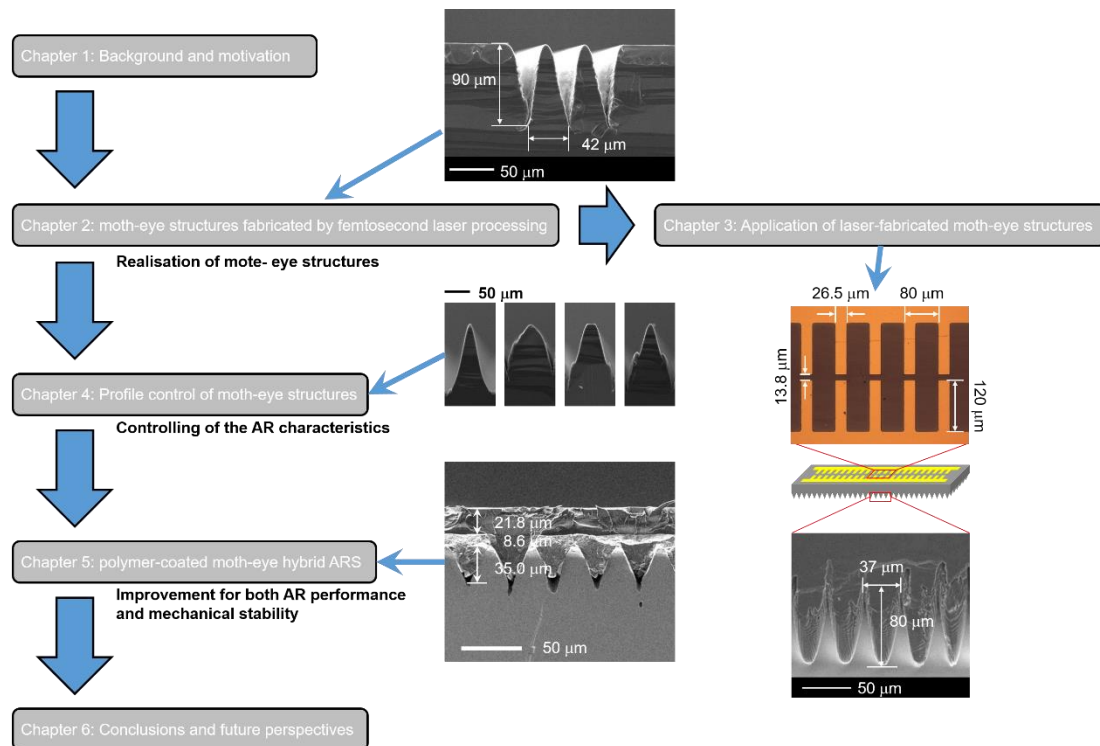


Figure. 1.4. the organization of this thesis.

Chapter 2

Realization of moth-eye structure by using femtosecond laser processing

2.1 Theoretical computation

First of all, we need to realize such periodically arranged micro tapers, and before the fabrication, theoretical computations were performed by using a high-frequency electromagnetic field simulation (HFSS) in advance. For periodic tapered structures to work as a diffraction grating, the pitch must be sufficiently small to enhance the zero-order diffraction[48,49,51]. At normal incidence, the pitch is defined as

$$p = \frac{\lambda_{min}}{n_{si}} \quad (2-1)$$

where p is the pitch of the taper, λ_{min} is the minimum wavelength in the AR region, and n_{si} is the refractive index of Si. For frequencies of 0.1–3 THz, the corresponding pitch is approximately 30 μm , which is a typical size for ultrashort-pulse laser processing. Deeper structures are generally considered to be better, due to their more favorable aspect ratio (h/p , where h is the depth of the taper)[44,47]. The profile of the taper is also important. Compared with a rectangular profile, a tapered profile results in a smoother change in the effective refractive index. Using electromagnetic simulations in ANSYS HFSS software, we theoretically predicted the AR characteristics of tapered moth-eye structures with different profiles (linear[63], exponential[64–66], and Klopfenstein[65–67]) in the THz range. Table 2.1 presents the details for the simulation conditions.

Table 2.1 Simulation Conditions.

Analysis Software	ANSYS HFSS
Port type	Floquet port
Boundary condition	Periodic boundary
Step size	0.01 THz
Frequency range	0.1-2.5 THz
Pitch(p)	35 μm
Materials	Si(3.42), vacuum

Figures 2.1-2.3 illustrate our simulation results. Figure 2.1 (a) shows three different refractive index distributions, displaying how the refractive indices change with the normalized position. Figure 2.1 (b) shows HFSS models based on the refractive index distributions shown in Figure 2.1 (a). Effective refractive indices are determined by changing the fill fraction for each position, and their differences result in variable profiles of taper. Figure 2.2 shows the calculated power reflectance of these three tapered structures for different frequencies. The tapers were attached to a 1 μm thick Si substrate to avoid using an inhomogeneous material for the Floquet port. The first power reflectance minimum is observed at approximately 0.72 THz for exponential taper, which is lower than that of the Klopfenstein taper.

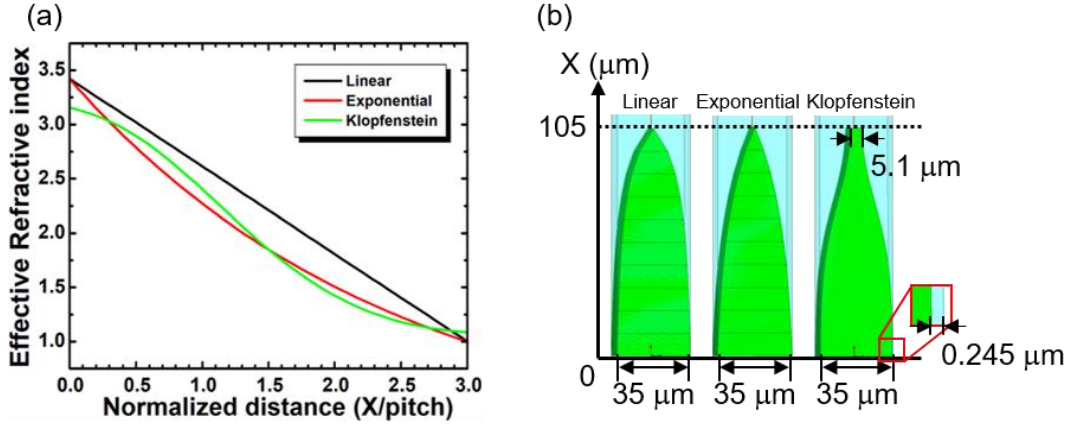


Figure 2.1. (a) Effective refractive index plotted against the normalized distance. X is the position from the bottom to the top of the tapered structure shown in Figure 2.1 (b); the width of models is set as $35 \mu\text{m}$. The Klopfenstein taper has a $5.1 \mu\text{m}$ flat top and $0.245 \mu\text{m}$ gap at the wings on the bottom. (b) HFSS models of tapers with different profiles. These tapers have a depth of $105 \mu\text{m}$ with an aspect ratio of 3. Terahertz waves were irradiated from vacuum to Si substrate (top to the bottom in this simulation).

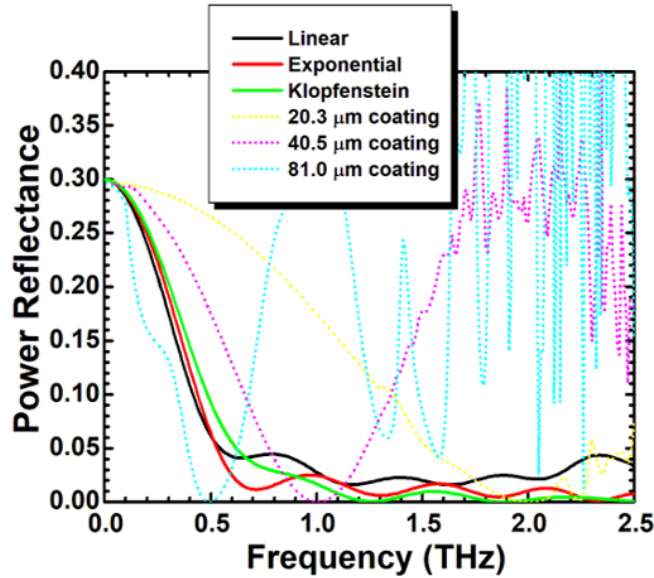


Figure 2.2. Power reflectance of all three tapered structures is reduced to almost zero but exhibits different frequency dependences. Compared with the $\lambda/4$ coating, the moth-eye structures have broader AR bands.

After the first minimum value is reached, the Klopfenstein taper offers the lowest, most stable reflectance curve with the weakest ripples. For these three tapers, the power reflectance is more strongly suppressed at higher frequencies. When the wavelength is sufficiently long, the surface can be considered as a flat surface. In contrast, at higher frequencies, the wavelength becomes shorter than the pitch, which enhances the multireflection of the THz wave between the walls of the grooves and thus suppresses the reflectance. A quarter-wavelength coating was also simulated for reference. The coating material has an ideal refractive index of $n_{ideal} = \sqrt{n_{si} \cdot n_{air}} = 1.85$, and the thickness was set at 20.3, 40.5, and $81.0 \mu\text{m}$ for an AR band with a center frequency of 2, 1, and 0.5 THz, respectively. Compared with the quarter-wavelength coatings, the moth-eye structures have broader AR bands. The power reflectance of the tapers with

different aspect ratios was also simulated, and the results for 0.72 THz are shown in Figure 2.3. From this result, we confirmed that the power reflectance can be reduced by employing a higher aspect ratio. When the aspect ratio exceeds 3, the power reflectance is reduced to almost 0 for these three tapered structures. These simulated results (Figures 2.1–2.3) suggest that the profile and aspect ratio have a strong influence on the AR characteristics of moth-eye structures.

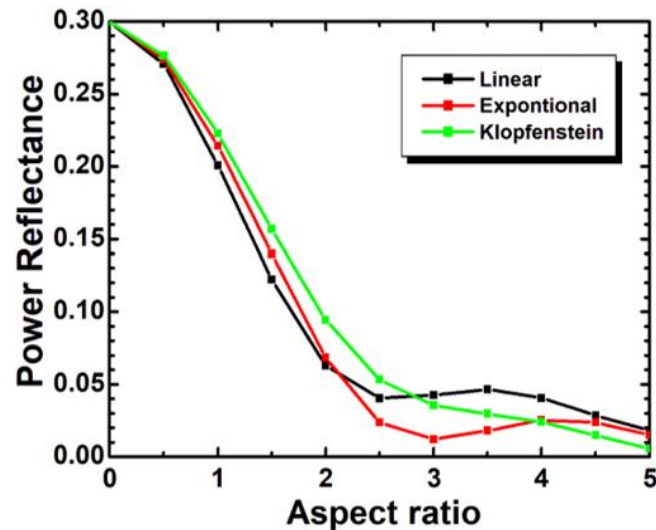


Figure 2.3. Relationship between power reflectance and aspect ratio of 1D tapered moth-eye structures at 0.72 THz. The power reflectance of moth-eye structures decreases as the aspect ratio increases.

2.2 Fabrication of moth-eye structures

To fabricate the moth-eye structures, we focused femtosecond laser pulses (D1000, IMRA America, Inc., center wavelength: 1045 nm; pulse width: 700 fs; repetition frequency: 100 kHz) onto the surface of a high-resistivity silicon substrate [plane 0.797 mm]. The target substrates were adhered to a two-axis orientation: (1 0 0); electrical resistivity: 1 k Ω ·cm; thickness: motorized stage. Two 1D tapered grating structures were fabricated by moving the stage at a constant speed of 5 mm/s, resulting in periodical parallel lines on the target surface. Figure 2.4 shows a schematic of the experiment setup, and the role of the galvanometer scanner will be discussed later. After laser ablation, the remaining components formed periodic tapered structures. Laser pulses (pulse energy= 8 μ J) were focused by a plano-convex lens with a focal length of 100 mm. The pitches were controlled by the movement setting of the stage, and the depths were adjusted by the number of scans. A square with a size of 10 mm \times 10 mm was fabricated within approximately 3 h for the 10-pass sample and within 4.5 h for the 20-pass sample. Figure 2.5 (a) shows a photograph of a Si substrate after femtosecond laser scanning and a 3D shape measurement obtained by laser scanning microscopy. Figure 2.5 (b) shows sectional scanning electron microscopy (SEM) images of these two samples. The 10-pass scanned sample has a depth of 20 μ m and a pitch of 25 μ m (i.e., aspect ratio = 0.9), and the 20-pass sample has a depth of 50 μ m and a pitch of 20 μ m (i.e., aspect ratio = 2).

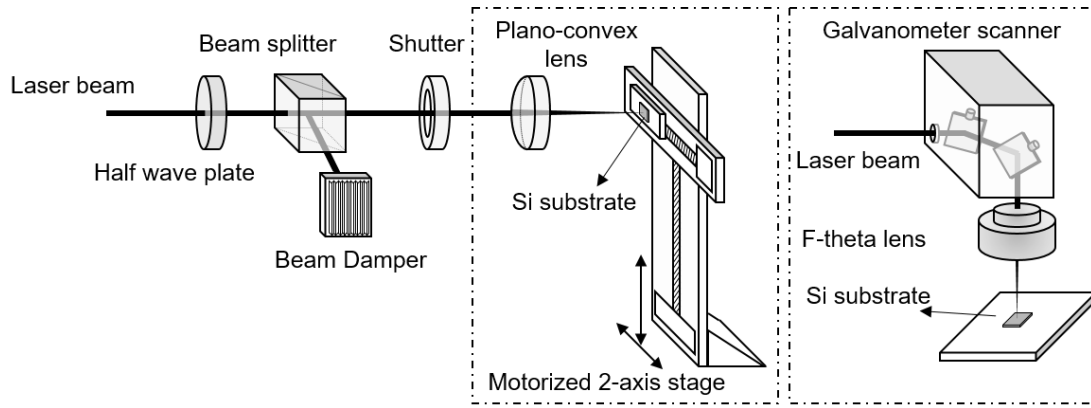


Figure 2.4. Schematic of the experiment setup. A plano-convex lens was assembled with a motorized stage, which could scan Si substrate at a relatively slow speed of 5 mm/s. By changing the settings of the plano-convex lens and motorized stage to a set of an F-theta lens and galvanometer scanner, the focused laser beam could be scanned at a high speed of 2825 mm/s.

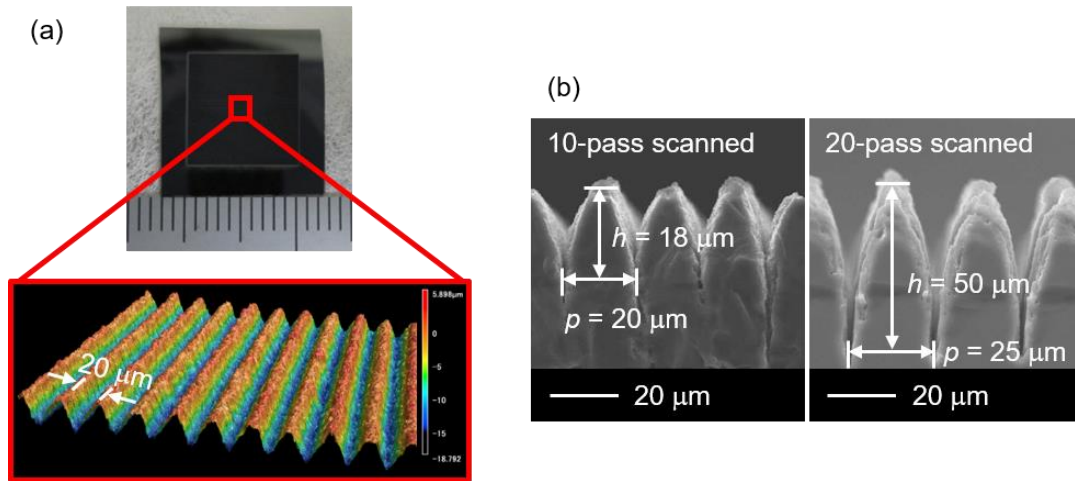


Figure 2.5. (a) Photograph of a Si substrate after 10-pass femtosecond laser scanning with a size of 10 mm \times 10 mm and a 3D shape measurement by laser scanning microscopy (Keyence, VK-X1050). (b) Sectional SEM images of fabricated periodic tapered structures.

However, as shown by the SEM image in Figure 2.5, we observed the deposition of molten Si and the reattachment of debris, which induced inhomogeneity in the tapered profile. These so-called thermal influences are assumed to be caused by excessive heating when samples are treated at a relatively low scanning speed. The continuous irradiation of unnecessary laser pulses at a constant point will induce excessive heat and pulse reabsorption by the plasma during laser ablation. To suppress thermal influences, we increased the scanning speed from the order of mm/s to m/s by replacing the two-axis motorized stage with a galvanometer scanner (Figure 2.4). An F-theta lens with a focal length of 100 mm was used to focus the laser pulses on the target surface. The two-axis motorized stage can move at a constant speed of 5mm/s, while the rotation of the galvanometer mirrors allows a rated scanning speed of 2825 mm/s on the substrate surface. By increasing the scanning speed, we obtained a smoother surface (Figure 2.6) and a higher aspect ratio of 2.25.

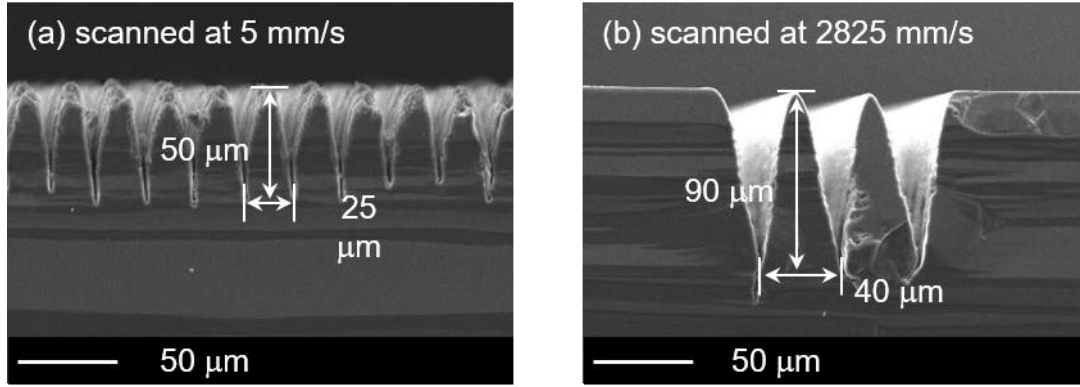


Figure 2.6. A sectional view of samples scanned at different speeds. At 2825 mm/s, a square with sides of 10 mm was fabricated within 1.5 hours, corresponding to a time reduction of one-third.

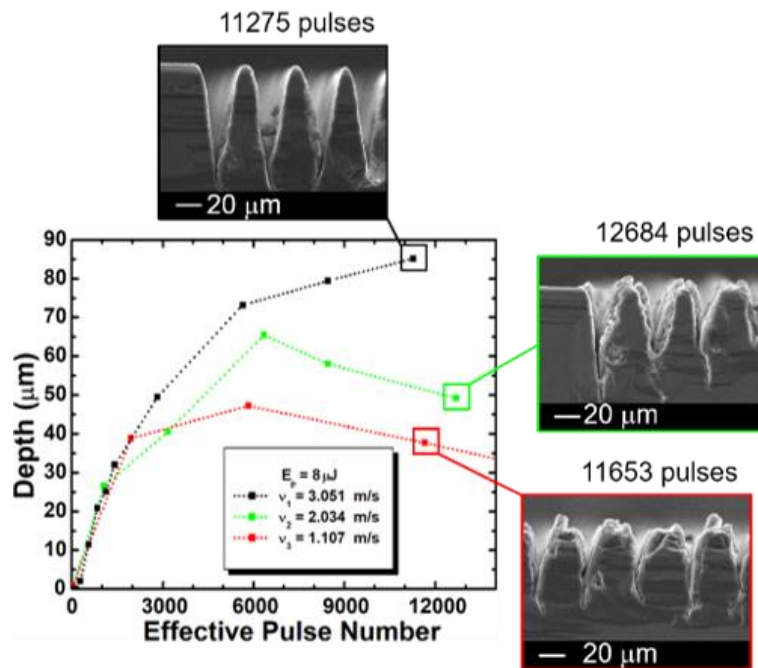


Figure 2.7. Relationship between depth and effective pulse number for tapers fabricated at different scanning speeds. Si substrates were irradiated by femtosecond laser pulses with a pulse energy of 8 μ J. As shown in the sectional SEM images, the internal surfaces of the grooves were smoother when higher scanning speeds were applied.

As shown in Figure 2.7, the taper was ablated deeper into the substrate when a higher scanning speed was applied. The effective pulse number (N_{eff}) can be defined as follows:

$$N_{eff} = \frac{d}{(v/f)} \times N_{pass} \quad (2-2)$$

where d is the diameter of the focused laser spot, v is the scanning speed, f is the repetition frequency of the laser, and N_{pass} is the pass number of each scanned line[68,69]. Increasing the scanning speed can reduce the number of laser pulses that are continuously irradiated at a given point over a short interval of time (1/100 kHz= 10 μ s); moreover, the reattachment of debris can be suppressed. A small proportion of the Si melted under higher scanning speeds. Figure 2.8 shows the relationship between depth and effective pulse number for tapers treated by different pulse energies (E_p).

Deeper grooves were obtained for higher pulse energy. Laser pulses with higher energy have larger fabrication voxels whose energy density exceeds the ablation threshold. The samples treated with 9133 pulses have a greater depth; furthermore, the groove depth decreased when excessive laser pulses were irradiated after their saturation. This phenomenon is considered to be caused by the molten material caused by excessive input energy. As the grooves are being cut, the internal surface increases while the average energy density decreases[70]. Once the average energy density is lower than the ablation threshold, the energy from these excessive laser pulses changes to heat, causing the material to melt and be deposited on the bottom surface or the internal walls of the grooves. Based on these experimental results, by scanning 8 μJ laser pulses at the standard speed of the galvanometer scanner (2825 mm/s), we fabricated 1D subwavelength tapered structures with pitches of 37, 42, and 51 μm and a uniform depth of 90 μm .

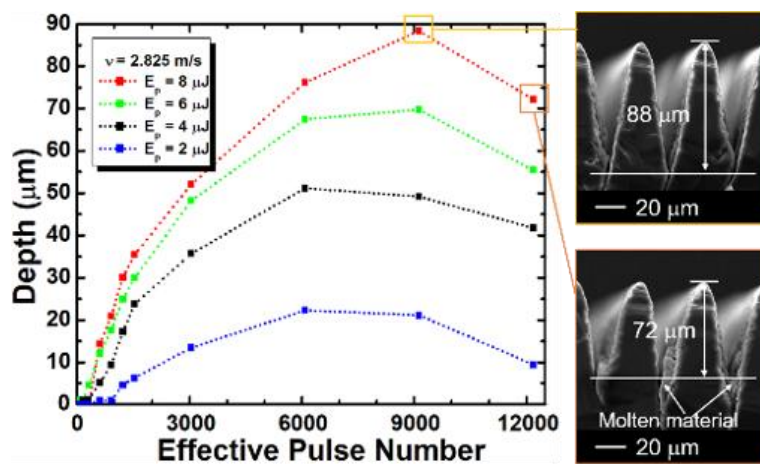


Figure 2.8. Relationship between depth and effective pulse number for tapers fabricated at different pulse energies. The scanning speed was set to 2825 mm/s. The depth plateaued after 9133 pulses due to molten material deposition caused by the average energy density attenuation.

2.3 AR characteristics based on the THz-TDS measurement

As showing in Figure 2.9, the AR characteristics of these tapered structures were measured by using a standard THz-TDS system, which has two photoconductive dipole antennas to generate and detect THz waves[71]. Based on sectional SEM images of these samples, HFSS models were used to obtain a simulated power reflectance for reference. The power reflectance of the fabricated gratings was obtained by comparing the measured transmittance of Si substrates with and without grating structures. Based on the thickness of the Si substrate (797 μm), reflection and transmission from both sides of the sample were considered in the calculations[49]. The Ti: sapphire femtosecond laser used in the THz-TDS system has a center wavelength of 812 nm, a pulse width of 60 fs, and a repetition frequency of 20 MHz. The laser beam was split into a pump beam for the generator and a probe beam for the detector. The THz transmission singles, A_{si} ($E_{\text{o,si}}/E_i$) and A_{ar} ($E_{\text{o,ar}}/E_i$), through the Si substrates with and without the grating structure, respectively, were measured and compared. Here, E_i is the incident signal, and $E_{\text{o,si}}$ and $E_{\text{o,ar}}$ are output signals transmitted by the Si substrate without and with ARS, respectively, as shown in Figure 2.10.

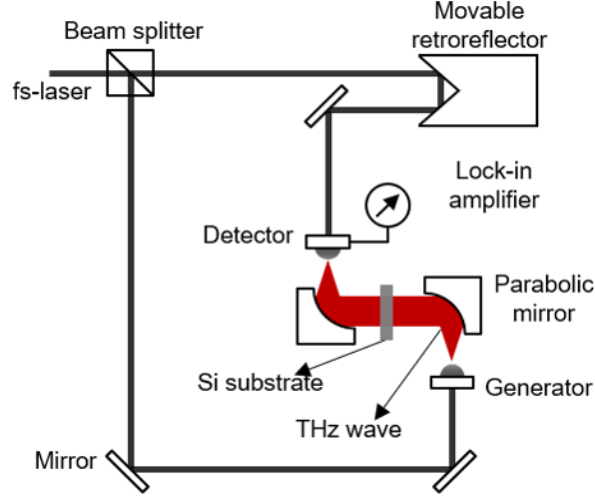


Figure 2.9. Transmitted singles were measured by using a standard THz- TDS system.

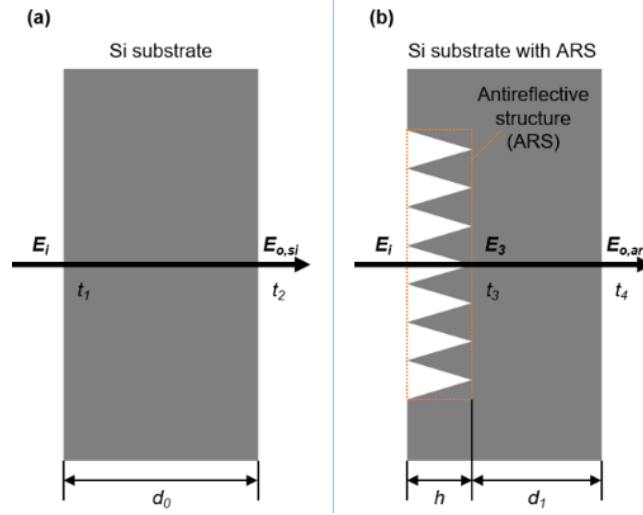


Figure 2.10. Images of THz waves transmit samples at normal incidence during THz-TDS measurement. (a) THz waves transmit the Si substrate. (b) THz waves transmit the Si substrate with ARS.

The complex refractive index n of Si was calculated from the measured results for $E_{o,si}/E_i$ as a function of frequency. From the evaluated results, n is $n_r - jn_i = 3.4 \pm 0.014 - j0.0012 \pm 0.0012$ in the frequency range of 0.2–2.5 THz. The real part, n_r , is much higher than the imaginary part n_i , such that $|n| \sim n_r$. All measurements were performed in TM (the electric field of the incident wave is perpendicular to the groove) and TE (the electric field of the incident wave is parallel to the groove) modes at normal incidence for frequencies ranging from 0.2 THz to 2.5 THz. Because the amplitudes of the incident waves remained nearly constant in the experiments,

$$\frac{A_{ar}(f)}{A_{si}(f)} = \frac{E_{o,ar}/E_i}{E_{o,si}/E_i} = \frac{E_{o,ar}}{E_{o,si}} \quad (2-3)$$

where f is the frequency of the THz signal. For Figure 2.10 (b), the following equation is given at the surface of the ARS,

$$R_{ar} = 1 - T_{ar} = 1 - \frac{P_{ar}}{P_i} \quad (2-4)$$

where R_{ar} is the power reflectance of the ARS, T_{ar} is the power transmittance of the ARS, P_i is the power of the incident signal, and P_{ar} is the power of the signal transmitted by the ARS. Because this signal propagates within the Si substrate, P_{ar} / P_i is calculated rather than measured, using the following equations. Based on the concept of the Poynting vector,

$$P_i = \frac{1}{2} \text{Re}(\mathbf{E}_i \times \mathbf{H}_i^*) = \frac{1}{2Z_0} |\mathbf{E}_i|^2 = \frac{1}{2Z_0} E_i^2 \quad (2-5)$$

$$P_{ar} = \frac{1}{2} \text{Re}(\mathbf{E}_3 \times \mathbf{H}_3^*) = \frac{|n|}{2Z_0} |\mathbf{E}_3|^2 = \frac{|n|}{2Z_0} E_3^2 \quad (2-6)$$

$$R_{ar} = 1 - |n| \left(\frac{E_3}{E_i} \right)^2 = 1 - |n| |t_3|^2 \quad (2-7)$$

where E_i and H_i are the electric and magnetic vectors of the incident wave. E_3 and H_3 are the electric and magnetic vectors of the wave transmitted by the ARS, and t_3 is the amplitude transmittance of the ARS. In the THz-TDS measurements, the output signals, $E_{o,si}$ and $E_{o,ar}$ can be expressed as follows,

$$\mathbf{E}_{o,si} = \mathbf{E}_i t_1 t_2 e^{-jnk_0 d_0} = \mathbf{E}_i t_1 t_2 e^{-n_i k_0 d_0} e^{-jn_r k_0 d_0} \quad (2-8)$$

where t_1 and t_2 are amplitude transmittance of the substrate surface and reverse, respectively. γ is the propagation constant for Si, and $\gamma = jnk_0$. k_0 is the wavenumber of the THz wave in the vacuum. $e^{-n_i k_0 d_0}$ gives the attenuation, and $e^{-jn_r k_0 d_0}$ gives the phase change. d_0 is the thickness of the Si substrate

$$\mathbf{E}_{o,ar} = \mathbf{E}_i t_1 t_2 e^{-jnk_0 d_0} = \mathbf{E}_i t_1 t_2 e^{-n_i k_0 d_0} e^{-jn_r k_0 d_0} \quad (2-9)$$

where t_4 is the amplitude transmittance of the substrate in reverse. t_1 , t_2 , and t_4 are given by $t_1 = \frac{2}{1+n}$, and $t_2 = t_4 = \frac{2n}{1+n}$. Therefore, the ratio of two output signals is

$$\frac{E_{o,ar}}{E_{o,si}} = \frac{|t_3| |1+n|}{2} e^{-n_i k_0 (d_1 - d_0)} e^{-jn_r k_0 (d_1 - d_0)}. \quad (2-10)$$

The amplitude transmittance of the ARS, t_3 , can be determined by using Equation (2-9), and derived from the absolute values,

$$\left| \frac{E_{o,ar}}{E_{o,si}} \right| = \left| \frac{A_{ar}(f)}{A_{si}(f)} \right| = \frac{|t_3| |1+n|}{2} e^{-n_i k_0 (d_1 - d_0)} \quad (2-11)$$

$$|t_3|^2 = \frac{4}{|1+n|^2} \left(\frac{A_{ar}(f)}{A_{si}(f)} \right)^2 e^{2\text{Im}(n)k_0 h} \quad (2-12)$$

where $d_0 - d_1 = -h$, and $\text{Im}(n) = -n_i$. By substituting Equation (2-12) into Equation (2-4), we can obtain the power reflectance of the ARS.

$$R_{ar}(f) = 1 - \frac{4|n|}{|1+n|^2} \left(\frac{A_{ar}(f)}{A_{si}(f)} \right)^2 e^{2\text{Im}(n)k_0 h} \quad (2-13)$$

where h is the effective height of the ARS, determined by the difference between the measured phases of $A_{ar}(f)$ and $A_{si}(f)$ from Equation (10):

$$\Delta\phi = -n_r k_o (d_1 - d_0) = n_r k_o h \quad (2-14)$$

where $\Delta\phi$ is the measured phase difference. In the measurements, the estimated values of h were relatively small, typically less than 30 μm ; thus, $e^{2\text{Im}(n)k_o h} \sim 1$. For reference, the HFSS models were based on the coordinates of the points in the sectional SEM images and were simulated to estimate the power reflectance.

Figure 2.11 (a) shows the results for the 10-pass sample. The reflectance decreased to almost zero in the TM mode, which is better than the approximately 50% decrease observed in the TE model. This difference can be explained by the circuit model reported by Kadlec[72], in which the periodic grooves are considered as a series circuit in the TM mode and a parallel circuit in the TE mode. This difference between the TM and TE modes suggests that this one-dimensional tapered structure is very effective to reduce the undesired reflection loss for TM-polarized THz waves[45]. A similar two-dimensional tapered structure can be considered as a resolution for unpolarized THz waves. Figure 2.11 (b) shows the measured and simulated reflectance for the TM mode. The relative power reflectance is reduced to almost 0 at 1.9 THz and 1.6 THz according to the 10-pass and 20-pass treated samples, respectively. This result suggests that the 20-pass sample has a broader AR band, which may be caused by the increased pitch and aspect ratio. The simulated results obtained by HFSS show good agreement with the experimental results and confirm the accuracy of these results.

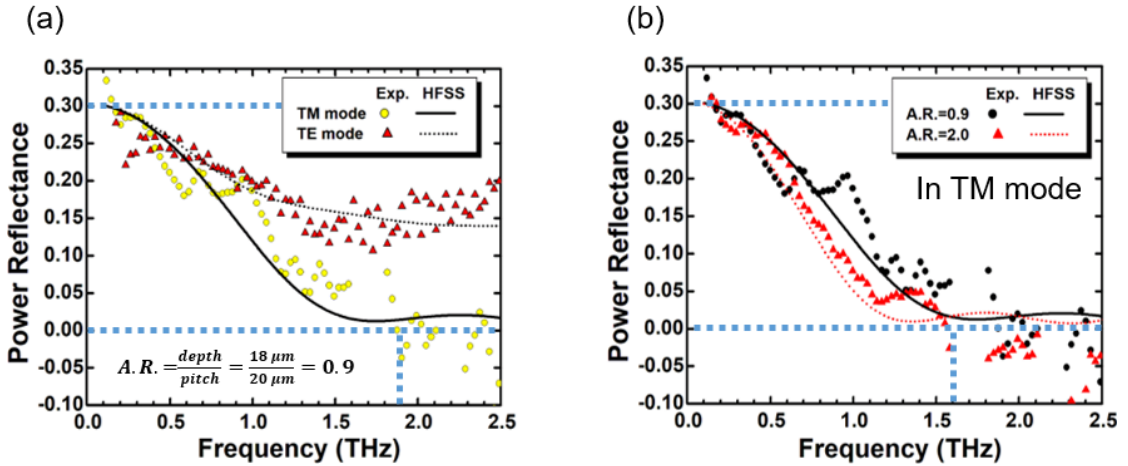


Figure 2.11. AR characteristics of samples scanned at 5 mm/s. The dots show experimental data obtained by THz-TDS, and the lines show simulated results obtained by HFSS. (a) Results for a sample with an aspect ratio (AR) of 0.9 in the TE and TM modes. (b) Comparison of the AR regions of two samples with different aspect ratios in the TM mode.

Figure 2.12 shows sectional SEM images, and the power reflectance calculated from the measured data obtained by THz-TDS (dots) and simulated by HFSS (lines). For the tapered structures with pitches of 42 μm and 51 μm , the measured variations in reflectance are in good agreement with the theoretical predictions for frequencies lower than 1 THz. The measured and simulated results do not match as well for the 37- μm -pitch grating. This mismatch is considered result from the difference in aspect ratios for the HFSS model ($90 \mu\text{m}/37 \mu\text{m} = 2.43$) and the actual sample [$(90 \mu\text{m} - 7.3 \mu\text{m})/37 \mu\text{m} = 2.24$]. A higher aspect ratio can improve the performance of AR characteristics over the entire AR band[73]. During laser processing, the laser spot was focused to a diameter of 41 μm , and the scanning was overlapped to obtain a pattern with a 37- μm

interval between each groove. Because of the scanning overlap, the top of the taper is $7.3\ \mu\text{m}$ below the surface of the Si substrate. For both the HFSS and measured results, ripples can be observed at frequencies beyond the first minimum power reflectance. The first minimum point shifts to lower frequencies as the pitch increases. According to Equation (2-1), tapers with a larger pitch correspond to an AR band with longer wavelengths in the lower frequency region.

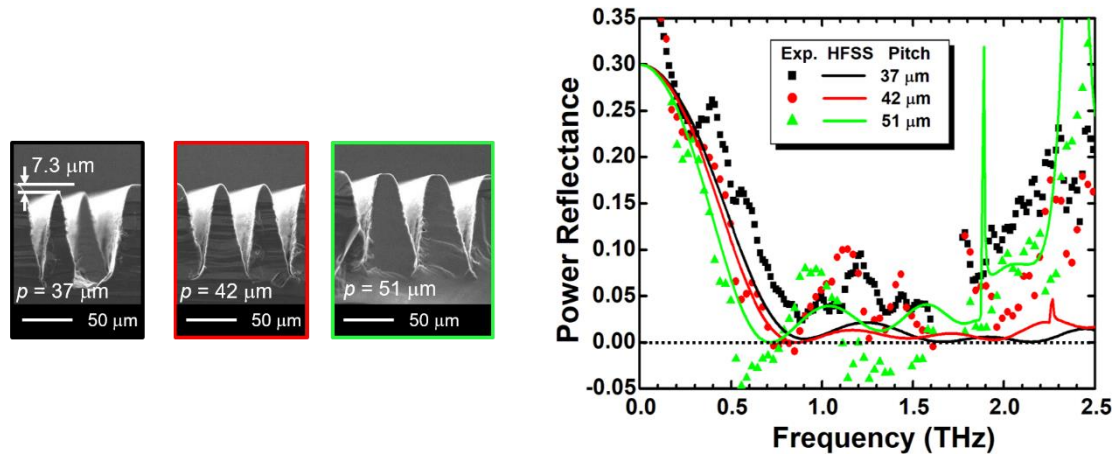


Figure 2.12 AR characteristics of the tapered grating structures.

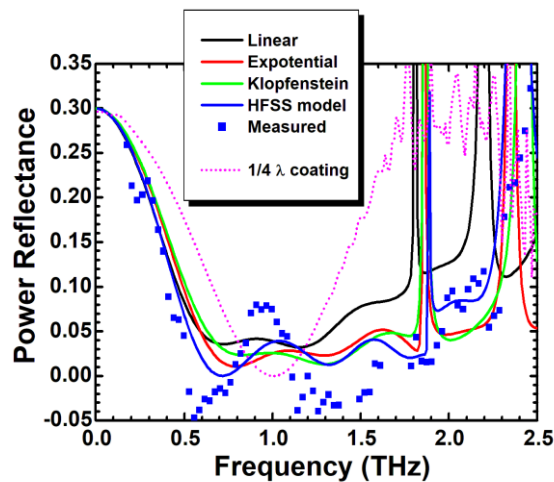


Figure 2.13. Comparison of the power reflectance for a 51- μm taper ($h/p = 90\ \mu\text{m}/51\ \mu\text{m}$) and a quarter-wavelength coating. The lines show simulated results obtained by HFSS, and the dots present calculated results based on measured data for the 51- μm taper.

Similar to the Klopfenstein taper shown in the sectional view, the 51- μm -pitch sample also has a flat top, but the measured reflectance is not as stable as the simulated results for the Klopfenstein taper. This result may be caused by a change in the shape from the top to the waist of the taper; this shape is convex in the laser-ablated sample, but concave in the Klopfenstein taper. To confirm the type of tapers that were fabricated, linear, exponential, and Klopfenstein tapers with the same size as 51- μm taper were modeled for simulations. The results are summarized in Figure 2.13. For the measured and HFSS simulated results (blue line and dots), the trends of the curve are similar to the result for the exponential taper (red line). By comparing the simulated results for the linear, exponential, and Klopfenstein tapers, we found that the exponential taper shows a lower power reflectance in the range from approximately 0.6 to 1 THz, but the

Klopfenstein taper has lower power reflectance ranging from approximately 1 to 1.7 THz. Compared with the quarter-wavelength coating designed for 1 THz, the laser-ablated structures have much broader AR bands.

2.4 Conclusions

One-dimensional periodic tapered structures for achieving antireflection of THz waves were theoretically modeled by HFSS and experimentally fabricated using a femtosecond laser. The AR characteristics were evaluated by a THz-TDS system at 0.2–2.5 THz. The theoretical simulations predicted that the taper profile has a strong influence on the performance of a moth-eye structure. The Klopfenstein taper offers the lowest and most stable AR characteristics with the weakest ripples after the first minimum value, but the exponential taper has a lower power reflectance over a small region after the first minimum value. A femtosecond laser was employed to fabricate periodic tapered structures with different aspect ratios and pitches. The production of molten silicon was suppressed by increasing the scanning speed, resulting in a higher aspect ratio of 2.25 and a smoother internal surface for the ablated grooves. Increasing the scanning speed is an efficient way to improve the quality of a laser-ablated surface. The THz-TDS measurements and HFSS simulation results matched well, especially for the 51- μm -pitch grating. For all of the fabricated samples, the power reflectance of the AR surface is reduced to almost zero over a band wider than 1 THz (0.7–1.9 THz), which is much broader than that for a quarter-wavelength coating. Ripples in the power reflectance were observed for both samples. Tapers with optimized profiles can be applied to suppress this variation; such taper profiles can be modified by adjusting the fabrication conditions during laser processing, such as the focus position, laser polarization, and scanning pattern. As a typical material for components in the THz range, high-resistivity silicon can be used for lenses and splitters, particularly for the lenses in photoconductive antennas. This type of moth-eye structure can be used to improve the performance of these components. In addition to high-resistivity silicon, other materials suitable for the THz range, such as GaAs, LiNbO₃, quartz, can also be applied with a moth-eye structure to improve the performance of related THz components. As an advanced microfabrication method, femtosecond laser processing is suitable for realizing an optimal profile for tapered AR structures on these materials. Femtosecond-laser-fabricated periodic tapered structures thus have great potential for improving the performance of components in the THz range.

Chapter 3

Applications of moth-eye structures to THz generators

3.1 Introduction

The actual applications of THz waves are limited by the lack of portable high output THz sources. Developing such THz wave sources is an important task for promoting the applications of THz waves. Alternatively, increasing the extraction efficiency of existed THz sources which are suffering the high reflection loss is an achievable way to obtain a higher output intensity, such as a THz photo conductive (PC) antenna fabricated on Gallium arsenide (GaAs) or Zinc oxide (ZnO). In this chapter, a GaAs-based terahertz (THz) signal combiner was proposed and fabricated with moth-eye structures to further improve its output intensity. Moth-eye structures are also fabricated on the ZnO surface, but the measured transmittance of the ZnO moth-eye structure (without any post-processing) was not as good as that of GaAs. The undesired results are possibly induced by the absorption of defects in laser-ablated ZnO surface, and the post-processing of annealing was demonstrated for improving the transmittance of laser fabricated moth-eye structure on ZnO substrate.

3.2 Periodic terahertz-wave generator on LT-GaAs substrate

3.2.1 Introduction

To meet the needs of developing a compact and high-power coherent terahertz (THz) wave source, a terahertz (THz) signal combiner was designed and fabricated with one dimensional photoconductive (PC) antenna array using a metal waveguide[74,75]. Moreover, the laser-ablated moth-eye structure is an effective method to reduce the reflection loss for THz components[51,76,77]. For improving the output efficiency, we have applied the moth-eye structures to the photoconductive antenna array to improve the output of the periodic terahertz-wave generator. To improve the generation efficiency of THz waves from the periodic terahertz-wave generator, a femtosecond laser was employed to fabricated a moth-eye structure on the reverse of the antenna substrate, a low-temperature-grown GaAs (LT-GaAs) substrate.

3.2.2 Experiment and results

Figure 3.2.1 is a schematic drawing of the periodic THz-wave generator. It consists of a one-dimensional array of photoconductive (PC) antennas on a LT-GaAs substrate. When irradiating with a tilted front laser beam, THz waves will be generated and incident radially from PC antennas to the inside of the waveguide, and only the THz waves with the same propagation direction of the laser beam will in force due to the interference regardless of frequency. To improve the transmission efficiency of the THz wave from the LT-GaAs substrate to the inside of the metal waveguide, we fabricated moth-eye structures on the reverse of the LT- GaAs substrate. Figure 3.2.2 shows the details of both sides of the PC antenna. Optical microscope image of the PC antenna

array, THz-wave generator image, and SEM image of moth-eye structure on the reverse of LT-GaAs substrate (size: 0.7 mm × 6 mm, thickness: 0.15 mm) are shown from top to bottom, respectively. The PC antennas have a length of 253.8 μm, a line width of 26.5 μm, a gap of 13.8 μm. The moth-eye structure consists of 2-dimensional tapers with an aspect ratio of about 2.16 (depth/width = 80 μm / 37 μm = 2.16), which was fabricated by scanning focused femtosecond laser pulses (wavelength: 1045nm, pulse width: 700 fs, pulse energy: 6 μJ; F-theta lens: 100 mm) on the reverse of the LT-GaAs substrate. The fabricated area is 0.5 mm × 4 mm on the center of the LT-GaAs substrate surface. The effective pulse number for each point is 990 in the calculation.

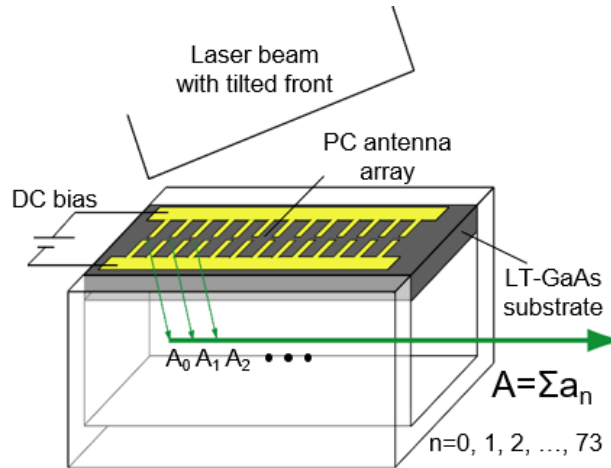


Figure 3.2.1. Schematic drawing of the periodic THz-wave generator with a photoconductive (PC) antenna array in a rectangular metal waveguide. A_n ($n = 0, 1, \dots, 74$) and A are THz signals from a signal PC antenna and the combined one, respectively.

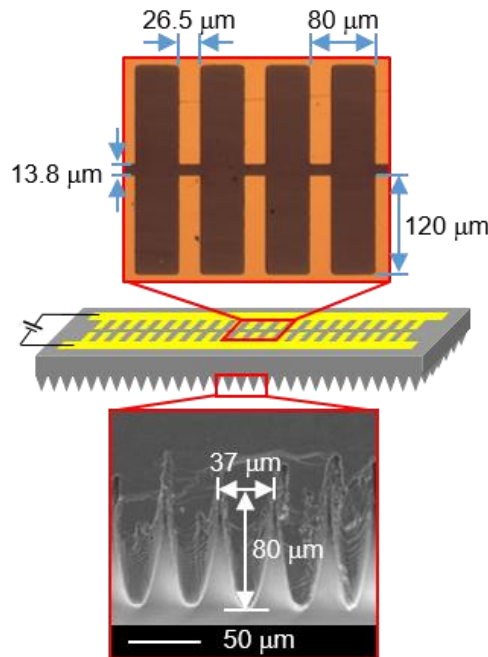


Figure 3.2.2. Details of both sides of the PC antenna array.

Firstly, PC antennas were singly measured for the basic characteristics by a THz-TDS system, where the incident laser beam was focused on a single dipole antenna by

an achromatic lens at a normal incident. Then, the THz-wave combiner was measured by the system showing in Figure 3.2.3, where the achromatic lens was changed by a cylindrical lens, and the incident beam has an incident angle of 54.5° . Figure 3.2.4 shows the output signals when only the 10th, 30th, 50th (E10, E30, E50) antenna was irradiated, respectively. The antenna number is added from the output side. E50 is the farthest one from the output window among these 3 antennas.

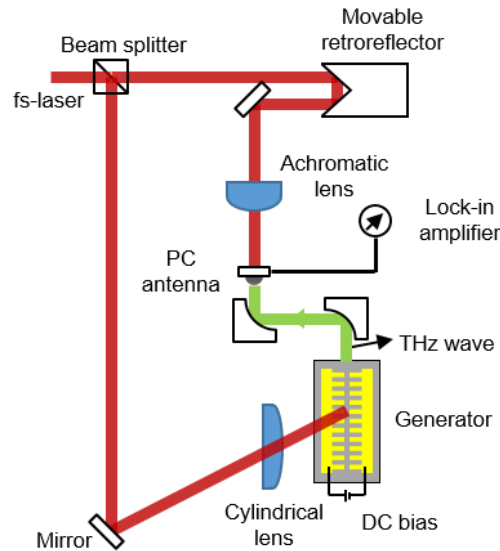


Figure 3.2.3. THz-TDS system was used for evaluating the characteristics of periodically arranged PC antennas.

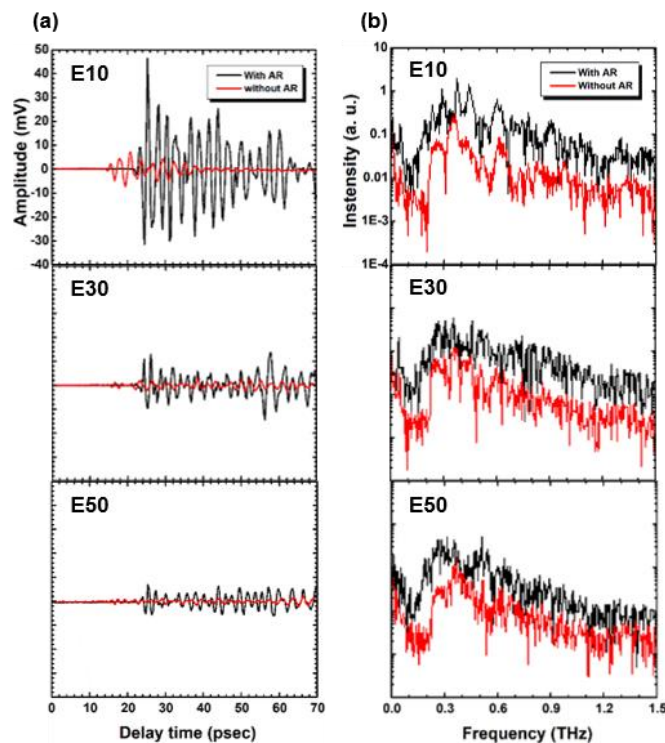


Figure 3.2.4. Time waveforms and spectrum intensity were measured by the THz-TDS system, when only the antenna E10, E30, E50 were irradiated, respectively.

Figure 3.2.4 (a) is the time waveform of the single from antennas with and without moth-eye structures. Figure 3.2.4 (b) shows their intensity of the spectrum of the singles

after the Fourier transformation. Multi-pulse was observed in time waveforms because of the dispersion characteristics of waveguides. The amplitude is observed reducing accompanying the distance from the output window. The signal from the moth-eye structured antennas has a much bigger maximum peak than the unstructured ones. According to the spectrum intensity, periodic THz-wave generator fabricated with moth-eye structure has an overall improvement of intensity at the region of 0.1-1.5 THz. Figure 3.2.5 shows the output signals when the antennas E1~E35 were irradiated by a tilted beam front with θ of 54.5° . At the frequency of 0.342 THz (calculated f_{out}), 0.283 THz, 0.226 THz (experimental f_{out} of the generator without and with moth-eye structure). The improvements are 3, 2.5, and 4.4 times, respectively.

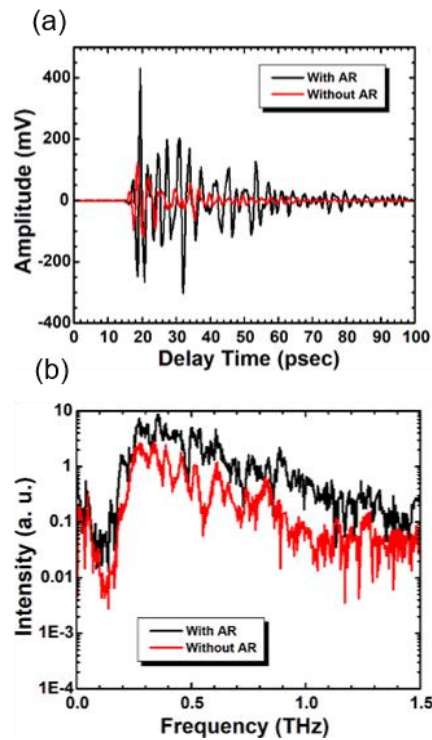


Figure 3.2.5. Measured results by the THz-TDS system, when the antenna E1~E35 were irradiated by a tilted beam front θ of 54.5° .

3.2.3 Conclusion (GaAs-based moth-eye structure)

Femtosecond laser-ablated moth-eye structure was fabricated on the reverse of a periodic terahertz-wave generator. The THz-TDS system measured results show a very good improvement of the output signal. The laser-ablated moth-eye structure should be an efficient method to improve the output of a PC antenna-based terahertz signal generator.

3.3 Femtosecond-laser-induced cleavage on a zinc oxide substrate

3.3.1 Introduction

Zinc oxide (ZnO) has been actively researched for a broad range of applications in ultraviolet (UV) and visible optical regions [78,79]. Benefiting from a wide bandgap (~3.3 eV) and various defect levels, it has been studied for more than two decades and has applications both scientific (e.g., UV–visible emitters and detectors [80,81]) and daily life (e.g., sunscreen and display[82–84]). Beyond the UV–visible region, ZnO is reported to have high transmittance and high refractive index in the terahertz (10^{11} – 10^{13} Hz) region [85,86]. The emission of terahertz waves from ZnO-based devices is very strong evidence that ZnO also has potential uses for terahertz components[85,87–89]. Developing the ZnO-based THz emitters is important for the diversification of THz light sources, which can promote the applications of THz waves in daily life. Due to the high refractive index of 2.8 in the THz region, a power reflectance of more than 22% will be induced when THz waves were propagating into the ZnO surface in a normal incidence. This high reflection loss is a disadvantage hindering the development of ZnO-based components for THz waves. Hence, antireflection strategies also need to be proposed for ZnO-based THz components due to this non-neglectable reflection loss.

Table 3.3.1 Laser processing conditions of ZnO-based moth-eye structures.

Number	1	2	3	4
E_{pulse} (μJ)	8	8	8	30
Repe. rate (kHz)	100	100	100	100
Scan speed (m/s)	3	3	3	5
N_{pass}	800	2000	8000	10000

In both the UV–visible and terahertz regions, laser processing is an efficient method for realizing thin-film-based devices or nano/microstructure-based functional surfaces [54,57,59,90,91]. For promoting the applications of THz waves in daily life, we tried fabricating moth-eye structures on ZnO substrate. Three 2D (cross scanning pattern) and a 1D (line scanning pattern) moth-eye structures were fabricated by using femtosecond laser processing. Samples 1-3 were fabricated by using the laser mentioned in chapter 2, and sample 4 was fabricated by a Yb: KGW laser with higher output power (central wavelength: 1030 nm; pulse duration: 700 fs, PHAROS PH1-10, Light Conversion, Lithuania). Table 3.3.1. shows the processing conditions of the four ZnO moth-eye structures. Figure 3.3.1 shows images of laser fabricated moth-eye structure on ZnO substrate (a), its 3D measurement by CLSM (b), and a section view of a sample with higher aspect ratio (c). Figure 3.3.2 shows the THz-TDS measured spectrum intensity for these four moth-eye structures. The THz-TDS measured results of ZnO-based moth-eye structures are not as good as those of Si and GaAs. Antireflective properties were not observed for these four samples. The intensity of transmitted THz waves even lower than the unprocessed ZnO surface. According to Figure 3.3.1 (a), the laser-irradiated area is dark brown, while the unprocessed surface is almost transparent in the visible region. This discoloration suggested that the ZnO surface may be modified by laser ablation, and the laser-irradiated area may have higher absorption than that of a bare surface in the visible region. Due to the special band structure of ZnO with various defect levels, defects could be easily induced by the

extreme conditions of high temperature and pressure in the laser ablation center. This modification on defect may also affect the absorption of THz waves. Consequently, the modification on defect induced by laser irradiation needs to be studied, and the suppression of AR properties due to the increased absorption demands a solution.

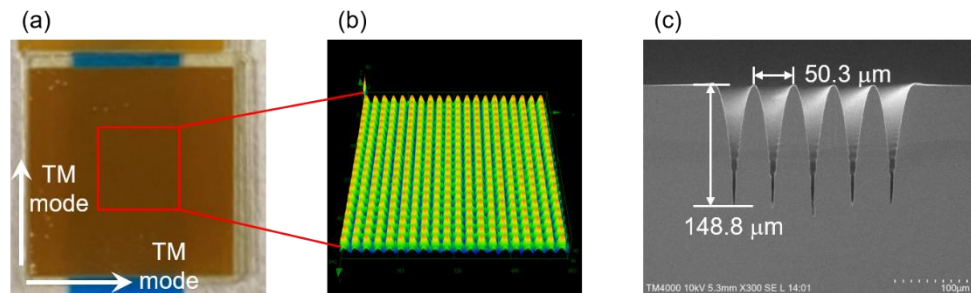


Figure 3.3.1. (a) an image of a 2D structure, (b) the CLSM measurements, and (c) a sectional view of the 1D moth-eye structure.

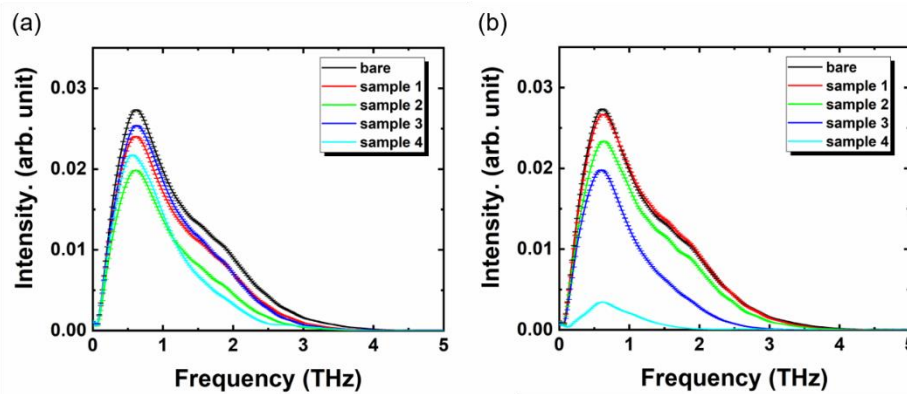


Figure 3.3.2. The THz-TDS measured spectrum intensity for these four moth-eye structures under (a) TM and (b) TE mode. For the 2D structures, the direction of the electric field during the THz-TDS measurements is shown in Figure 3.3.1 (a). For the 1D structure, the direction of the electric field during the THz-TDS measurements is perpendicular to the groove in TM mode and parallel to the groove in TE mode.

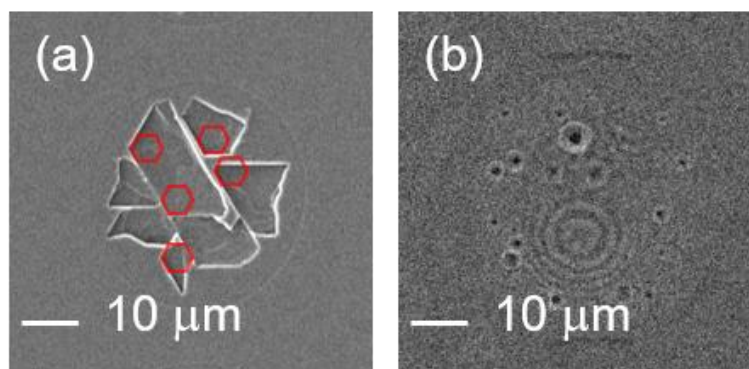


Figure 3.3.3. The one-pulse irradiated surface of ZnO (a) and Si (b) by a femtosecond laser with a wavelength of 1,030 nm and pulse energy of 30 μJ . Corners with 120° angle randomly distributed in the one-pulse irradiated area are observed, which may be pieces from broken hexagon patterns.

Although ZnO-based thin films fabricated by pulsed-laser deposition have been widely reported by a vast number of researchers [79], functional surface structures fabricated by direct laser irradiation upon a ZnO substrate occur seldom, despite the

appearance of cheaper lasers with extremely high output [92,93]. Recently, femtosecond laser-induced nano-ripples on ZnO surfaces have been separately reported by Hang et al. [94] and Liu et al. [95]. Multiple laser pulses are irradiated upon the ZnO substrate surface to fabricate structures with a size less than the wavelength of the incident laser pulse. Meanwhile, single-pulse irradiation physics is not mentioned in such literature. Figure 3.3.3 (a) shows the one-pulse irradiated ZnO substrate surface of our work; this is a very interesting morphology that differs from the laser-irradiated surface of the silicon (Si) substrate or some other metal materials [96–98]. As shown in Figure 3.3.3 (b), in general, these one-pulse irradiated marks on Si or other metal surfaces are considered to be caused by melting with heat. On the contrary, no melting was observed from the one-pulse irradiated spot of the ZnO substrate; instead, corners with 120° angle (pieces from broken hexagon patterns) are observed.

To find out a solution to improve the AR performance of ZnO moth-eye structures, as well as the formation mechanism of such marvelous cleavage phenomena in detail, we studied the formation and changing of defects on the surface of ZnO substrate irradiated by laser pulses. we performed one-pulse irradiation (pulse energy: 6–60 μJ) on the surface of the ZnO substrate, as well as multi-pulse (1–11 pulses) irradiation with the same pulse energy of 30 μJ . The dependence of pulse energy upon cleavage depth was discussed and quantitatively analyzed with a three-photon absorption model; a cleavage-melt shift was also observed after 4 laser pulses. This shift is attributed to the enhancement of absorption due to the initial pulses, and the mechanism is supported by our measurement of cathodoluminescence. Moreover, by annealing at 300–500 $^\circ\text{C}$, the transmittance of laser fabricated ZnO moth-eye structure was developed, and these annealed ZnO moth-eye structures showed broadband AR features.

3.3.2 Experimental details

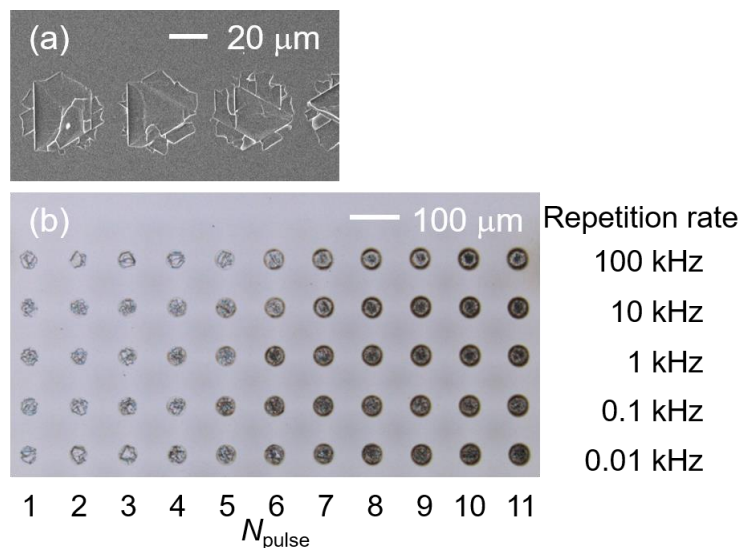


Figure 3.3.4. (a) SEM image of the one-pulse irradiated ZnO substrate surface under pulse energy of 60 μJ by scanning a laser beam in a line. (b) CLSM images of spots irradiated by laser pulses with different pulse numbers (N_{pulse}) and repetition rates.

Femtosecond-laser pulses from a Yb: KGW laser (central wavelength: 1,030 nm; pulse duration: 700 fs, PHAROS PH1-10, Light Conversion, Lithuania) were irradiated and focused upon the surface of a ZnO substrate (orientation: (0001); hexagonal

structure; purchased from CrysTec GmbH, Germany) by an F-Theta lens (focus length: 200 mm, SILL 297358, Sill Optics GmbH, Germany) at normal incidence. A laser beam operating at a repetition frequency of 100 kHz was guided by a galvanometer scanner head (SUPERSCAN IV-30, Raylase GmbH) to directly write lines on the surface of a ZnO substrate at a constant speed of 5,000 mm/s. Thus, one-pulse irradiated spots arranged in a line with a spacing of 50 μm can be easily obtained by a single scan (Figure 3.3.4 (a)). Pulses with energies ranging from 6 μJ to 60 μJ were used to obtain the one-pulse irradiated spots; as shown in Figure 3.3.4 (b), multi-pulse irradiated samples were obtained by irradiating the laser pulses (pulse energy: 30 μJ) upon the same spot, and the pulse numbers (N_{pulse} : 1–11) were controlled by adjusting the irradiating time and repetition rate (0.01–100 kHz). After laser irradiation, the samples were separately immersed in acetone and purified water for three minutes of ultrasonic cleaning. The irradiated areas were observed by a scanning electron microscope (SEM, TM4000pulseI, Hitachi, Japan, at 5 kV) and a confocal laser scanning microscope (CLSM, LEXT ILS4100, Olympus, Japan) to attain the morphological details (radius, cleavage depth). The cathodoluminescence (CL, MonoCL4, Gatan Inc., USA with JSM-7800F, JEOL, Japan) of the laser-irradiated spots (repetition rate, 10 Hz) was also measured to analyze their luminescence properties and get their surface defect information.

ZnO moth-eye structures are annealed on a hotplate in the air. Samples 1–3 were annealed for 30 minutes at 300, 400, 500 $^{\circ}\text{C}$, and sample 4 was annealed for 15 minutes at 500 $^{\circ}\text{C}$. The spectrum intensities of these samples were obtained by taking the Fourier Transform of the THz-TDS waveform. A time window of 6.66 ps (2.22 ps before and 4.44 ps after the first dip) was selected for removing the Fabry-Perot fringes causing by the multi-reflected signal[53]. The measured spectrum intensities (average of 100 measurements) of the ZnO substrates with and without tapered structures were compared to obtain the power reflectance of the fabricated AR structures. Based on the thickness of the ZnO substrate, the reflection and transmission from both sides of the sample were considered in the calculations[49,54].

3.3.3 Results and discussion

Figure 3.3.5 (a) shows SEM images of the one-pulse irradiated spots on the ZnO substrate surface. Broken hexagonal cleavages are observed when $E_p > 10 \mu\text{J}$. The laser-induced cleavages are centered at the irradiated spot and surrounded by a no-cleavage zone. This central location of cleavage is thought to be caused by the Gaussian energy distribution of the laser beam, whose center has the highest intensity. The Gaussian laser beam propagation in the z-direction can be given by

$$F(x, y) = F_0 e^{-\left(\frac{1}{w_0}\right)^2 [(x-x_0)^2 + (y-y_0)^2]}, \quad (3-1)$$

where F is the laser fluence (energy per unit area) and F_0 is its max value, w_0 is the radius at which the fluence falls to F_0/e^2 , and (x_0, y_0) is the beam center of the profile[99–102]. The index $(x-x_0)^2 + (y-y_0)^2$ denotes the square of the distance to the center, i.e., the square of the radius (r) from the aerial view. Substituting $r^2 = (x-x_0)^2 + (y-y_0)^2$ into Equation (3-1) and replacing I_0 with $2E_p/(\pi w_0^2)$, we obtain

$$r^2 = \frac{1}{2} w_0^2 \ln \frac{E_p}{E_{th}}, \quad (3-2)$$

where τ is the laser-pulse duration (700 fs), E_p is its pulse energy, and E_{th} is the ablation threshold energy for our processing system. Based on our SEM images, we measured the ablation areas of the one-pulse irradiated spots (shown by black squares in Figure 3.3.5 (b)) and obtained the r^2 value. The red broken line in Figure 3.3.5 (b) shows the fitting curve described by Equation (3-2); according to the simulated values of E_{th} (5.11 μJ) and w_0 (21.5 μm), we can obtain the ablation threshold, $F_{th} = 0.35 \text{ J/cm}^2$.

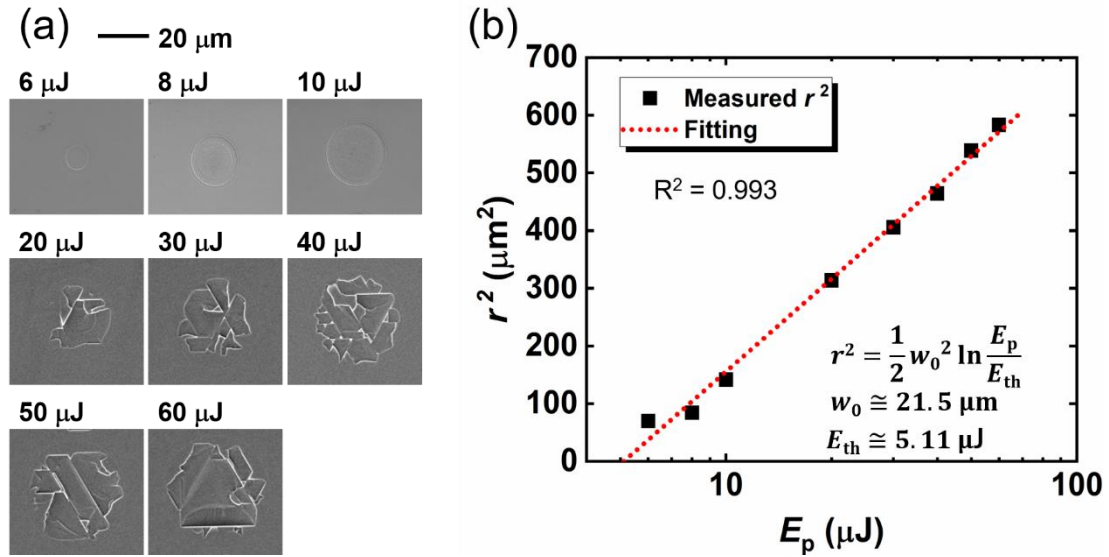


Figure 3.3.5. (a) SEM image of one-pulse irradiated spots. (b) The square of the spot radius (black squares) is plotted as a function of the pulse energy. The slope of the linear fitting yields the beam radius at the surface (w_0). The extrapolation to zero shows the ablation threshold in the energy (E_{th}) of one-pulse irradiation.

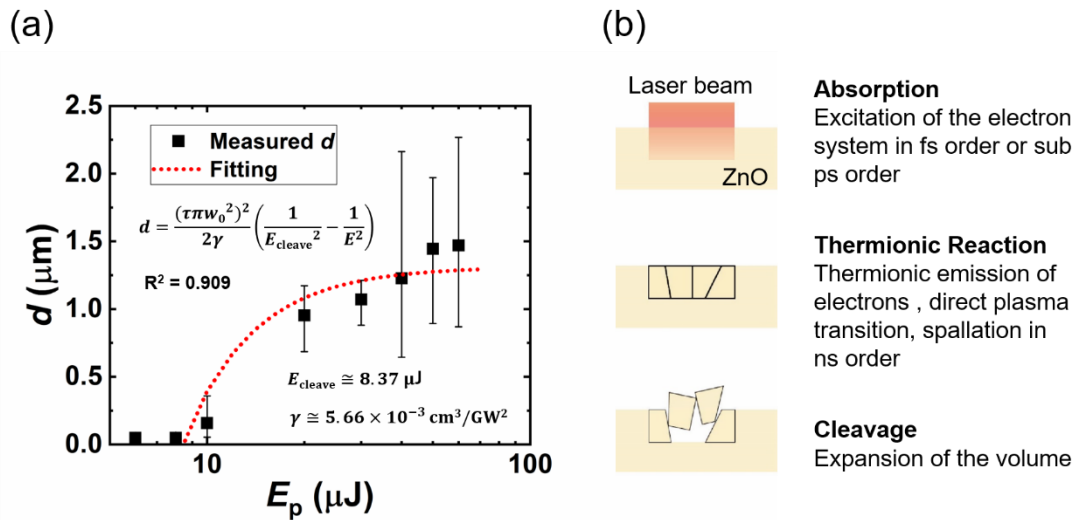


Figure 3.3.6. (a) The cleavage depth (d) (black squares) is plotted as a function of the pulse energy. The red broken line shows a fitting result based on a three-photon absorption model. The extrapolation to zero shows the laser-induced cleavage threshold energy (E_{cleave}). (b) Image of the laser-induced surface-cleavage model.

The bandgap of ZnO (3.3 eV) is as wide as 3 times that of Si (1.1 eV); when a laser pulse with a wavelength of 1,030 nm ($E_{photon} = 1.2 \text{ eV}$) is irradiated to the Si substrate, most energy will be absorbed by the surface. On the contrary, in the case of ZnO, multi-photon absorption will predominate, and some of the energy will propagate into the

ZnO substrate. The cleavage depths (d) of the one-pulse irradiated spots are plotted as a function of the pulse energy, as shown in Figure 3.3.6 (a). For the one-pulse irradiated samples in our work, the pulse energy irradiated to the ZnO substrate is below 60 μJ , and the laser-induced cleavage depth is less than 3 μm according to CLSM measurement; this suggests that the propagation time from the surface to the cleaved valley of the laser pulse is shorter than 20 fs ($t = nd/c$, where t is the propagation time, n is the refractive index of ZnO, and c is the speed of light). Hence, multi-photon absorption (femtosecond or sub-picosecond order from the laser-matter interaction) will be finished before the thermionic reaction (nanosecond order from the laser-matter interaction); the expansion caused by the thermionic reaction then leads to cleavage [103,104]. Figure 3.3.6 (b) presents an image of the laser-induced surface cleavage. The coefficients of two-photon absorption (2PA) and three-photon absorption (3PA) of bulk ZnO were measured by Vivas et al. [105] and He et al. [106], respectively. Vivas reported that a saturable one-photon absorption (1PA) was observed due to the deep levels; a mixture of 1PA, 2PA, and 3PA was observed for the excitation from 530 nm to 800 nm and, when the ZnO was excited by light with a wavelength from 820 nm to 980 nm, 3PA predominated. Because the 1,030-nm wavelength is close to the 3PA-predominant region in the result given by ViVas, we propose a 3PA-based laser-induced cleavage model.

When a laser beam with an average intensity of I propagates through the sample along the z -direction, the 3PA result can be written as

$$\frac{dI}{dz} = -\gamma I^3; \quad (3-3)$$

this equation can be solved to obtain

$$I(z) = \left(2\gamma z + \frac{1}{I_0^2}\right)^{-\frac{1}{2}}, \quad (3-4)$$

where γ is the 3PA coefficient, I_0 is the irradiance of laser pulse (power per unit area, $E_p/(\tau\pi w_0^2)$), and $I(z)$ is the laser intensity at position z of laser propagation direction inside the ZnO substrate. Equation (3-4) can also be rewritten as

$$d = \frac{(\tau\pi w_0^2)^2}{2\gamma} \left(\frac{1}{E_{\text{cleave}}^2} - \frac{1}{E_p^2} \right), \quad (3-5)$$

where d is the cleavage depth, τ is the pulse duration (700 fs), w_0 is the focused radius (21.5 μm , simulated by Figure 3.3.4 (b)), E_{cleave} is the threshold energy of laser-induced cleavage for our processing system, and E_p is the energy of incident laser pulse. The measured cleavage depth was fitted based on Equation (3-5) and shown in Figure 3.3.6 (a). The 6- μJ irradiated spot was neglected for the fitting because the intensity may be too low to encourage multi-photon absorption[107]. The fitting curve agrees well with the measured results, and we obtained a simulated value of E_{cleave} (8.37 μJ) indicating the minimum pulse energy for laser-induced cleavage. The simulated γ in our work is 5.66 cm^3/GM^2 , which agrees with the result measured by He *et al.* The thermal properties also contribute considerably to the cleavage process; ZnO has a higher thermal-expansion coefficient ($\alpha_{\perp} \sim 5 \times 10^{-6} \text{ K}^{-1}$, $\alpha_{\parallel} \sim 3 \times 10^{-6} \text{ K}^{-1}$ [108 - 110]) and a much lower thermal conductivity ($\kappa < 50 \text{ W} \cdot \text{m}^{-1} \cdot \text{K}^{-1}$ [110-113]) than that of Si ($\alpha \sim 2.6 \times 10^{-6} \text{ K}^{-1}$ [109,114,115], $\kappa \sim 150 \text{ W} \cdot \text{m}^{-1} \cdot \text{K}^{-1}$ [114,116]) at a temperature of ~ 300

K. These thermal properties indicate that a larger expansion in a smaller volume will be induced by laser irradiation in the ZnO substrate than in Si.

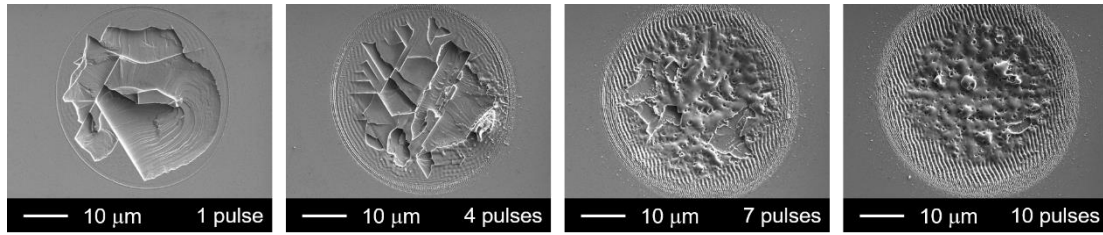


Figure 3.3.7. ZnO surface irradiated by laser pulses with the same pulse energy of 30 μJ but different pulse numbers (repetition rate: 10 Hz).

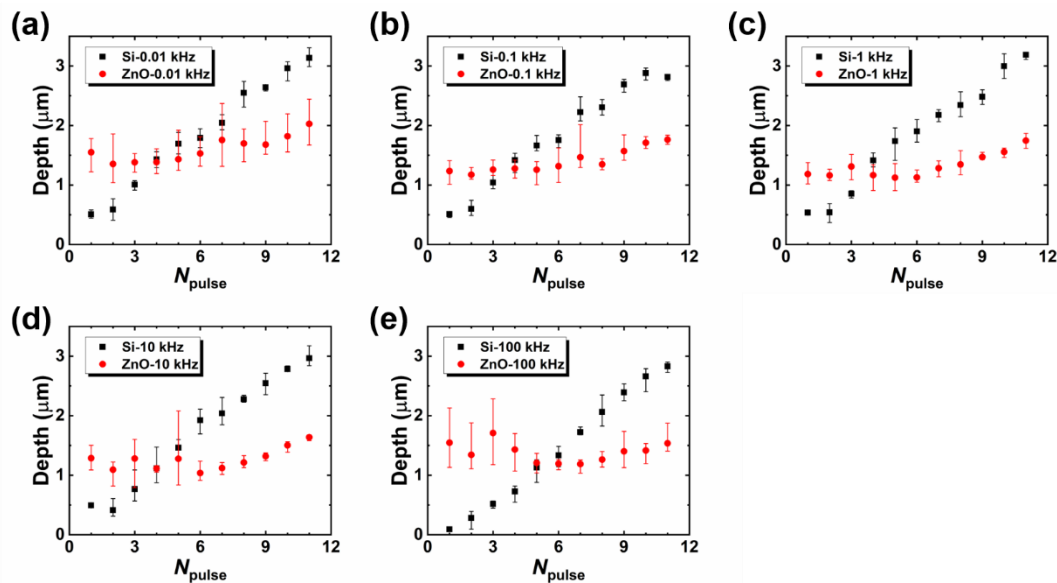


Figure 3.3.8. Depths of the multi-pulse irradiated spots of ZnO (red squares) and Si (black squares) under different repetition rates in the range 0.01–100 kHz ((a)–(e)).

Although the one-pulse irradiated spots showed cleavage marks if the pulse energy was higher than the threshold energy, the laser-induced cleavage did not remain when the same spot was irradiated by multiple pulses. As shown in Figure 3.3.7, when the pulse number reached 4, the conspicuous melt is deposited on the no-cleavage zone, and the melt area increases with pulse number; consequently, the 10-pulse irradiated spot becomes a fully melted surface. This cleavage-melt shift was found for all of the samples under different repetition rates according to their CLSM measurements, and it may be caused by the vestigial heat from initial laser–matter interaction or the change of absorption related to the surface defect arising from previous irradiations. As shown in Figure 3.3.8, the depth of laser-irradiated Si increases almost linearly with the number of pulses. This linear increase indicates that there is no mechanistic change in the ablation process as the pulse number increases. The melting process consistently accompanies the increase of laser pulses. On the other hand, the depth of laser-irradiated ZnO seems to be randomly distributed for pulse numbers less than 5; and from the fifth pulse, the depth linearly increases with the laser-pulse number. The cleavage-melt shift occurred for all samples with laser repetition rates from 10 Hz to 100 kHz. However, the repetition rate is associated with the waiting time for the next pulse, which will vary the cooling time for the irradiated spot between pulses. Hence, when the repetition rate is low enough, the longer cooling time is possible to change the formation process of

the surface defect. So that, the change of repetition rate may not affect the happen of melt-cleavage shift, but it is possible to change the N_{pulse} when the melt-cleavage shift was induced.

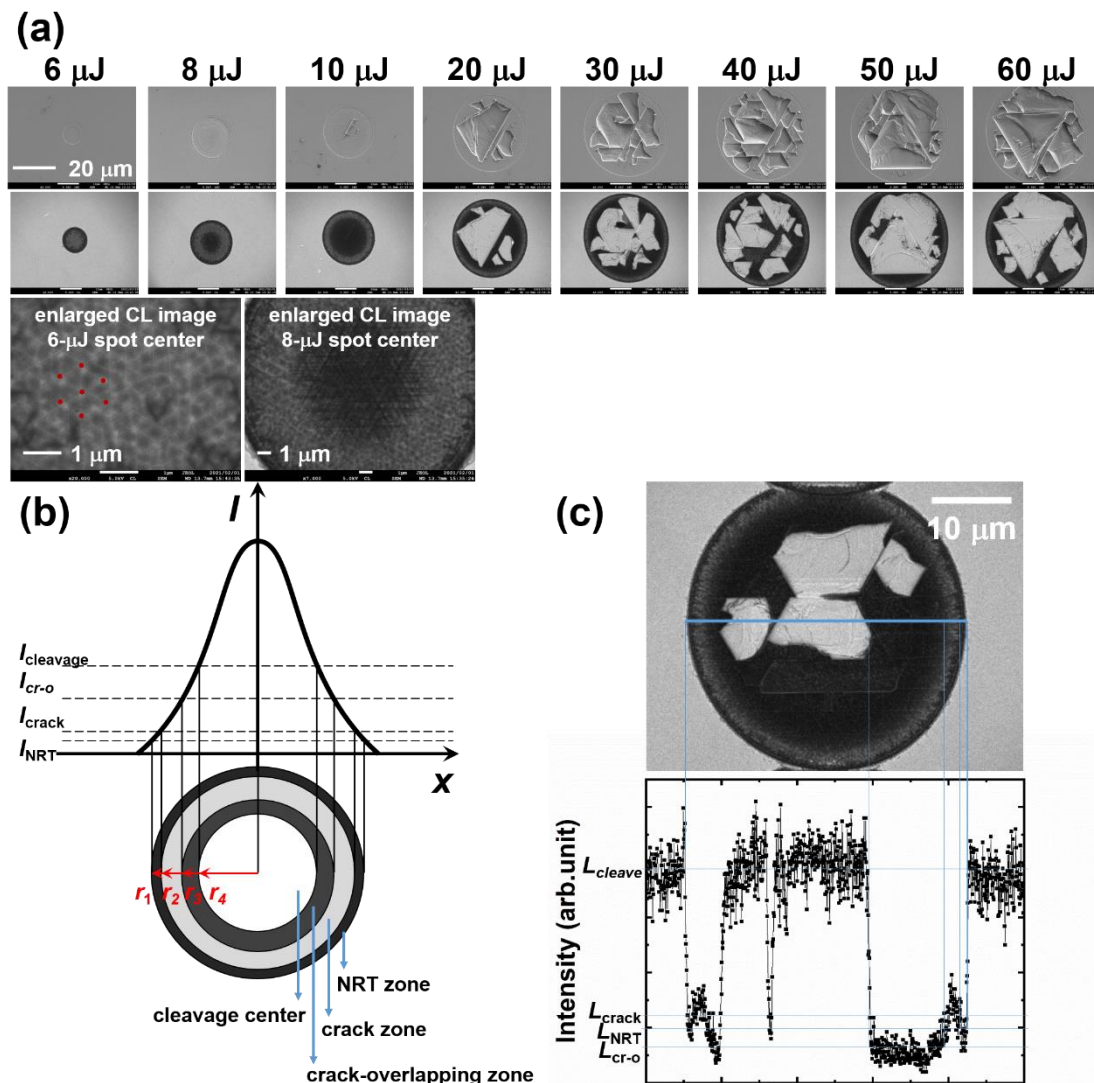


Figure 3.3.9. (a) SEM (top) and CL (bottom) images of the one-pulse irradiated spot. The red points in the enlarged CL image of the 6- μJ irradiated spot are the vertices of the triangles that combine to form the hexagon. The enlarged CL image of the 8- μJ irradiated spot shows a crack-overlapping center surrounded by the crack zone. (b): Image of the cleavage center, crack zone, crack-overlapping zone, and NRT zone of the laser-irradiated spot when the intensity is sufficiently high to induce surface cleavage. (c) The CL image and a line profile of luminescence intensity in a 20- μJ irradiated spot.

Figure 3.3.9 (a) shows the SEM and CL images of one-pulse irradiated spots with different pulse energies. In the enlarged CL image of the 6- μJ irradiated sample, nano cracks with triangular or hexagonal (6 triangular pieces) shapes were observed at the center of the spot. In these nano cracks, luminescence was detected from the edges, but the centers were relatively dusky. 6 μJ is relatively low pulse energy close to the processing threshold (5.66 μJ), which may not be high enough to induce nano cracks inside the ZnO substrate; this suggests that the luminescence should be generated from the exposed ZnO and escape from the shallow cracks. A dark center surrounded by a

round area with higher luminescence intensity (a donut shape) was observed in the CL image of the 8- μJ irradiated spot center, and the enlarged CL image shows that the overlapping cracks constituted the dark center. In a Gaussian beam, the center has the highest intensity and gradually decreases toward the edge. The 8- μJ irradiated center has a higher intensity level than that of the 6- μJ irradiated spot (crack zone), leading to cracks under the surface that result in a crack-overlapping zone. The overlap of cracks can obstruct the escape of luminescence from the inside and constitutes the dark center. Moving outwards from the center of the 8- μJ irradiated spot, the intensity will decrease to the same level of 6- μJ irradiated center, such that a luminous donut with the pattern of triangles and hexagons as seen in the center of 6- μJ irradiated spot is observed surrounding the dark center. Both the 6- and 8- μJ irradiated spots have dark rings in their outermost areas which have the lowest intensity in a laser spot. In this area, the intensity may be too low to induce nano-cracking. Non-radiative defects may arise due to this low-intensity irradiation (as shown in Figure 3.3.9 (b)) and give rise to the dark ring (NRT zone). When the pulse energy is higher than 10 μJ , the area of laser-induced cleavages was observed to increase with the pulse energy, and the exposed surface shows a relatively strong luminescence compared to the surrounding area.

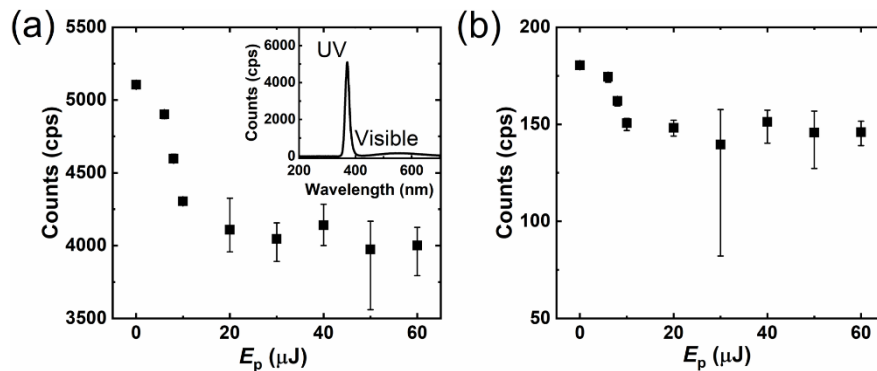


Figure 3.3.10. The intensities of the UV (a) and green-light (b) luminescence of the one-pulse irradiated spots. The error bar using minimum and maximum was obtained from 5 samples. The inserted graph shows the CL spectrum of the unprocessed ZnO surface whose index is 0 J in graphs (a) and (b).

The luminescence properties of ZnO have been reported in detail on numerous occasions[117–126]. The consensus is that UV luminescence should be attributed to the near-band emission, but the visible luminescence associated with various intrinsic defects can show various wavelengths. Figure 3.3.10 shows the intensity of the UV (a) and visible (b) peaks of the one-pulse irradiated samples according to their CL spectra. For the one-pulse irradiated samples, UV emission appeared at 371.5 ± 0.3 nm with a full width at half maximum (FWHM) of 16.3 ± 0.2 nm, while green peak appeared at 549.3 ± 8.0 nm with an FWHM of 179.2 ± 2.8 nm. For the bulk surface, UV emission appeared at 371.6 ± 0.3 nm with an FWHM of 16.3 ± 0.0 nm, while green peak appeared at 556.4 ± 5.6 nm with an FWHM of 177.5 ± 1.8 nm. The green luminescence in our ZnO samples has a similar wavelength to the reports by Zhang et al. [43] and Camarda et al. [125]; it is related to the defects of ionized oxygen vacancies. For both UV and green luminescence, a decrease process was observed when $E_p < 20$ μJ ; for higher pulse energies, the intensity randomly changed with the pulse energy. When $E_p \geq 20$ μJ , the intensity changed randomly, but the average intensity remained at a relatively constant level, which was decreased dramatically from the bare ZnO substrate ($E_p = 0$ J) to $E_p = 20$ μJ .

When the intensity was high enough to induce cleavage, the luminescence intensity should be related to the areas of cleavage center (S_{cleavage}), the crack-overlapping zone ($S_{\text{cr-o}}$), the crack zone (S_{crack}), and the NRT zone (S_{NRT}). Figure 3.3.9 (c) shows a CL image and a line profile of the luminescence intensity for a 20- μJ irradiated spot. The exposed surface has the same luminescence intensity as the unprocessed surface ($L_{\text{surface}}=L_{\text{cleave}}$), which is higher than those of the crack-overlapping, crack, or NRT zones ($L_{\text{surface}}=L_{\text{cleave}}>L_{\text{crack}}>L_{\text{NRT}}>L_{\text{cr-o}}$); because $L_{\text{surface}}=L_{\text{cleave}}$, the detected CL intensity of a cleavage spot is related to $S_{\text{cr-o}}$, S_{crack} , and S_{NRT} .

As shown in Figure 3.3.9 (b), for an ideal laser-induced cleavage surface, the intensity level for cleavage (I_{cleavage}) can be written as

$$I_{\text{cleavage}} = I_0 e^{-2\left(\frac{r_4}{w_0}\right)^2} \quad (3-6)$$

and that for inducing the crack-overlapping zone ($I_{\text{cr-o}}$) can be written as

$$I_{\text{cr-o}} = I_0 e^{-2\left(\frac{r_3}{w_0}\right)^2}. \quad (3-7)$$

According to Equations (3-6) and (3-7), we can obtain

$$S_{\text{cr-o}} = \pi(r_3^2 - r_4^2) = \frac{\pi w_0^2}{2} \ln \frac{I_{\text{cleavage}}}{I_{\text{cr-o}}}, \quad (3-8)$$

where I_{cleavage} is the intensity for inducing the cleavage, $I_{\text{cr-o}}$ is the intensity for inducing the crack-overlapping zone. Here, I_{cleavage} and $I_{\text{cr-o}}$ should be a constant for a settled processing system and a specified material, indicating that the crack-overlapping zone should have an immutable area $S_{\text{cr-o}}$ in an ideally cleaved spot. In the same way, S_{crack} and S_{NRT} can also be obtained as $\frac{\pi w_0^2}{2} \ln \frac{I_{\text{cr-o}}}{I_{\text{crack}}}$ and $\frac{\pi w_0^2}{2} \ln \frac{I_{\text{crack}}}{I_{\text{NRT}}}$, respectively, and independent to the energy of incident laser pulse. The immutability of such areas suggests that an ideally cleaved surface should have a constant intensity of CL luminescence. Due to the formation of the NRT, crack, and crack-overlapping zone, the UV and green luminescence decrease until the pulse energy increase to the level at which surface cleavage is induced. When the pulse intensity is high enough to induce surface cleavage, the crack-overlapping area, crack, and NRT zones will be constant. The surface exposed by cleavage increases with the pulse energy, but the luminescence intensity of the exposed surface is almost the same as that of the unprocessed surface. Consequently, the luminescence intensity will be constant for an ideal laser-induced cleavage surface.

Figure 3.3.11 shows the UV–green ratio of luminescence intensity; for one-pulse irradiated samples (Figure 3.3.11 (a)), this ratio showed a smooth distribution with almost no change as the pulse energy increased. On the other hand, the ratio of multi-pulse irradiated samples (Figure 3.3.11 (b)) started to increase after 4 pulses and saturated at 8. This suggests that the surface-defect state is not overly affected by the pulse energy in one-pulse irradiated samples, but can be changed by multi-pulse irradiation. Figure 3.3.12 shows the UV (a) and green (b) peak intensities of CL luminescence for the multi-pulse irradiated samples. For these samples, UV emission appeared at 372.2 ± 0.4 nm with an FWHM of 17.0 ± 0.6 nm, while green peak appeared at 543.1 ± 4.9 nm with an FWHM of 172.3 ± 3.3 nm. The UV intensity dramatically decreased for the first pulses due to a sudden increase of the crack-overlapping, crack,

and NRT zones. The UV intensity randomly changed from 1 to 3 pulses, continued increasing from 4 to 7 pulses, and saturated at 8 pulses. On the other hand, the intensity of the green peak kept decreasing until saturating at 8 pulses. This result indicates that the defects contributing to green luminescence decreased with the pulse number. Because the similar depth change via N_{pulse} was obtained for the samples irradiated with a repetition rate from 10 Hz to 100 kHz (Figure 3.3.8), an increase-saturation process of $I_{\text{uv}}/I_{\text{visible}}$ (Figure 3.3.11 (b)) can also be predicted for samples irradiated under repetition rates from 100 Hz to 100 kHz.

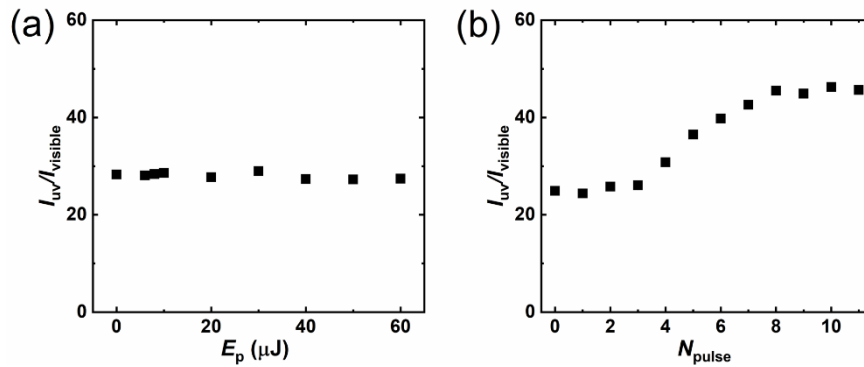


Figure 3.3.11. The intensity ratio of UV and green luminescence. (a) One-pulse irradiated spot; (b) Multi-pulse irradiated spot. The 0-J and 0-pulse samples in the graph indicate the results of unprocessed ZnO.

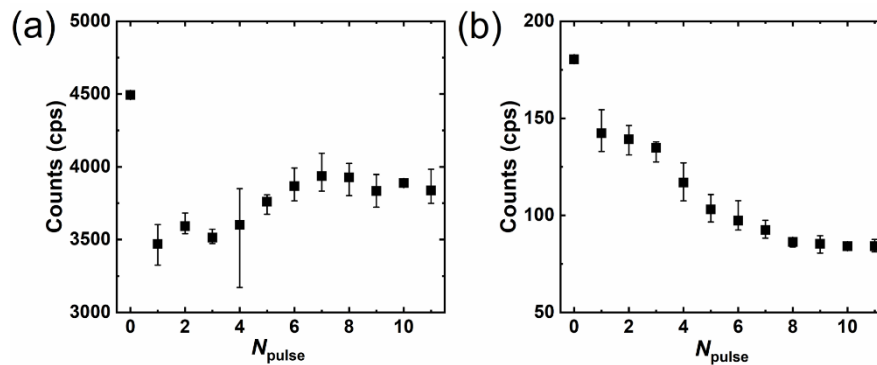


Figure 3.3.12. The intensities of UV (a) and green (b) luminescence for multi-pulse irradiated spots. The error bars using minimum and maximum are obtained from 4 samples. The 0-pulse sample in the graph indicates the result for unprocessed ZnO.

As shown in Figure 3.3.13, before the fourth pulse, laser-induced cleavage is the main phenomenon of laser processing and the randomly exposed surface leads to a variable UV intensity. Meanwhile, the melted material deposited on top of the crack-overlapping, crack, and NRT zones slightly increased with the pulse number. Compared to the bulk surfaces of ZnO, these areas should have a higher absorptivity of laser pulses, causing the melt to be preferentially deposited on these areas. The melted material also showed a relatively high luminescence intensity. After 5-pulse irradiation, the melt increased quickly with the pulse number, and when 8 pulses were irradiated onto the spot, a fully melted surface was formed. As shown in the enlarged SEM and CL images of the 11-pulse irradiated sample, the melting mountain has a smooth surface in the SEM image; however, CL images suggest that the melting mountain is formed by many nano phosphors induced by laser ablation. In the high-temperature, high-pressure center of the irradiated spot, the ablated pieces were heated and melted together. Consequently, the green luminescence in our work is thought to have been caused by transitions from

oxygen-vacancy (V_o) defects to the valance band as V_o decreased with pulse number under laser irradiation in oxygen-rich conditions[120,121,123–125]. After 8 pulses, the fully melted surface was formed and the melted area remained almost changeless while the pulse number increased, leading to saturation of the CL luminescence. The lowest $I_{UV}/I_{visible}$ in Figure 3.3.11 (b) and the highest intensity of green luminescence for the bare ZnO surface ($N_{pulse}=0$) suggest that a bare surface with suitable V_o density may be easier to induce the MPA and the surface cleavage when it is irradiated by ultrafast laser pulses.

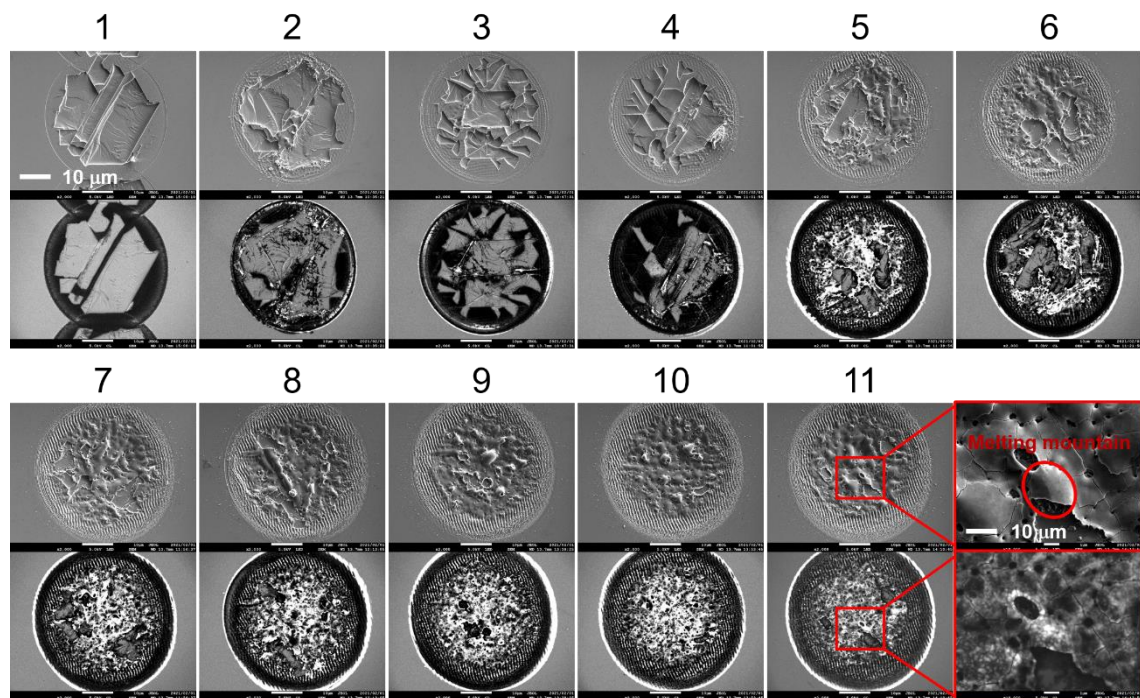


Figure 3.3.13. SEM (top) and CL (bottom) images of multi-pulse irradiated samples. The numbers above the SEM images indicate the number of pulses irradiated upon each sample.

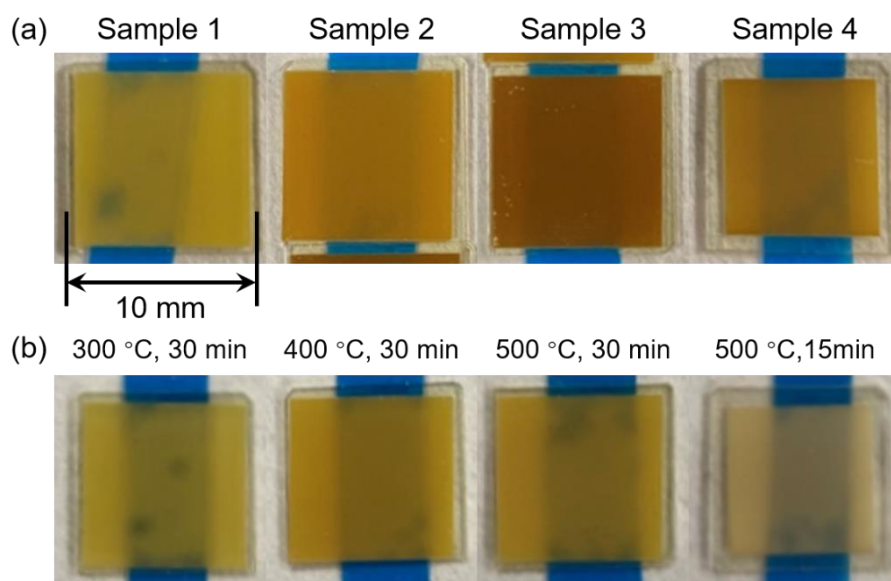


Figure 3.3.14. Images of ZnO moth-eye structures before (a) and after (b) annealing.

Figure 3.3.14 (a) shows the images of ZnO substrates with the moth-eye structure on the surface, and (b) shows their images after annealing in air. The discoloration was observed for samples 2–4 when the temperature is higher than 300 °C. Discolorations in these images indicate that the defect state was changed by annealing in the air for the laser fabricated ZnO moth-eye structures, and the lightening of color (dark brown–light brown) suggests that the transmittance may be increased by the annealing process. The response to THz waves for these four samples was measured by using a standard THz-TDS system (NIPPO PRECISION Co., Ltd.), which has two photoconductive dipole antennae to generate and detect THz waves. Initially, the THz wave was allowed to propagate in a closed box, flowing with dry air to keep the humidity lower than 0.1%. The THz beam was horizontally polarized with a spectral range of approximately 0.1–4.0 THz. The spectral resolution, 0.02 THz, was determined by the inverse of the temporal scan range of 50 ps, whereas the diameter of the THz beam spot was approximately 3 mm. The THz waves were irradiated to the modified surface of the samples at a normal incidence (the propagation direction is vertical to the sample) and detected after passing through the samples. All the measurements were conducted in TM mode (in which the direction of the electric field of the incident THz wave is perpendicular to the groove parallelly arranged). The time-domain signals are measured 100 times for each sample, as well as the paired bare ZnO substrate for reference. The spectrum intensities of these samples were obtained by taking the Fourier Transform of the THz-TDS waveform. A time window of 6.66 ps (2.22 ps before and 4.44 ps after the first dip) was selected for removing the Fabry-Perot fringes causing by the multi-reflected signal[53].

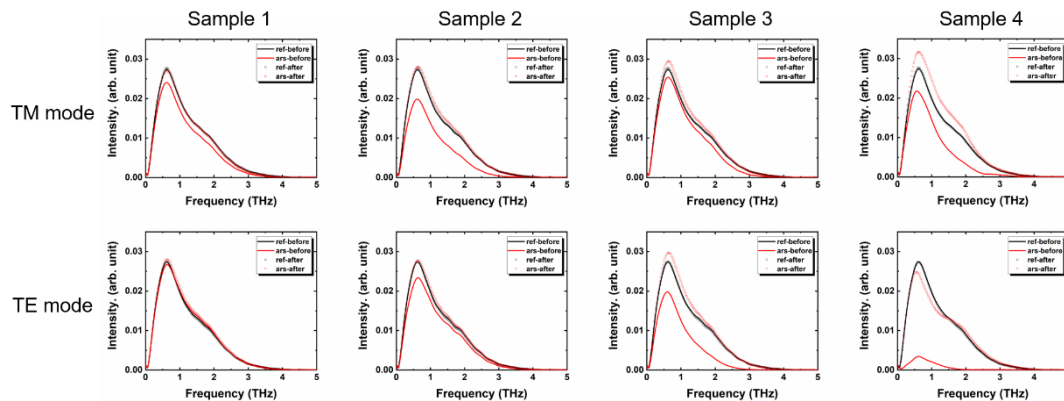


Figure 3.3.15. Spectrum intensities of ZnO moth-eye structures. Black denotes the bare ZnO surface, and red denotes the ZnO moth-eye structures. Lines denote measured results of samples before annealing, and empty squares denote the measured results of samples after annealing.

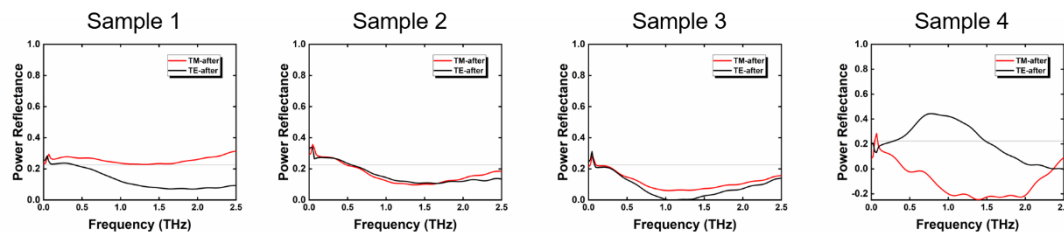


Figure 3.3.16. Calculated power reflectance according to the spectrum intensity showing in Figure 3.3.15. The gray line denotes the power reflectance of an unprocessed ZnO surface (22.4%).

The measured spectrum intensities (average of 100 measurements) of these ZnO substrates with and without moth-eye structures are shown in Figure 3.3.15. There is almost no change in the measurement of the unprocessed ZnO, but all the samples show have an improvement of the transmitted intensity after annealing. The measured spectrum intensities of ZnO substrates with and without moth-eye structures were compared to obtain the power reflectance of the fabricated AR structures according to Equation (2-13). Figure 3.3.16 shows the calculated power reflectance according to the spectrum intensity showing in Figure 3.3.15. Most of the samples showed a broadband AR feature except sample 1 in TM mode and sample 4 in TE mode. An ideally fabricated 2D structure should have the same power reflectance for TE and TM mode due to the same profile from both horizontal and vertical section view, but the measured results showed different power reflectance in TE and TM mode for samples 1–3. This difference in reflectance distributions may be caused by the difference in profiles of horizontal and vertical directions. The profile was affected by the deposition of debris during the laser ablation, which is associated with the scanning pattern. Sample 4 shows a negative power reflectance, which means the measured transmittance increased even higher than the theoretical calculation. This increase of transmittance may be caused by the decrease of inherent defects during annealing, and the unprocessed ZnO substrate used for reference was not annealed. Nevertheless, annealing in the air is an efficient way to improve the laser-fabricated moth-eye structures on the ZnO surface.

3.3.4 Conclusion (ZnO-based moth-eye structure)

In summary, laser-induced cleavage on the bulk ZnO surface was observed under single-pulse irradiation (wavelength: 1,030 nm, pulse duration: 700 fs). A three-step process of multi-photon absorption, expansion, and cleavage was proposed for the laser-induced cleavage of ZnO. When ZnO is irradiated by laser pulses with a 1030-nm wavelength, the 3PA due to the wide bandgap will be predominate and results in surface cleavages. This 3PA-induced surface cleavage differs from the general melt process caused by 1PA that occurred on the surface of Si or other metals. The pulse-energy-dependent cleavage depth was quantitatively analyzed by a 3-photon absorption model, and the 3-photon absorption coefficient was calculated to be $5.66 \text{ cm}^3/\text{GW}^2$. The cleavage-melt shift of laser processing on the surface of the ZnO substrate was observed and characteristically analyzed in terms of the change of the surface-defect states during multi-pulse irradiation. The laser-induced cleavage process will be caused by 3PA of the first pulse; then, a mixed process of cleavage and melt occurs from 2 to 4 pulses, resulting in the formation of the crack-overlapping, crack, and NRT zones with absorptions higher than that of the unprocessed surface; after four pulses, the general laser-induced melt process comes to dominate. Moreover, the intrinsic defect of V_o decreased with the input of the pulse number, which could decrease the intensity of green luminescence and increase the UV–visible ratio of luminescence intensity. Additionally, surface cleavage could be possibly induced on other wide-bandgap materials by MPA under ultrafast laser irradiations, for example, gallium nitride, which also has cleavability and a wide bandgap of 3.4 eV. These results can potentially be used to extend femtosecond laser-based surface-modification processing methods, or to design laser-induced functional surfaces of ZnO or other wide-bandgap materials with wide bandgap and suitable thermal properties (i.e., a high thermal expansion coefficient and low thermal conductivity). Although without any post-processing, the laser-fabricated ZnO moth-eye structures did not achieve the desired AR performance, it was

demonstrated that the AR performance can be improved by annealing such structures in the air.

3.4 Conclusion

By applying the moth-eye structure on the reverse of GaAs PC antenna, reflectance loss was successfully reduced when the THz waves were generated from a THz wave combiner. The output of this compact device was successfully improved by increasing the extraction efficiency, instead of improving the generating ability. Due to the improvement of crystallinity by annealing in the atmosphere, the transmittance is successfully improved for the laser-fabricated moth-eye structure on ZnO substrate, which is a wide bandgap material with various defect levels. These results suggest that moth-eye structure is a useful method to reduce the reflectance for various materials-based THz devices besides Si.

Chapter 4

Profile control of moth-eye structures

4.1 Introduction

Frequency bands within 275 – 450 GHz to be used for THz communication in the operation of fixed and land mobile service application have been specified during the World Radiocommunication Conference 2019[127], which offered an opportunity to satisfy the Tbps data rate demand of the next generation (6G) of the mobile communication system. However, there remain challenges such as path loss during the THz wave propagation and atmospheric absorption that cross the full utilization of THz radiation and that should be overcome[21,128–130]. Furthermore, despite the difficulty in increasing the output of THz light sources, materials generally used in this region have a relatively high refractive index associated with high reflection loss because of the sudden change in the interface between air and the THz optical components. Moth-eye structure is useful for antireflection in the THz region, but further work needs to be done for applying such structures for some specific applications. Increasing the aspect ratio can indeed efficiently make the refractive index changing smoothly, consequently, reduce the power reflectance. Nevertheless, the vulnerability limits the employing of a high aspect ratio for moth-eye structures. The effective refractive index (n_{eff}) changing can also be adjusted by adjusting the profile of such microtapers. In this chapter, one-dimensional (1-D) periodic-tapered structures having varying profiles and aspect ratios on high-resistivity silicon substrates were fabricated by femtosecond laser processing. The AR characteristics of these structures are evaluated using a standard THz time-domain spectroscopy (THz-TDS) and then numerically simulated by employing the method of Finite-difference time-domain (FDTD). It will be shown later that there is a corresponding agreement between the results of measurement and simulation, with the different profiled structures displaying various power reflectance distributions against the frequency in the THz region, especially for the low reflection (<5%) region within 0.5–1 THz. Accordingly, these results confirm that the AR characteristics can be controlled by adjusting the profile of the micro-tapers of the 1-D moth-eye structures, and these characteristics are related to the n_{eff} distribution. The relationship between the n_{eff} distributions and the AR improvement is also quantitatively analyzed, and the results can be considered as a valuable reference for the design of AR structures in the THz region. On a positive note, these results would not only enhance the use of femtosecond laser processing as a precise surface modification method but also improve the flexibility of AR designs for various scientific and industrial applications in the THz region.

4.2. Material and Methods

4.2.1 Fabrication of moth-eye structures

The moth-eye structures were fabricated by applying femtosecond laser pulses (D1000, IMRA America, Inc.; center wavelength, 1045 nm; pulse width, 700 fs; repetition rate, 100 kHz) onto the surface of a high-resistivity silicon substrate [plane

orientation: (1 0 0); electrical resistivity, 1 k Ω ·cm; thickness, 0.795 \pm 0.005 mm] by an F-theta lens with a focal length of 100 mm. A schematic of the experimental setup of the laser processing system is shown in Figure 4.1; here, the rotation of the galvanometer mirrors allows a rated scanning speed of approximately 3 m/s on the substrate surface. Meanwhile, a different pattern for various laser-ablated grooves is shown in Figure 4.2. Grooves 40 μ m wide (approximate to the spot diameter of the focused laser beam) could be easily obtained by a single-line scan of 6 μ J laser pulses [Figures 4.2 (a) and (d)], whereas the bigger grooves could be fabricated by overlapping the scan lines as a sequence of channels [61,131]. Subsequently, sequence scanning was conducted on the finished groove scanned by a single-line pattern [Figure 4.2 (b)]. Meanwhile, a branch structure with some molten materials appeared on the bottom left [Figure 4.2 (e)], most likely because of the reflection of the inner surface of the right side. The successively irradiated laser pulses appeared to be influenced by the previously formed structure; thus, to avoid such an influence, sequence scanning was conducted initially once and then fully repeated to create a deeper groove with greater width [Figures 4.2(c) and (f)]. Through careful adjustments of the scanned pattern (by n repetitions in channel duration Δ and channel number m , as shown in Figure 4.2), periodically arranged tapers with four types of profile and with component remnants after laser ablation (i.e., the remained Si between the grooves) were successfully fabricated.

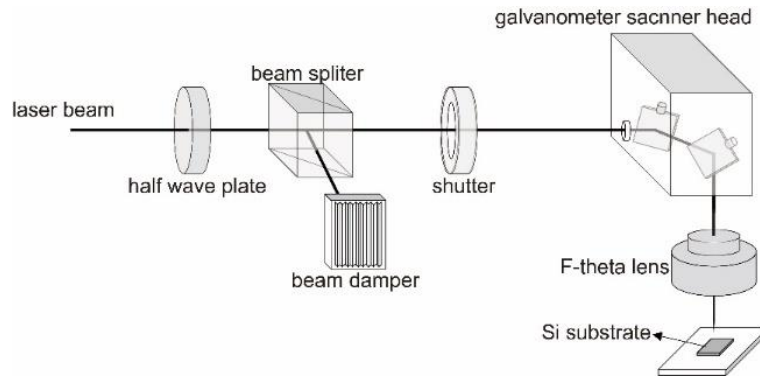


Figure 4.1. Schematic of the femtosecond laser processing system.

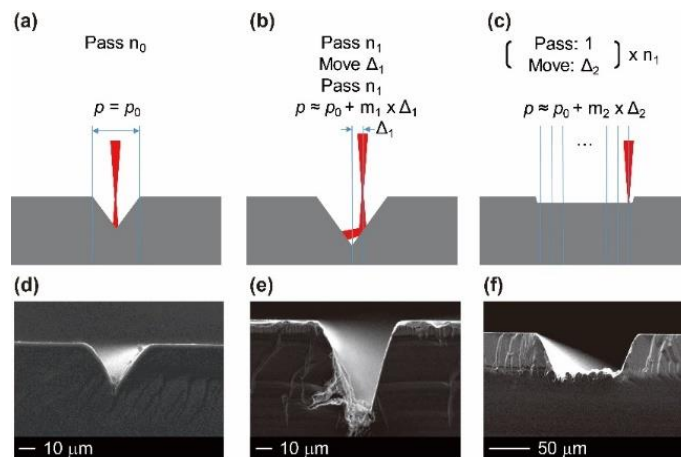


Figure 4.2. (a–c) Sectional views of the scanning pattern of grooves fabricated by laser ablation. (d–f) SEM images of the fabricated grooves. (a) and (c) shows a single-line pattern, with the laser beam scanning vertically to the section images. (b) and (e) show the width (p) of the expanded pattern, where the expanding scan is conducted after the

structuring of the initial single-line sacred groove. (c) and (f) show the expanded pattern, where the expanding scan is repeated with the single-line scan.

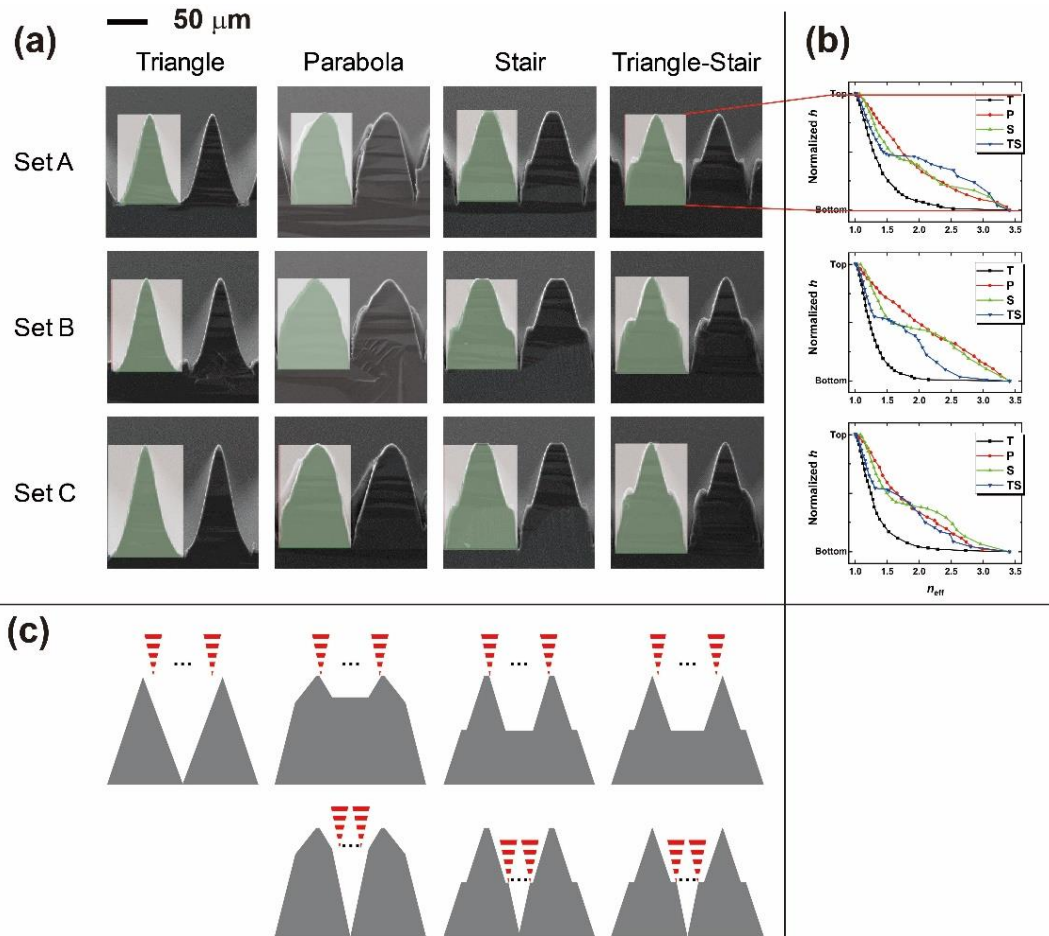


Figure 4.3. (a) Sectional SEM images of tapers with different profiles. The green parts show the profile of simulation models plotted from the SEM images. (b) Plots of the n_{eff} distribution of the three tapers according to the normalized height from top to bottom (h : depth of groove). (c) Scanning pattern for the tapers with different profiles.

Table 4.1. Measured depth and pitch of tapers with different profiles (unit: μm)

SET	Triangle	Parabola	Stair	Triangle-Stair
A	114.9/78.5	114.9/77.2	114.5/80.2	114.0/77.6
B	114.5/93.0	111.4/92.1	114.0/92.5	117.1/92.5
C	134.6/92.1	125.9/91.7	134.2/93.0	134.6/93.0

Figures 4.3 (a) and (c) show the scanning electron microscope (SEM) images of tapers having different profiles (triangle (T), parabola (P), stair (S), and triangle–stair (TS)) and their respective fabrication processes under the break line. Note that the T profile tapers were fabricated simply by the sequence scanning, whereas P, S, and TS profile tapers had to undergo a two-step process. In the case of the P profile tapers, they were fabricated first using an approximately 20- μm -depth groove with a flat bottom, followed by a relatively narrow sequence scanning. The TS pattern was based on the T pattern and gave a different depth of the first groove approximated to $h/2$, where h is the depth of the tapers. Furthermore, the S pattern displayed a 15 μm larger period of

grooves than the TS pattern to obtain a 15 μm flat top. Sets A–C were designed with different depth sizes and pitch (p), such that set A: $h/p = 120 \mu\text{m}/80 \mu\text{m}$, set B: $h/p = 120 \mu\text{m}/95 \mu\text{m}$, and set C: $h/p = 140 \mu\text{m}/95 \mu\text{m}$. The size details of the tapers are summarized in Table 4.1. All the profile-controlled samples were fabricated to an area of $8 \text{ mm} \times 8 \text{ mm}$, and their processing times ranged from 40 to 60 min depending on the scanning pattern.

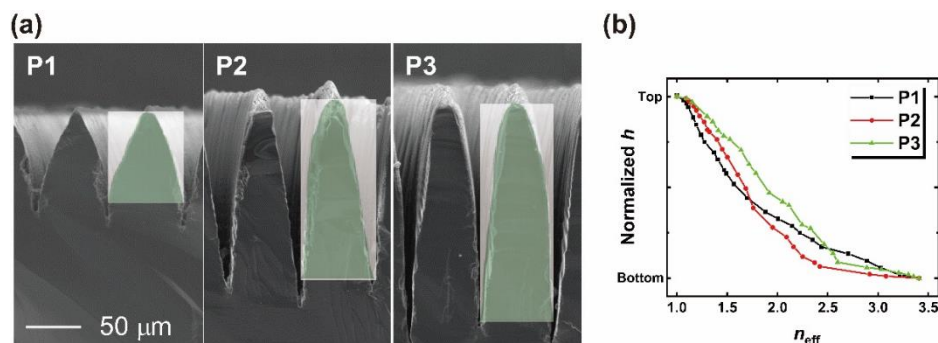


Figure 4.4. (a) SEM images and simulation models of samples P1, P2, and P3 and their n_{eff} distributions (b). The green parts show the profile of simulation models plotted from the SEM images.

Another parameter that contributes to the improvement of the AR characteristics of moth-eye structures is the aspect ratio (h/p). Three samples reflecting different aspect ratios of 1.20, 2.46, and 3.14 were fabricated using a high-power femtosecond laser (TruMicro 5050, wavelength 1030 nm; pulse width: 900 fs; repetition rate: 100 kHz; and max power: 40 W), although the sample pitch of $65 \mu\text{m}$ was fabricated by the single-line scan pattern in Figure 4.2(a) irradiating $50 \mu\text{J}$ pulses. The laser beam was focused by an F-theta lens with a focal length of 150 mm and scanned at a rated speed of appx. 1 m/s. These three samples were fabricated to display an area of $10 \text{ mm} \times 10 \text{ mm}$. The processing times for P1, P2, and P3 were 13, 38, and 57 min, respectively. Figure 4.4 (a) shows the SEM images and simulation models of samples for the P set, and their n_{eff} distributions are shown in Figure 4.4 (b).

4.2.2 Evaluation of the moth-eye structures

The AR characteristics of the tapered structures were measured by using a standard THz-TDS system (NIPPO PRECISION Co., Ltd.), which has two photoconductive dipole antennae to generate and detect THz waves. Initially, the THz wave was allowed to propagate in a closed box, flowing with dry air to keep the humidity lower than 0.1%. The THz beam was horizontally polarized with a spectral range of approximately 0.1–4.0 THz. The spectral resolution, 0.02 THz, was determined by the inverse of the temporal scan range of 50 ps, whereas the diameter of the THz beam spot was approximately 3 mm. The THz waves were irradiated to the modified surface of the samples at a normal incidence (the propagation direction is vertical to the sample) and detected after passing through the samples. All the measurements were conducted in TM mode (in which the direction of the electric field of the incident THz wave is perpendicular to the groove parallelly arranged). The time-domain signals are measured 100 times for each sample, as well as the paired bare silicon substrate for reference. The spectrum intensities of these samples were obtained by taking the Fourier Transform of the THz-TDS waveform. A time window of 10 ps (3.33 ps before and 6.67 ps after the first dip) was selected for removing the Fabry-Perot fringes causing by the multi-

reflected signal[53]. The spectrum intensities of these samples are shown in the top part of each cell in Figure 4.5 (profile-controlled samples) and Figure 4.6 (samples of set P). The measured spectrum intensities (average of 100 measurements) of the Si substrates with and without tapered structures were compared to obtain the power reflectance of the fabricated AR structures. Based on the thickness of the Si substrate, the reflection and transmission from both sides of the sample were considered in the calculations[49,54]. Furthermore, the THz transmission singles $A_{si}(E_{o,si}/E_i)$ and $A_{ar}(E_{o,ar}/E_i)$, through the Si substrates with and without the grating structures, were measured and compared. Here, E_i is the incident signal, and $E_{o,si}$ and $E_{o,ar}$ are output signals transmitted by the Si substrate without and with the AR structure, respectively. The power reflectance R_{ar} is given by

$$R_{ar}(f) = 1 - \frac{4|n|}{|1+n|^2} \left(\frac{A_{ar}(f)}{A_{si}(f)} \right)^2 e^{2n_i k_0 h_{eff}}, \quad (4-1)$$

where n is the complex refractive index of Si, $n = n_r - jn_i = 3.407 \pm 0.0028 - j0.00077 \pm 0.0012$ in the 0.1–2.5 THz frequency range, k_0 is the wavenumber of the THz wave in vacuum, and h_{eff} is the effective height of the AR structure, which is determined by the difference between the measured phases of A_{ar} and A_{si} according to $\Delta\phi = n_r k_0 h_{eff}$. A thorough explanation of the derivation procedures for Equation (4-1) can be found in[54]. Substituting $\Delta\phi$ to the exponential term, $e^{2n_i k_0 h_{eff}} = e^{2\frac{n_i}{n_r} \Delta\phi}$. Because in the range from 0.1 – 5 THz, $\Delta\phi < 4$ rad in our measurement, the term of $e^{2\frac{n_i}{n_r} \Delta\phi} \sim 1$, so that Equation (4-1) can be written as

$$R_{ar}(f) = 1 - \frac{4|n|}{|1+n|^2} \left(\frac{A_{ar}(f)}{A_{si}(f)} \right)^2. \quad (4-2)$$

From the 100 measurements of each sample, we obtained the standard deviation of A_{ar} (σ_{ar}) and A_{si} (σ_{si}). Because the power reflectance has a function with variation A_{ar} and A_{si} ($R = f(A_{ar}, A_{si})$), the standard deviation of the power reflectance (σ_{si}) can be calculated as

$$\sigma_{ar} = \sqrt{\sigma_{ar}^2 \left(\frac{\partial R}{\partial A_{ar}} \right)^2 + \sigma_{si}^2 \left(\frac{\partial R}{\partial A_{si}} \right)^2} \quad (4-3)$$

According to the sectional SEM images of the samples, simulation models were applied to obtain a simulated power reflectance for reference. The profiles of the simulation models are inserted into the SEM images of each sample in Figures 4.3 (a) and 4.4 (a). The measured and simulated results are showing in the bottom part of each cell of Figure 4.5 and Figure 4.6 for the profile-controlled samples and P-set samples.

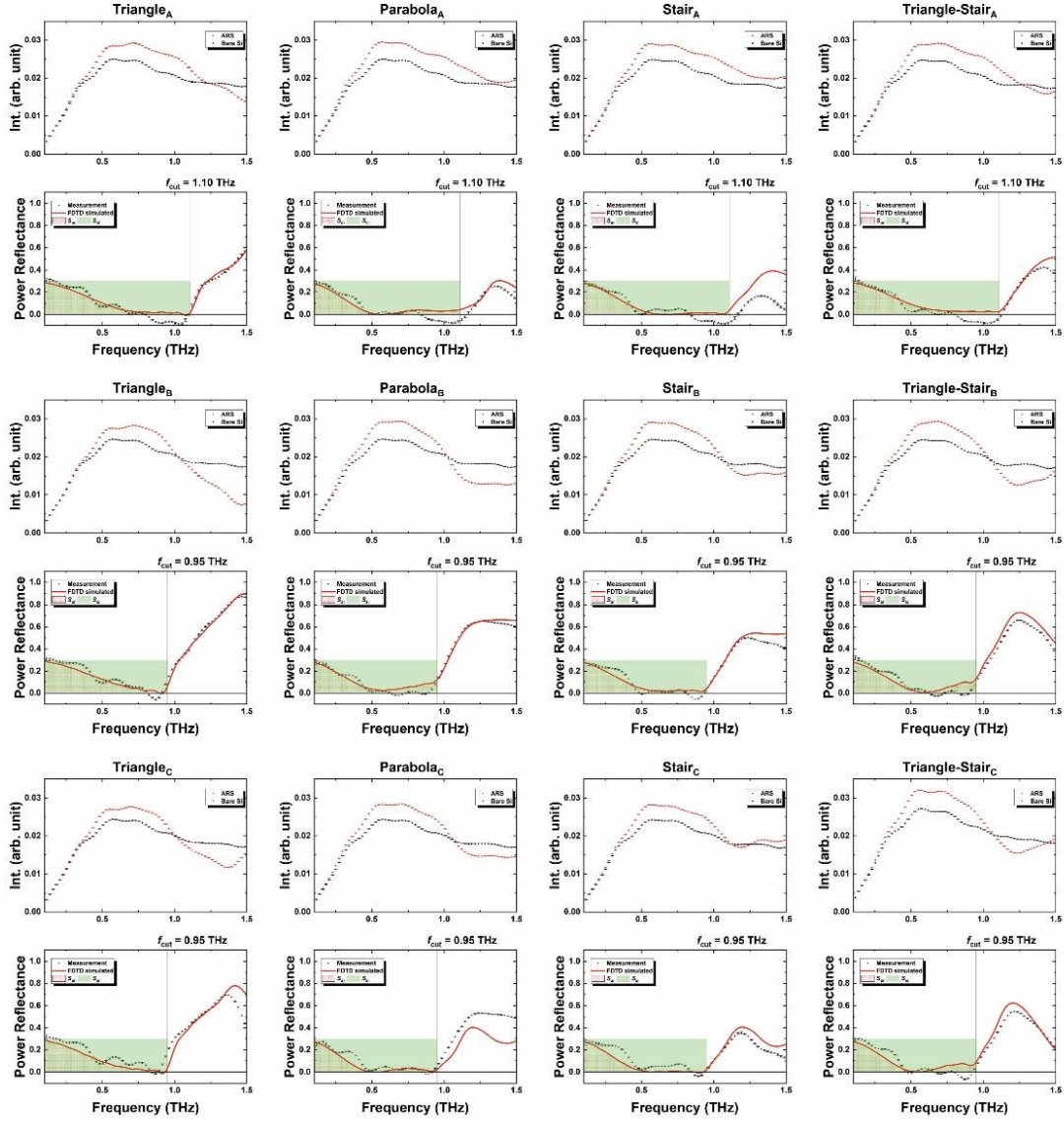


Figure 4.5. Spectrum intensity, power reflectance obtained from THz-TDS measurements, and the simulation results for profile-controlled samples. The top part of each cell is the spectrum intensity of samples with different profiles (red dots) and their reference (black dots). The bottom part of each cell is showing the calculated power reflectance (black dots) and the simulated results (red line). Red gratings are the integrated area ended at the cut-off frequency according to the simulated power reflectance of AR structures, and the green squares show that of the bare Si substrate. The error bar is the standard deviation obtained from 100 measurements.

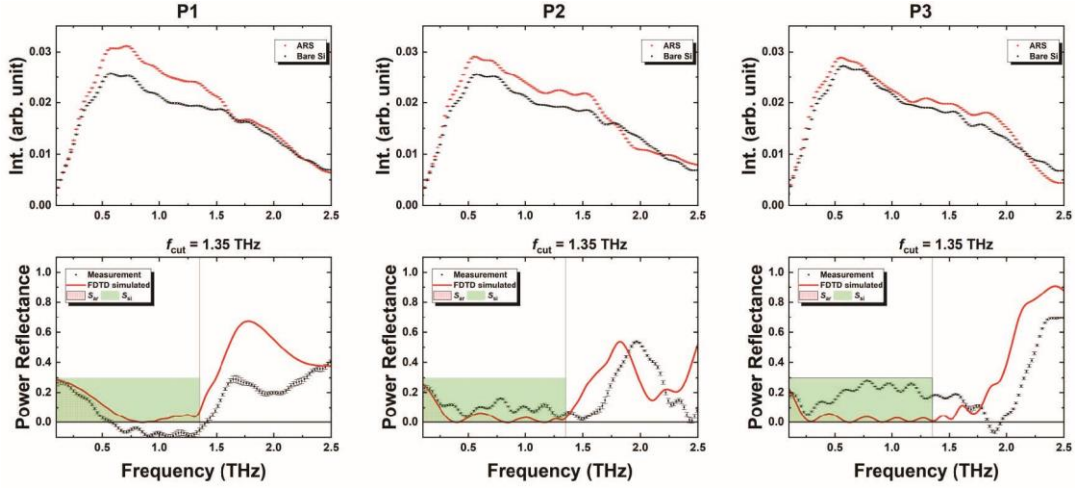


Figure 4.6. Spectrum intensity, power reflectance obtained from THz-TDS measurements, and the simulation results for samples with different aspect ratios.

4.3 Results and discussion

As shown in Figure 4.3(a), the tapers having four different profiles and sizes were successfully fabricated by carefully adjusting the scan pattern. To calculate n_{eff} , the equation

$$n_{\text{eff}} = \sqrt{\frac{\epsilon_{\text{si}}}{g_{\text{si}} + \epsilon_{\text{si}}(1 - g_{\text{si}})}} \quad (4-4)$$

was used[72]. The sectional SEM images also illustrated the n_{eff} distributions of these tapers plotted to the normalized height [Figure 4.3 (b)]. Accordingly, the tapers with different profiles displayed significant differences in n_{eff} distribution. Among the four taper profiles, T experienced a dramatic change, where almost 85% of the n_{eff} was changed along with the lower 25% part of the height. Meanwhile, P showed a relatively smooth n_{eff} change along with the taper height, whereas both S and TS had a buffer step around the middle of the taper height, with S reflecting a smoother change in the top of the taper, which is the interface of air to the taper.

Spectrum intensity and power reflectance distribution of the moth-eye structures with different n_{eff} distributions and sizes are shown in Figure 4.5. Graph title of each cell is the profile of the sample, and subscripts of the titles mean the set (size) of the sample. According to the spectral properties, the transmitted THz signals are much stranger than that of the bare Si substrate in broadband. It can be observed that the measured THz-TDS results agreed well with the simulated results for all samples (Figure 4.5, bottom parts of each cell). Furthermore, as the pitch approached the order of THz wavelength, the power reflectance starts increasing, which should be caused by the negative interference of THz waves with shorter wavelengths. Figure 4.7 is showing the electric field distribution at 1.03 THz (the minimum of R distribution) and 1.58 THz (the first peak after f_{cut}) for sample Triangle_A. Strong interference can be observed at 1.58 THz, but the 1.03-THz wave transmitted the substrate without any interference. Therefore, each sample showed a specific cut-off frequency, above which, the diffraction will reduce the transmission of THz waves. On one hand, the tapers of set A had $p=8.9\pm 1.3 \mu\text{m}$ associated with a cut-off frequency (f_{cut}) of 1.11 THz, $f_{\text{cut}}=c/(p \times n_{\text{si}})$,

where c is the speed of light[49,54]. On the other hand, the tapers of sets B and C yielded $p=92.4\pm 0.6 \mu\text{m}$ and a cut-off frequency of 0.95 THz.

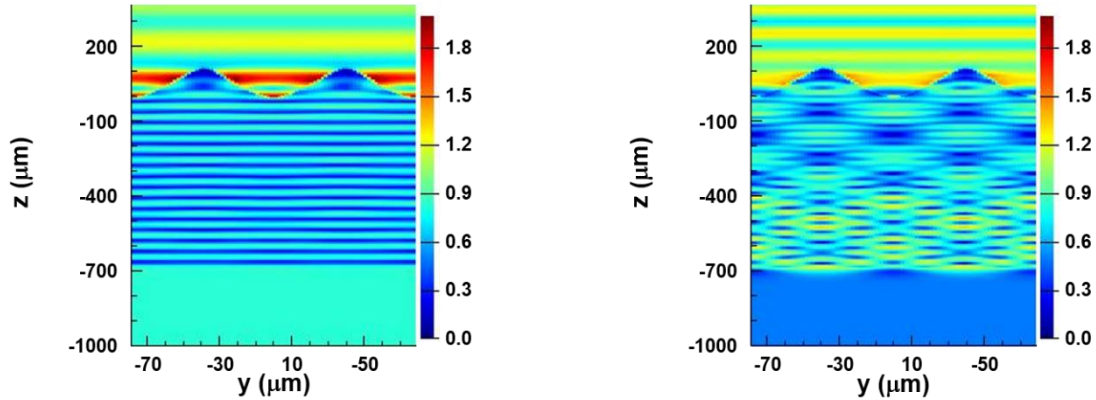


Figure 4.7. The electric field distribution of 1.03 THz (a) and 1.58 THz (b) for sample Triangle_A, where the minimum and the first peak after f_{cut} appeared, respectively.

For the high THz frequencies (1–1.5 THz), the simulated results start slipping away from the experimental results. This may be caused by the variation of the taper profile during the fabrication, i.e. un-uniformity of the depth of the grooves, debris deposited on the top of the taper, and the entrance of the grooves, while we choose just one taper from the hundreds of tapers in one sample. Although we plot the profile from the SEM image of the laser fabricated tapers, it still has some subtle differences in the profiles between the plotted and the fabricated ones. As showing in Figure 4.3(a), the non-negligible difference in the profiles and variation of the depth can be observed from SEM images. Likewise, THz waves emitted from the THz-TDS system are broadband, so that, the wavelength is very different in the measured range. THz waves with longer wavelength (low-frequency region) maybe not so sensitive to the subtle difference as the waves with shorter wavelengths. Consequently, experimental results in the low-frequency region match the simulated results better than results in the high-frequency region. The surface defect should also be considered for the mismatch of experiment and simulation results. Laser ablation provides a high-temperature and high-pressure condition at the laser-focused spot. This can promote the formation of amorphous Si and the reaction of laser-ablated Si debris with oxygen in the air. On the contrary, the material used in simulations has a constant refractive index of $n=3.407-j0.00077$, which is measured by the THz-TDS system. It could be inferred from the simulated results that the power reflectance of the samples with T profiles increased dramatically as soon as the minimum was achieved, whereas the other samples exhibited a relatively stable reflectance distribution after the first minimum. Particularly, these samples maintained a power reflectance of less than 5% in the 0.5–1.0 THz range, especially for the S-profiled samples, which almost provided a flat reflectance distribution between the first minimum to the cut-off frequency and where the power reflectance was reduced to almost 0.

Figure 4.4 (b) shows the n_{eff} distribution of the moth-eye structures with different aspect ratios but the same pitch of $65 \mu\text{m}$ with a f_{cut} of 1.35 THz. The three samples showed similar n_{eff} distributions, which also resembled those of the P-profiled tapers. Their spectrum intensities (top parts) and power reflectances (bottom parts) are shown in Figure 4.6. Sample P1 has a negative power reflectance in the measured results, which means the measured transmittance increased even higher than the theoretical calculation. The refractive index of Si may be changed during laser processing. In the

high-temperature-high-pressure center of pulsed laser-induced plasma, the ablated Si particles will be oxidized when the target was exposed to the air during the processing. The Refractive index of silicon oxide is lower than Si, which is associated with a higher power transmittance in the calculation. Consequently, the decreased refractive index may be contributed to the negative value of the power reflectance. Before the cut-off frequency, the measured result of P2 matches the simulation well, but the measured result of P3 has a higher power reflectance than that of the simulation. For both P2 and P3 the simulated results start slipping away from the experimental results. These may be caused by the difference of profiles between the ideally created model of the simulation and the laser fabricated tapers. To obtain a higher aspect ratio, P2 and P3 were irradiated by more laser pulses than P1, hence P2 and P3 have more molten materials randomly deposited both on the top of the taper and the inner surface.

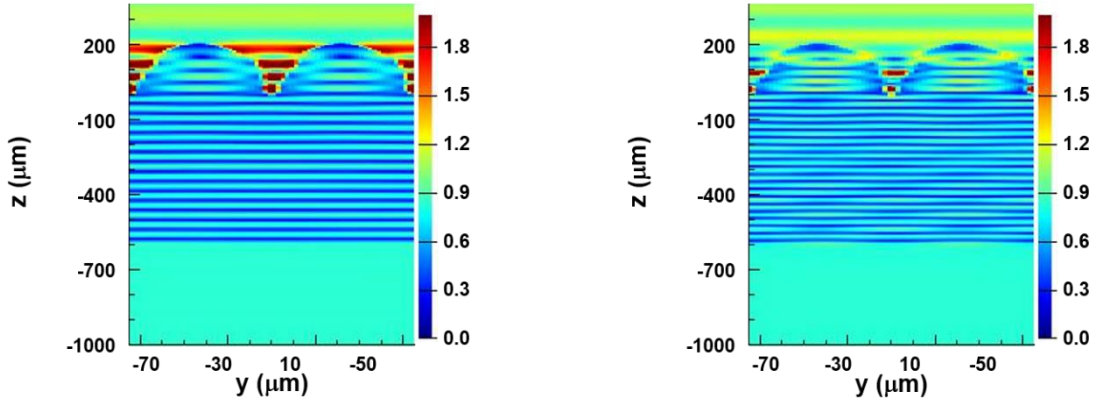


Figure 4.8. The electric field distribution of 1.15 THz (a) and 1.51 THz (b) for sample P3, where a dip of the power reflectance appeared before and after the cut-off frequency, respectively.

Interestingly, different from the simulated results of other samples, the power reflectance of P3 did not increase directly after the cut-off frequency of 1.35 THz. A dip at 1.51 THz can be observed. The electric distribution of P3 at 1.15 THz and 1.51 THz are shown in Figure 4.8, where a dip of the power reflectance appeared before and after the cut-off frequency, respectively. Different from the electric distribution of 1.58 THz in Triangle_A ($f_{\text{cut}}=1.11\text{THz}$) shown in Figure 4.7 (b), 1.51 THz in P3 has a very weak interference during the propagation in the substrate after entering from the AR structures. This result indicates that P3 has a higher cut-off frequency than P1 and P2 ignoring the same pitch of 65 μm . The AR structure (groove–taper–groove) can be considered as a waveguide (air–Si–air). P3 has a depth of 204 μm which is larger than the depth of P1 (78 μm) and P2 (159 μm), and the depth of P3 is about 3.5 times larger than the wavelength of 1.51 THz in Si substrate (58 μm). The bottom part with a width near 65 μm of P3 is the largest of these three samples. It means that P3 has a larger effective width than the others, which can couple more THz waves into the structure.

Generally, the total reflection of a taper $\Gamma(\theta)$ can be obtained by summing all the partial reflections with their appropriate phase shifts[132] as follows:

$$\Gamma(\theta) = \frac{1}{2} \int_0^h e^{-2j\beta x} \frac{d}{dx} \ln \left(\frac{Z(x)}{Z_0} \right) dx \quad (4-5)$$

where $\theta=2\pi h$, h is the height of the taper, $Z(x)$ is the effective impedance distribution of the taper, Z_0 is the vacuum wave impedance, and x is the height of each position. If

$Z(x)/Z_0=1/n(x)$, where $n(x)$ is the refractive index distribution of the taper, Equation (4-4) can be redefined into

$$\Gamma(\theta) = -\frac{1}{2} \int_0^h e^{-2j\beta x} \frac{dn(x)/dx}{n(x)} dx \quad (4-6)$$

where $\frac{dn(x)/dx}{n(x)} = \frac{n'(x)}{n(x)}$ indicates the refractive index change in each minute-divided part.

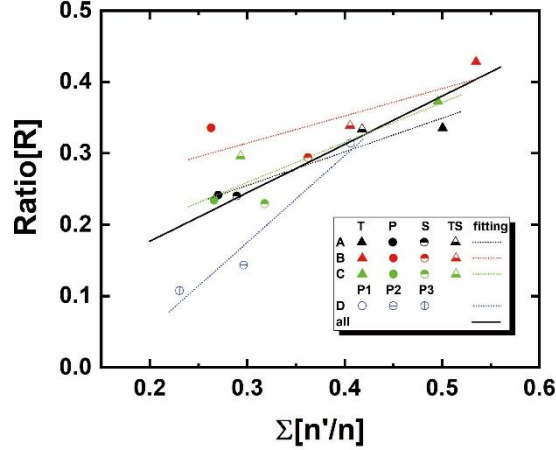


Figure 4.9. Relationship between the AR characteristics and the n_{eff} distribution characteristics.

If $n(x)$ is known, $\Gamma(\theta)$ can be found as a function of frequency, indicating that the refractive index distribution is the main parameter influencing total reflectance. The relationship between the AR characteristics and the n_{eff} distribution is shown in Figure 4.9. Here, the vertical axis (ratio[R]) is the quotient of the red grating line-filled area (S_{ar}) and the green rectangle area (S_{si}) depicted in Figures 4.5 and 4.6 (i.e., the ratio[R] = $S_{\text{ar}}/S_{\text{si}}$). Here, a lower ratio[R] means a greater improvement of the AR characteristics. If its value is 0, there is no reflectance. Furthermore, when the ratio is 1, the power reflectance of the structured surface is the same as that of a bare Si substrate. In the same figure, the horizontal axis ($\Sigma[n'/n]$) indicates the summary of the refractive index change in each minute-divided part of h , which can be obtained in reference to the plotted (unnormalized) refractive index distribution. This means that the total refractive index changes along with the taper height. The black line showed an overall fitting for all the samples. The ratio[R] increased with $\Sigma[n'/n]$, demonstrating that a rougher change of n_{eff} distribution would be corresponded by a greater increase in the total power reflectance. For the single-line scanned tapers (blue, empty circles), the ratio[R] increased inversely proportionally with respect to the aspect ratio, indicating that a higher aspect ratio will reduce the reflectance further. The fitting line for set B (red dashed line) samples laid above the fitting line of sets A (black dashed line) and C (green dashed line), indicating that the tapers fabricated with the size of set B had a relatively smaller improvement in the AR characteristics because of the relatively lower average aspect ratio of set A (1.23), compared with those of sets B (1.46) and C (1.43). However, for each profile-controlled set (A, B, and C) of the samples, the power reflectance of AR tapers depended greatly on their profiles, whereas the aspect ratio was maintained. Additionally, for all sets, the S-profiled tapers demonstrated a relatively lower ratio[R] and thus assumed a n_{eff} distribution similar to the Klopfenstein taper [54,67], which is characterized by a smoothly changing n_{eff} , as well as a stable

reflectance distribution, at the top and bottom of the taper. Thus, compared with the T and TS profiles, the P and S profiles should have stronger mechanical strength sufficient to increase the mechanical stability of moth-eye structures.

4.4 Conclusion

The AR characteristic of 1-D moth-eye structures has been successfully controlled by adjusting the n_{eff} distribution of micro tapers for THz waves, which is achieved by employing femtosecond laser processing. A good agreement was found between the measured results from THz-TDS and the simulated results by FDTD, indicating that aside from the aspect ratio of micro-tapers, the profile is another key parameter that influences the power reflectance distribution. The most stable reflectance distribution was observed in the S-profiled structures, maintained at nearly 0 in the 0.5–1.0 THz range. The S-profiled tapers also displayed lower total power reflectance for a broadband THz region from 0.1 to 1.0 THz, covering several high-frequency bands that could be used for 6G communication. To specify the range more accurately, a more precise processing technology using the femtosecond laser may be necessary; this could be achieved by applying a laser with a shorter wavelength and a lens with a smaller focused spot size. Furthermore, combining the method herein with other surface modification technologies, such as etching and coating technologies, may provide more possibilities for the anti-reflection design of moth-eye structures in the THz region. As the output of the femtosecond laser constantly increases in recent years, this adds up to improvements in its processing efficiency and processing technologies. The findings presented herein can contribute to both the development of THz applications and laser processing technologies.

Chapter 5

Polymer-coated moth-eye hybrid ARS

5.1 Introduction

Although the fabrication of moth-eye structures for THz waves is free of technical barriers, the applications of moth-eye structures for daily life are still limited by their weak mechanical stability [51,58]. Profiling the microtapers of moth-eye structures may increase the mechanical stability [59–61]; however, as the resulting microstructures are brittle, the AR structure (ARS) is difficult to clean [62]. On the contrary, an AR coating with a flat surface can prevent dust from depositing inside the structures and has sufficient mechanical stability to endure the necessary cleaning process. In addition, multilayer coatings also possess broadband AR features. Hosako fabricated a four-layer coating based on SiO_x via plasma-enhanced chemical vapor deposition for enhancing the transmittance of Ge substrate for THz waves in the wavenumber range of $40\text{--}130\text{ cm}^{-1}$ [38]. However, the complicated fabrication process and time cost limit the application of this technique in the THz region as the AR coating is much thicker in the THz region than in the visible region. Kawada et al. developed a two-layer coating based on a refractive index-controllable composite, through which the amplitude of $0.7\text{--}1.5\text{-THz}$ transmitted waves exceeded 90% [62,133]. This composite was fabricated by dispersing Si nanoparticles (NPs) in a cyclo-olefin polymer. A refractive index of $1.52\text{--}2.0$ can be achieved in these composites by adjusting the Si NP ratio during fabrication. However, the amplitude transmittance reduces to 85% (corresponding to a power reflectance of 68%) in the $1.1\text{--}2.0\text{-THz}$ range.

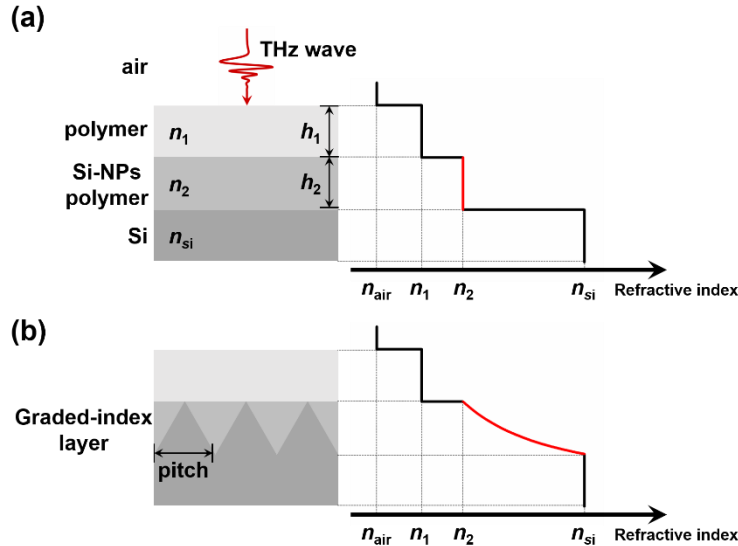


Figure 5.1. Profiles of (a) a two-layer AR coating, (b) the hybrid ARS, and their refractive index distribution.

For suppressing this transmittance fluctuating and further improving the AR characteristics, we proposed a simpler structure obliterating the mismatch of refractive index smoothly instead of increasing the coating layer. As showing in Figure 5.1 (a), there is a clifflike change of refractive index (red line in the refractive index distribution)

from the second layer to the Si substrate. By inserting a moth-eye structure into the second layer (Figure 5.1 (b)), the graded-index feature was added to this combined layer, which has a smoother change of effective refractive index connected to Si substrate (from n_2 to n_{si}). From the view of antireflection, the first layer of this hybrid ARS works as a quarter wavelength ($\lambda/4$) coating, in which the positive interference improves the transmittance of the incident THz waves, and the combined second layer is a sub-wavelength structure that can enhance the 0-order diffraction and improve the transmittance for tunable THz range with a selected size of structure [10].

We simulated the antireflective properties of this hybrid ARS by employing the method of Finite-difference time-domain (FDTD). Basing on the simulated results, we fabricated a hybrid ARS by employing the femtosecond laser processing for ablating the moth-eye structure and the heat press coating method for attaching the coating layers. The hybrid ARS was measured by a terahertz time-domain spectroscopy (THz-TDS) for calculating the power reflectance of the AR surface. The simulated and measured results agree well and showed that the power reflectance was remained less than 6% from 0.6 THz to 2.5 THz. From 0.1 to 2.5 THz, the total reflectance (integrated area under the power reflectance versus frequency plot [59]) was reduced to 20% that of the bare Si surface. The hybrid ARS also inherited the cleanable flat surface from the coating structure, which can also work as a protective shield for the moth-eye structures.

5.2 Experiment and results

Table 5.1. Ideal thicknesses of the $\lambda/4$ coating for different center frequencies and refractive indices (unit: μm)

$n_1 \backslash f$ (THz)	0.1	0.7	1.3	1.9	2.5
1.52	493	70	38	26	20
1.60	468	67	36	25	19
1.70	441	63	34	23	18
1.80	416	59	32	22	17
1.90	394	56	30	21	16
2.0	375	54	29	20	15

According to Kawada [62], the refractive indices should satisfy $1.52 < n_1 < n_2 < 2$. In $\lambda/4$ coating theory, $n_2 = n_1^2$; thus, $n_1 = 1.52$ and $n_2 = 2$ should be the best choices for the refractive indices. In addition, the thickness of the first layer should be one-quarter of the incident wavelength. Table 1 shows the ideal thicknesses of a $\lambda/4$ coating with different center frequencies (0.1–2.5 THz, quarterly divided) and refractive indices (1.52–2.0). The thickness was calculated as $c/(4nf)$, where c is the speed of light, n is the refractive index of the coating material, and f is the center frequency. If the center frequency is located at the edge (i.e., at 0.1 or 2.5 THz), half of the AR band will be out of the target range. At center frequencies of 0.7 and 1.9 THz (1/4 and 3/4 of the 0.1–2.5-THz range, respectively), the $\lambda/4$ coating should be $<70\text{-}\mu\text{m}$ thick and $>20\text{-}\mu\text{m}$ thick, respectively, if the refractive index changes from 1.52 to 2.0. Consequently, the simulations were performed under the following conditions: $n_1 \in [1.52, 1.60, 1.70, 1.80, 1.90, 2.0]$, $n_2 \in [1.52, 1.60, 1.70, 1.80, 1.90, 2.0]$, and first-layer thickness $h_1 \in [7.5, 20.0, 32.5, 45.0, 57.5, 70.0] \mu\text{m}$. The Si substrate was simulated with $n_{\text{si}} = 3.407$ (measured via THz-TDS) and thickness = $795 \mu\text{m}$ (moth-eye parts included). The tapers of the moth-eye structure were given a triangular profile resembling laser-fabricated

moth-eye structures. The taper pitch was set to 35 μm (corresponding to a cutoff frequency of 2.5 THz), and the taper aspect ratio was 1.0 (i.e., the depth was also 35 μm) for convenience in the actual fabrication process. The moth-eye structures were buried in a material with a refractive index of n_2 .

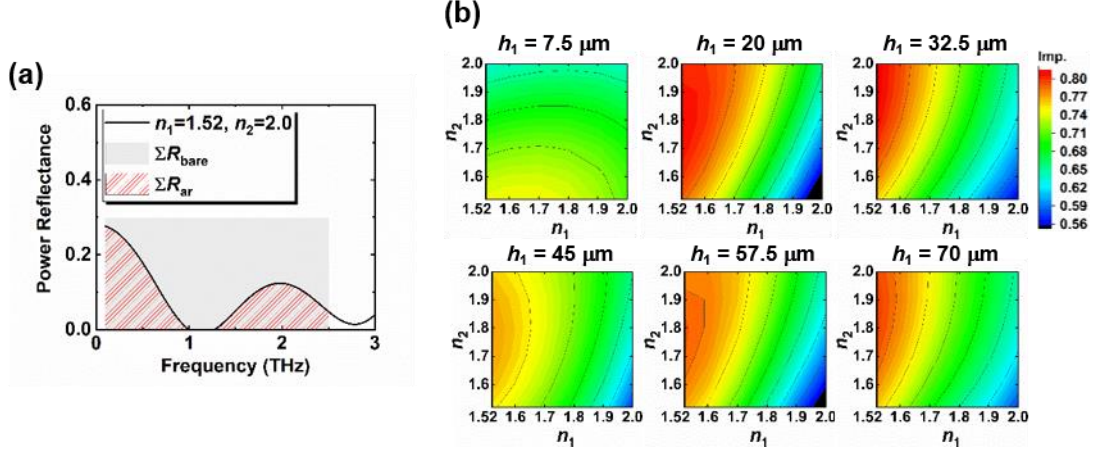


Figure 5.2. Simulation results: (a) power reflectance of a two-layer coating on a Si substrate with $n_1=1.52$, $n_2=2$, $h_1=21$ μm , $h_2=24$ μm , and thickness=795 μm and (b) improvement index mapping of hybrid ARS with different h_1 , which is plotted as a function of refractive indices n_1 and n_2 .

Figure 5.2 (a) plots the power reflectance of a two-layer coating on the Si substrate as a function of frequency. The simulated result agrees with the measured and simulated results of Kawada *et al*[62]. The red-striped and gray-solid areas indicate the total reflectances of the ARSs (ΣR_{ar}) and a bare Si surface (ΣR_{bare}), respectively, over the 0.1–2.5-THz range. Using these simulated areas, the improvement index was calculated as $I_{\text{imp}}=1-\Sigma R_{\text{ar}}/\Sigma R_{\text{bare}}$. The total reflectance of this two-layer coating was 33% of the bare Si, indicating that the AR characteristic outperformed that of the Si surface by 67%. Figure 5.2 (b) shows the I_{imp} mappings derived from the simulated power reflectances. When the first layer was thin ($h_1=7.5$ μm), I_{imp} depended more on n_2 than on n_1 because 7.5- μm thickness corresponds to the center wavelength of 6.6 THz on the $\lambda/4$ coating. At this thickness ($h_1=7.5$ μm), the sample with $n_1=1.6$ and $n_2=1.52$ showed the highest improvement (75%). As the thickness of the first layer (h_1) was increased to ≥ 20 μm , the first layer began working as a $\lambda/4$ coating with a center wavelength located within the 0.1–2.5-THz range and the I_{imp} depended more on n_1 than on n_2 because the coupled range of THz waves depends on the refractive index of a $\lambda/4$ coating. However, the best improvements of the samples with $h_1 \geq 20$ μm were very similar and close to 80%. Changing the thickness might shift the center AR frequency of the quarter-wavelength coating but has little effect on the total reflectance in a limited THz range. The sample with $n_1=1.52$, $n_2=1.9$, and $h_1=32.5$ μm showed the highest improvement (82%) among the simulated samples. Most of the hybrid ARSs showed an I_{imp} that exceeded 60%, and the I_{imp} of samples with $n_1 \leq n_2$ is higher than that of the two-layer coating (67%).

A hybrid ARS with $n_1=1.52$, $n_2=2.0$, and $h_1=20$ μm was fabricated, whose predicted improvement index (80%) was only 2% less than the best simulation result. Firstly, we fabricated a one-dimensional moth-eye structure (with periodically arranged grooves) on the Si substrate with a pitch of 35 μm and an aspect ratio of 1 via femtosecond laser processing (Figure 5.3 (a)) [54,59], subsequently, attached a polymer-based two-layer coating onto the moth-eye structure by heat press coating method under 170°C for 5

min. This two-layer coating is prepared in advance, and the refractive index was controlled to 1.52 and 2 for the first and second layer, respectively, by adjusting the Si NPs fraction ratio during the fabrication (0 and 35% for the first and second layer, respectively)[62,133]. As showing in Figure 5.3 (c), the intervals between protuberances were well filled by Si NPs-dispersed polymer, although small holes with a size of several micrometers were encapsulated in the bottom of the moth-eye structure. For the sample of AR coating (Figure 5.3 (b)), a 6- μm thick polymer layer (refractive index, 1.52) was added between the NPs-dispersed polymer layer and Si substrate to increase the adhesiveness, which forming a three-layer coating different from the simulated two-layer AR coating.

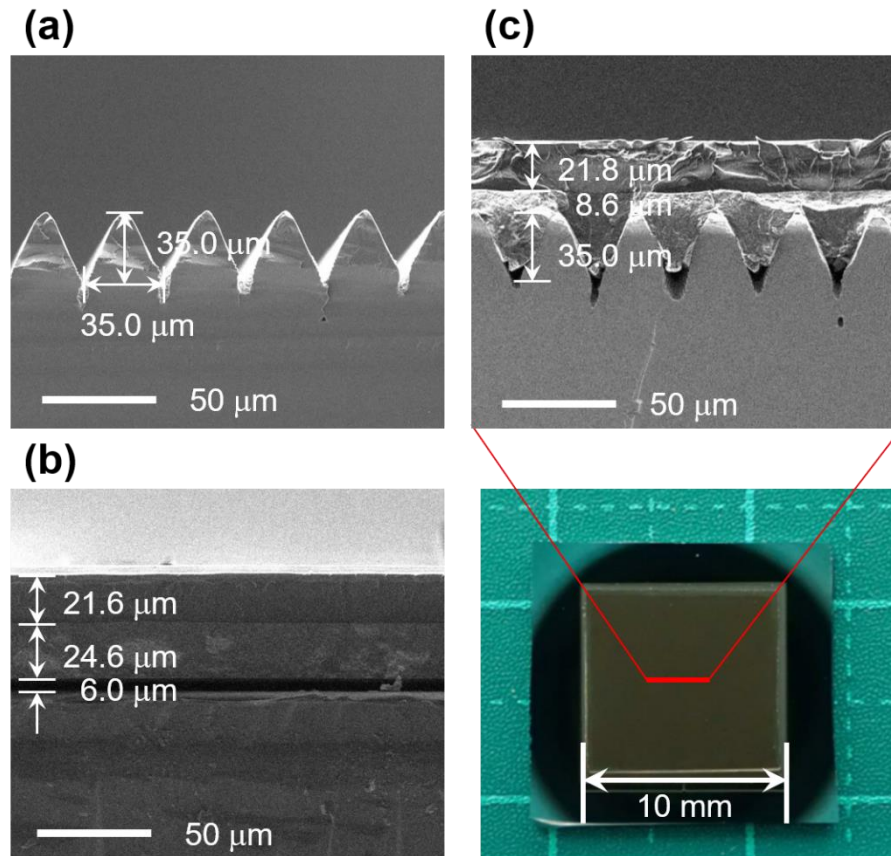


Figure 5.3. Profiles of (a) the moth-eye structure, (b) the three-layer AR coating, and (c) the hybrid ARS. The bottom right panel is an image of an actual sample sized 10 mm \times 10 mm. Both samples were fabricated on a single side of the Si substrate.

The spectrum intensities of these three samples were obtained via fast Fourier transform of the time waveforms measured using the THz-TDS system, in which the THz waves were propagating to the samples at a normal incidence with the electric field perpendicular to the parallelly arranged grooves[54,59]. By comparing the spectral intensities of the transmitted signals and Si substrate, the power reflectance was calculated considering the transmittances and reflectances of both the ARS and reverse bare sides [48,49,54,59]. The measured power reflectances of these samples are shown in Figure 5.4 (a)–(c) (black squares). The error bars are the standard deviations of obtained from 100 measurements. The insets display the measured spectrum intensities of the respective samples. Based on the profiles in Figure 5.3, the power reflectances were simulated using the FDTD method (red curves in Figure 5.4 (a)–(c)). The power reflectances of the laser-ablated samples, moth-eye structure, and hybrid ARS were partly negative. During the laser processing, silicon oxide may form under the extreme

condition of high-temperature, high-pressure in the laser ablation center. The refractive index of silicon oxide is much lower than that of Si, implying a higher power transmittance in the calculation; the decreased refractive index possibly contributed to the negative values in the power reflectance spectra[59]. On the contrary, the measurement results of the coated samples showed almost perfect agreement with the simulated results, in which the samples were not processed under laser irradiation. Both the measured and simulated samples exhibited broadband AR characteristics. The hybrid ARS exhibited a super-broad AR band in the range of $\sim 0.6\text{--}2.5$ THz, with a power reflectance of $<6\%$. As shown in Figure 5.4 (d), the hybrid ARS best improved the AR characteristics (by 80%; much higher than the improvements of the moth-eye structure or the three-layer coating).

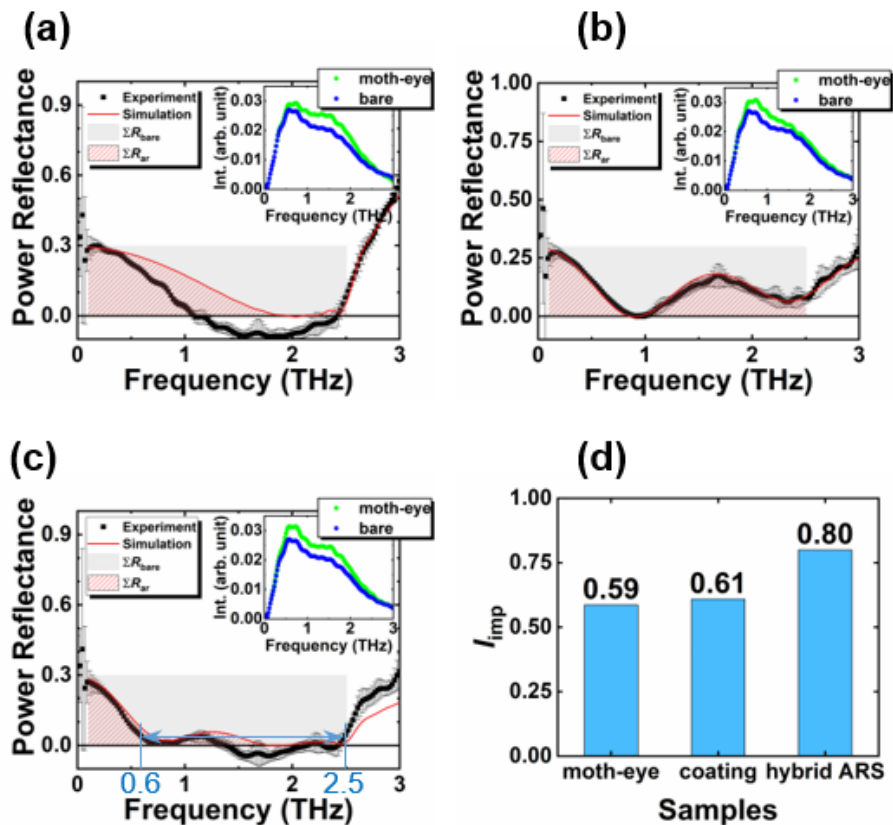


Figure 5.4. Measured and simulated power reflectances of (a) the moth-eye structure, (b) the three-layer coating, and (c) the hybrid ARS. Panel (d) compares the improvement indices of the three samples calculated from their simulated power reflectances. The insets in panels (a)–(c) display the spectrum intensities measured via THz-TDS. The green and blue dots were taken from the ARSs and the bare Si surface, respectively.

5.3 Conclusion

In conclusion, we designed a hybrid ARS comprising an AR coating covered with moth-eye structures and simulated its power reflectance. The AR characteristic was improved by 80% compared to that of the bare Si substrate. We also demonstrated that the proposed structure can be fabricated using a mixed fabrication method (femtosecond laser processing and the heat press coating method). The measured power reflectance of the hybrid ARS showed good agreement with the simulated results. The hybrid exhibited a super-broad AR band over the $\sim 0.6\text{--}2.5$ -THz range, in which the power reflectance was $<6\%$. Total power reflectance over the $0.1\text{--}2.5$ -THz range was improved by 80% compared to that of the bare Si surface, which is

much higher than the improvements observed in the moth-eye structure (59%) and the three-layer AR coating (60%). The hybrid ARS not only achieved excellent AR characteristics but also inherited the cleanable flat surface of the coating, which can protect the moth-eye structure from physical damages. This high-performance, strong ARS with a flat surface is expected to enhance the transmittance of THz waves in numerous THz components, especially of lens and generators. This hybrid-ARS THz technology can also potentially contribute to the next generation (6G) of mobile communication with frequency bands 0.275–0.45 THz[127]. In this band, the hybrid ARS showed approximately 15%-20% power reflectance, which is almost half of the bare Si surface. Moreover, the AR performance can be further improved by adjusting the design of the moth-eye profile and AR coating.

Chapter 6

Conclusion and future perspectives

6.1 Conclusion

Systemic research for the moth-eye structures in THz frequencies, mainly from 0.1 to 2.5 THz, was performed for pursuing a high AR performance and high mechanical stability to meet the actual applications. Fabrication method basing on femtosecond laser processing was established, and the laser fabricated moth-eye structures has made considerable improvement in the transmittance of a THz generator, which had a 2.5-4.4 times improvement of the output at the theoretical and experimental output frequencies comparing to that of the one without moth-eye structure. A reasonable solution for the improvement of the transmittance of laser irradiated ZnO substrate has been proposed basing on the study of laser-matter reaction for ZnO, which is demonstrated as a material for THz generator and potentially functional material for other THz applications. To suppress the fluctuating power reflectance distribution and improve the mechanical stability, profile control of micro tapers in moth-eye structure was accomplished and an important parameter related to the AR performance was proposed for its AR design. Lastly, a polymer-coated moth-eye structure was demonstrated to realized a high AR performance for a broadband THz region and high mechanical stability for actual applications. This hybrid structure can. The total power reflectance from 0.1 to 2.5 THz was reduced to 20% of the unprocessed Si surface (30% of the incidence power), which means the total reflected power is less than 6% for this broadband. This work can not only promote the practical application of THz but also contribute to ultrafast laser-based precision processing technology.

6.2 Future perspectives

Impressive improvement of AR performance has been achieved in works so far. Likewise, basing on the above-introduced results, there are some important works for this research that can be opened up for achieving better AR performance and promoting the application of THz waves in the future.

Better AR performance

Basing on the results of chapter 4 (Figure 4.9), more mathematical (topological) work on the design of profile can be done for achieving better AR performance. i.e. what is the best profile for such moth-eye structures? For the hybrid structures proposed in chapter 5, design of the AR coating parts can also future improve the AR performance.

Stronger mechanical stability

The flat surface of the hybrid AR structure demonstrated in chapter 5 can work as a protecting cushion and reduce the shock for the microtapers. In addition, the mechanical stability can be improved by reinforcing the structure itself. Branches with random directions in the bottom of the microtapers can be observed in the Si and GaAs moth-eye structures, and these branches are possible to make such tiny structures break easily. During the laser ablation, skipped debris is randomly deposited on the entrance and

groove to forming the melts. These melts will bend the propagating direction of the laser beam inside the groove and promoting the formation of these branches[103]. Further works on suppressing the formation of the melts can be achieved by adjusting the strategies on laser processing, for example, increasing the cooling time by reducing the repetition rate or changing the scan pattern.

Incident angle characteristics

Most moth-eye structures in this research were fabricated in one-dimensional for the linearly polarized THz sources, which is enough for lots of scientific research. For more practicality in daily life, moth-eye structures for unpolarized THz sources with broad incident angles need to be achieved. 2-dimensional structure as described in chapter 3 for the THz generator should be a preliminary resolution and further research on the profile need to be done for achieving such broad incident angle properties.

Application to 6G mobile communication

Such moth-eye structures can be used for lots of THz applications related to imaging, spectroscopy, and communication. Especially for the next mobile communications, frequency bands within 275–450 GHz have been specified for THz communication in land mobile service applications during the World Radiocommunication Conference 2019. The high frequencies offer an opportunity to satisfy the Tbps data rate demand of the next generation of the mobile communication system, but there remain challenges such as path loss, atmospheric absorption, as well as reflection loss, which should be overcome. Our fabricated structures have a considerable AR performance for this band. For example, the hybrid AR structure showed a 15%-20% power reflectance for frequencies from approximately 0.45 to 0.25 THz, which is 30% for a bare surface in the case of Si. To make this hybrid structure match the 6G band better, adjusting of taper profile, aspect ratio, or thickness of the first coating layer needs to be performed to obtain a matched refractive index distribution.

Reference

- [1] Zhang XC, Xu J. Introduction to THz wave photonics. Boston, MA: Springer US; 2010. <https://doi.org/10.1007/978-1-4419-0978-7>.
- [2] Tonouchi M. Cutting-edge terahertz technology. *Nat Photonics* 2007;1:97–105. <https://doi.org/10.1038/nphoton.2007.3>.
- [3] Ferguson B, Zhang X. Materials for terahertz science and technology. *Nat Mater* 2002;1:26–33. <https://doi.org/10.1038/nmat708>.
- [4] Sakai K, editor. Terahertz Optoelectronics. vol. 97. Berlin, Heidelberg: Springer Berlin Heidelberg; 2005. <https://doi.org/10.1007/b80319>.
- [5] Smith PR, Auston DH, Nuss MC. Subpicosecond photoconducting dipole antennas. *IEEE J Quantum Electron* 1988;24:255–60. <https://doi.org/10.1109/3.121>.
- [6] Wang H, Horikawa Y, Tsuchikawa S, Inagaki T. Terahertz time-domain spectroscopy as a novel tool for crystallographic analysis in cellulose. *Cellulose* 2020;27:9767–77. <https://doi.org/10.1007/s10570-020-03508-9>.
- [7] Wang H, Inagaki T, Hartley ID, Tsuchikawa S, Reid M. Determination of Dielectric Function of Water in THz Region in Wood Cell Wall Result in an Accurate Prediction of Moisture Content. *J Infrared, Millimeter, Terahertz Waves* 2019;40:673–87. <https://doi.org/10.1007/s10762-019-00594-0>.
- [8] Inagaki T, Ahmed B, Hartley ID, Tsuchikawa S, Reid M. Simultaneous prediction of density and moisture content of wood by terahertz time domain spectroscopy. *J Infrared, Millimeter, Terahertz Waves* 2014;35:949–61. <https://doi.org/10.1007/s10762-014-0095-7>.
- [9] Wang H, Tsuchikawa S, Inagaki T. Terahertz time-domain spectroscopy as a novel tool for crystallographic analysis in cellulose: the potentiality of being a new standard for evaluating crystallinity. *Cellulose* 2021;28:5293–304. <https://doi.org/10.1007/s10570-021-03902-x>.
- [10] Kemp MC, Taday PF, Cole BE, Cluff JA, Fitzgerald AJ, Kemp MC, et al. Security applications of terahertz technology, n.d. <https://doi.org/https://doi.org/10.1117/12.500491>.
- [11] Wang J, Sun Q, Stantchev RI, Chiu T-W, Ahuja AT, Pickwell-MacPherson E. In vivo terahertz imaging to evaluate scar treatment strategies: silicone gel sheeting. *Biomed Opt Express* 2019;10:3584. <https://doi.org/10.1364/boe.10.003584>.
- [12] Sterczewski LA, Westberg J, Yang Y, Burghoff D, Reno J, Hu Q, et al. Terahertz hyperspectral imaging with dual chip-scale combs. *Optica* 2019;6:766. <https://doi.org/10.1364/optica.6.000766>.
- [13] Zhong S. Progress in terahertz nondestructive testing: A review. *Front Mech Eng* 2019;14:273–81. <https://doi.org/10.1007/s11465-018-0495-9>.
- [14] Jansen C, Wietzke S, Peters O, Scheller M, Vieweg N, Salhi M, et al. Terahertz imaging: Applications and perspectives. *Appl Opt* 2010;49. <https://doi.org/10.1364/AO.49.000E48>.
- [15] Stantchev RI, Yu X, Blu T, Pickwell-MacPherson E. Real-time terahertz imaging with a single-pixel detector. *Nat Commun* 2020;11:1–8. <https://doi.org/10.1038/s41467-020-16370-x>.
- [16] Stoik C, Bohn M, Blackshire J. Nondestructive evaluation of aircraft composites using reflective terahertz time domain spectroscopy. *NDT E Int* 2010;43:106–15. <https://doi.org/10.1016/j.ndteint.2009.09.005>.
- [17] Heinz E, May T, Born D, Zieger G, Anders S, Zakosarenko V, et al. Passive 350 GHz Video Imaging Systems for Security Applications. *J Infrared, Millimeter, Terahertz Waves* 2015;36:879–95. <https://doi.org/10.1007/s10762-015-0170-8>.
- [18] Hu BB, Nuss MC. Imaging with terahertz waves. *Opt Lett* 1995;20:1716. <https://doi.org/10.1364/OL.20.001716>.

- [19] Nagatsuma T, Horiguchi S, Minamikata Y, Yoshimizu Y, Hisatake S, Kuwano S, et al. Terahertz wireless communications based on photonics technologies. *Opt Express* 2013;21:23736. <https://doi.org/10.1364/OE.21.023736>.
- [20] Kleine-ostmann T, Nagatsuma T. A Review on Terahertz Communications Research 2011:143–71. <https://doi.org/10.1007/s10762-010-9758-1>.
- [21] ZHAO Y, YU G, XU H. 6G mobile communication networks: vision, challenges, and key technologies. *Sci Sin Informationis* 2019;49:963–87. <https://doi.org/10.1360/n112019-00033>.
- [22] Yang Y, Yamagami Y, Yu X, Pitchappa P, Webber J, Zhang B, et al. Terahertz topological photonics for on-chip communication. *Nat Photonics* 2020;14:446–51. <https://doi.org/10.1038/s41566-020-0618-9>.
- [23] Nagatsuma T, Ducournau G, Renaud CC. Advances in terahertz communications accelerated by photonics. *Nat Photonics* 2016;10:371–9. <https://doi.org/10.1038/nphoton.2016.65>.
- [24] Walker CK. *Terahertz Astronomy*. CRC Press; 2015. <https://doi.org/10.1201/b19111>.
- [25] Lewis RA. A review of terahertz sources. *J Phys D Appl Phys* 2014;47:374001. <https://doi.org/10.1088/0022-3727/47/37/374001>.
- [26] Isgandarov E, Ropagnol X, Singh M, Ozaki T. Intense terahertz generation from photoconductive antennas. *Front Optoelectron* 2021;14:64–93. <https://doi.org/10.1007/s12200-020-1081-4>.
- [27] Zhang Y, Li K, Zhao H. Intense terahertz radiation: generation and application. *Front Optoelectron* 2021;14:4–36. <https://doi.org/10.1007/s12200-020-1052-9>.
- [28] Wietzke S, Jansen C, Reuter M, Jung T, Kraft D, Chatterjee S, et al. Terahertz spectroscopy on polymers: A review of morphological studies. *J Mol Struct* 2011;1006:41–51. <https://doi.org/10.1016/j.molstruc.2011.07.036>.
- [29] Grischkowsky D, Keiding S, van Exter M, Fattinger C. Far-infrared time-domain spectroscopy with terahertz beams of dielectrics and semiconductors. *J Opt Soc Am B* 1990;7:2006. <https://doi.org/10.1364/JOSAB.7.002006>.
- [30] Yasuda H, Hosako I. Measurement of Terahertz Refractive Index of Metal with Terahertz Time-Domain Spectroscopy. *Jpn J Appl Phys* 2008;47:1632–4. <https://doi.org/10.1143/JJAP.47.1632>.
- [31] Dorney TD, Baraniuk RG, Mittleman DM. Material parameter estimation with terahertz time-domain spectroscopy. *J Opt Soc Am A* 2001;18:1562. <https://doi.org/10.1364/JOSAA.18.001562>.
- [32] Dai J, Zhang J, Zhang W, Grischkowsky D. Terahertz time-domain spectroscopy characterization of the far-infrared absorption and index of refraction of high-resistivity, float-zone silicon. *J Opt Soc Am B* 2004;21:1379. <https://doi.org/10.1364/josab.21.001379>.
- [33] Davies CL, Patel JB, Xia CQ, Herz LM, Johnston MB. Temperature-Dependent Refractive Index of Quartz at Terahertz Frequencies. *J Infrared, Millimeter, Terahertz Waves* 2018;39:1236–48. <https://doi.org/10.1007/s10762-018-0538-7>.
- [34] Rayleigh, Lord. On Reflection of Vibrations at the Confines of two Media between which the Transition is Gradual. *Proc London Math Soc* 1879;s1-11:51–6. <https://doi.org/10.1112/plms/s1-11.1.51>.
- [35] Lee C. *The Current Trends of Optics and Photonics*. vol. 129. Dordrecht: Springer Netherlands; 2015. <https://doi.org/10.1007/978-94-017-9392-6>.
- [36] Englert CR, Birk M, Maurer H. Antireflection coated, wedged, single-crystal silicon aircraft window for the far-infrared. *IEEE Trans Geosci Remote Sens* 1999;37:1997–2003. <https://doi.org/10.1109/36.774710>.
- [37] Hosako I. Antireflection coating formed by plasma-enhanced chemical-vapor deposition for terahertz-frequency germanium optics. *Appl Opt* 2003;42:4045. <https://doi.org/10.1364/ao.42.004045>.
- [38] Hosako I. Multilayer optical thin films for use at terahertz frequencies: Method of fabrication. *Appl Opt* 2005;44:3769–73. <https://doi.org/10.1364/AO.44.003769>.
- [39] Chen YW, Zhang XC. Anti-reflection implementations for terahertz waves. *Front*

- Optoelectron 2014;7:243–62. <https://doi.org/10.1007/s12200-013-0377-z>.
- [40] Raut HK, Ganesh VA, Nair AS, Ramakrishna S. Anti-reflective coatings: A critical, in-depth review. *Energy Environ Sci* 2011;4:3779–804. <https://doi.org/10.1039/c1ee01297e>.
- [41] CLAPHAM PB, HUTLEY MC. Reduction of Lens Reflexion by the “Moth Eye” Principle. *Nature* 1973;244:281–2. <https://doi.org/10.1038/244281a0>.
- [42] Wilson SJJ, Hutley MCC. The Optical Properties of ‘Moth Eye’ Antireflection Surfaces. *Opt Acta Int J Opt* 1982;29:993–1009. <https://doi.org/10.1080/713820946>.
- [43] Brückner C, Pradarutti B, Riehemann S, Stenzel O, Steinkopf R, Gebhardt A, et al. Moth-eye structures for reduction of Fresnel losses at THz components. In: Jäger D, Stöhr A, editors. *Millimeter-Wave and Terahertz Photonics*, vol. 6194, 2006, p. 61940N. <https://doi.org/10.1117/12.662199>.
- [44] Brückner C, Pradarutti B, Stenzel O, Steinkopf R, Riehemann S, Notni G, et al. Broadband antireflective surface-relief structure for THz optics. *Opt Express* 2007;15:779. <https://doi.org/10.1364/OE.15.000779>.
- [45] Kuroo S, Shiraishi K, Sasho H, Yoda H, Muro K. Triangular surface-relief grating for reduction of reflection from silicon surface in the 0.1-3 terahertz region. 2008 Conf. Lasers Electro-Optics, IEEE; 2008, p. 1–2. <https://doi.org/10.1109/CLEO.2008.4551371>.
- [46] Wagner-Gentner A, Graf UU, Rabanus D, Jacobs K. Low loss THz window. *Infrared Phys Technol* 2006;48:249–53. <https://doi.org/10.1016/j.infrared.2006.01.004>.
- [47] Brückner C, Käsebier T, Pradarutti B, Riehemann S, Notni G, Kley E, et al. Broadband antireflective structures applied to high resistive float zone silicon in the THz spectral range. *Opt Express* 2009;17:3063. <https://doi.org/10.1364/OE.17.003063>.
- [48] Han P, Chen YW, Zhang XC. Application of silicon micropyramid structures for antireflection of terahertz waves. *IEEE J Sel Top Quantum Electron* 2010;16:338–43. <https://doi.org/10.1109/JSTQE.2009.2031164>.
- [49] Chen YW, Han PY, Zhang XC. Tunable broadband antireflection structures for silicon at terahertz frequency. *Appl Phys Lett* 2009;94:3–5. <https://doi.org/10.1063/1.3075059>.
- [50] Kuroo SI, Oyama S, Shiraishi K, Sasho H, Fukushima K. Reduction of light reflection at silicon-plate surfaces by means of subwavelength gratings in terahertz region. *Appl Opt* 2010;49:2806–12. <https://doi.org/10.1364/AO.49.002806>.
- [51] Brahm A, Döring S, Wilms A, Notni G, Nolte S, Tünnermann A. Laser-generated broadband antireflection structures for freeform silicon lenses at terahertz frequencies. *Appl Opt* 2014;53:2886. <https://doi.org/10.1364/AO.53.002886>.
- [52] Matsumura T, Young K, Wen Q, Hanany S, Ishino H, Inoue Y, et al. Millimeter-wave broadband antireflection coatings using laser ablation of subwavelength structures. *Appl Opt* 2016;55:3502. <https://doi.org/10.1364/ao.55.003502>.
- [53] Sakurai H, Nemoto N, Konishi K, Takaku R, Sakurai Y, Katayama N, et al. Terahertz broadband anti-reflection moth-eye structures fabricated by femtosecond laser processing. *OSA Contin* 2019;2:2764. <https://doi.org/10.1364/osac.2.002764>.
- [54] Yu X, Ohta M, Takizawa N, Mikame K, Ono S, Bae J. Femtosecond-laser-fabricated periodic tapered structures on a silicon substrate for terahertz antireflection. *Appl Opt* 2019;58:9595. <https://doi.org/10.1364/AO.58.009595>.
- [55] Takaku R, Hanany S, Imada H, Ishino H, Katayama N, Komatsu K, et al. Broadband, millimeter-wave anti-reflective structures on sapphire ablated with femto-second laser. *J Appl Phys* 2020;128:225302. <https://doi.org/10.1063/5.0022765>.
- [56] Wang D, Li Y, Zhang C, Liao W, Li Z, Zhang Q, et al. Broadband terahertz antireflective microstructures on quartz crystal surface by CO₂ laser micro-processing. *Opt Express* 2019;27:18351. <https://doi.org/10.1364/oe.27.018351>.
- [57] Yu X, Ono S, Bae J. Application of laser generated moth-eye structure for a periodic terahertz-wave generator. 2019 44th Int. Conf. Infrared, Millimeter, Terahertz Waves, vol. 2019- Septe, IEEE; 2019, p. 1–2. <https://doi.org/10.1109/IRMMW-THz.2019.8874269>.
- [58] Yoo YJ, Kim YJ, Kim S-Y, Lee JWJHW, Kim K, Ko JH, et al. Mechanically robust

- antireflective moth-eye structures with a tailored coating of dielectric materials. *Opt Mater Express* 2019;9:4178. <https://doi.org/10.1364/ome.9.004178>.
- [59] Yu X, Yasunaga Y, Goto K, Liu D, Ono S. Profile control of femtosecond laser-fabricated moth-eye structures on Si substrate. *Opt Lasers Eng* 2021;142:106584. <https://doi.org/10.1016/j.optlaseng.2021.106584>.
- [60] Yu X, Horita N, Bessho M, Sudo M, Ono S, Bae J. Shape dependence of Terahertz anti-reflective structures fabricated by femtosecond laser processing. In: Klotzbach U, Kling R, Watanabe A, editors. *Laser-based Micro- Nanoprocessing XIII*, SPIE; 2019, p. 55. <https://doi.org/10.1117/12.2507534>.
- [61] Yu X, Bae J, Ono S. Profile control of one-dimensional Terahertz moth-eye structure fabricated by femtosecond laser processing. 2019 44th Int. Conf. Infrared, Millimeter, Terahertz Waves, vol. 2019- Septe, IEEE; 2019, p. 1–2. <https://doi.org/10.1109/IRMMW-THz.2019.8874287>.
- [62] Kawada Y, Soeda J, Satozono H, Ikeda Y, Takahashi H. High-transparency polymer-silicon nano-particle composites for broadband anti-reflection of terahertz waves. *Appl Phys Express* 2019;12:92004. <https://doi.org/10.7567/1882-0786/ab3470>.
- [63] Southwell WH. Gradient-index antireflection coatings. *Opt Lett* 1983;8:584. <https://doi.org/10.1364/ol.8.000584>.
- [64] Yeh P, Sari S. Optical properties of stratified media with exponentially graded refractive index. *Appl Opt* 1983;22:4142. <https://doi.org/10.1364/ao.22.004142>.
- [65] Grann EB, Moharam MG, Pommet DA. Optimal design for antireflective tapered two-dimensional subwavelength grating structures. *J Opt Soc Am A* 1995;12:333. <https://doi.org/10.1364/josaa.12.000333>.
- [66] Chen M, Chang HC, Chang ASP, Lin SY, Xi JQ, Schubert EF. Design of optical path for wide-angle gradient-index antireflection coatings. *Appl Opt* 2007;46:6533–8. <https://doi.org/10.1364/AO.46.006533>.
- [67] Klopfenstein RW. A Transmission Line Taper of Improved Design. *Proc IRE* 1956;44:31–5. <https://doi.org/10.1109/JRPROC.1956.274847>.
- [68] Bizi-Bandoki P, Benayoun S, Valette S, Beaugiraud B, Audouard E. Modifications of roughness and wettability properties of metals induced by femtosecond laser treatment. *Appl Surf Sci* 2011;257:5213–8. <https://doi.org/10.1016/j.apsusc.2010.12.089>.
- [69] Liu B, Jiang G, Wang W, Mei X, Wang K, Cui J, et al. Porous microstructures induced by picosecond laser scanning irradiation on stainless steel surface. *Opt Lasers Eng* 2016;78:55–63. <https://doi.org/10.1016/j.optlaseng.2015.10.003>.
- [70] Förster DJ, Weber R, Holder D, Graf T. Estimation of the depth limit for percussion drilling with picosecond laser pulses. *Opt Express* 2018;26:11546. <https://doi.org/10.1364/OE.26.011546>.
- [71] Beard MC, Turner GM, Schmuttenmaer CA. Terahertz Spectroscopy. *J Phys Chem B* 2002;106:7146–59. <https://doi.org/10.1021/jp020579i>.
- [72] Kadlec C, Kadlec F, Kužel P, Blary K, Mounaix P. Materials with on-demand refractive indices in the terahertz range. *Opt Lett* 2008;33:2275. <https://doi.org/10.1364/ol.33.002275>.
- [73] Ting C-J, Chen C-F, Chou CP. Antireflection subwavelength structures analyzed by using the finite difference time domain method. *Optik (Stuttg)* 2009;120:814–7. <https://doi.org/10.1016/j.ijleo.2008.03.011>.
- [74] Ito K, Ito R, Yu X, Bessho M, Bae J. Signal Combining of one Dimensional Photoconductive Antenna Array Using a Metal. 64th JSAP Spring Meet., 2017, p. 14p-211–4.
- [75] Ito K, Bae J. Theoretical Consideration of Circuits used for Efficient Conversion from Static Electric Fields to Terahertz Waves. 76th JSAP Autumn Meet., 2015, p. 16p-2J – 3.
- [76] Horita N, Yu X, Takeuchi M, Ono S, Bae J. Anti-reflection Characteristics of Laser Drilling Subwavelength Tapered Structures at Terahertz Frequencies. 2018 43rd Int. Conf. Infrared, Millimeter, Terahertz Waves, vol. 2018- Septe, IEEE; 2018, p. 1–2. <https://doi.org/10.1109/IRMMW-THz.2018.8510489>.

- [77] Yu X, Horita N, Takeuchi M, Sudo M, Ono S, Bae J. Studying of Thermal Influence for Improving Anti-Reflective Characteristics of Moth-Eye Structures Fabricated by Femtosecond Laser Processing. 2018 43rd Int. Conf. Infrared, Millimeter, Terahertz Waves, vol. 2018- Septe, IEEE; 2018, p. 1–2. <https://doi.org/10.1109/IRMMW-THz.2018.8510112>.
- [78] Özgür Ü, Alivov YI, Liu C, Teke A, Reshchikov MA, Doğan S, et al. A comprehensive review of ZnO materials and devices. *J Appl Phys* 2005;98:1–103. <https://doi.org/10.1063/1.1992666>.
- [79] Series S. Transparent Conductive Zinc Oxide. vol. 104. Berlin, Heidelberg: Springer Berlin Heidelberg; 2008. <https://doi.org/10.1007/978-3-540-73612-7>.
- [80] Look DC, Claflin B, Alivov YI, Park SJ. The future of ZnO light emitters. *Phys Status Solidi C Conf* 2004;1:2203–12. <https://doi.org/10.1002/pssa.200404803>.
- [81] Khokhra R, Bharti B, Lee H-N, Kumar R. Visible and UV photo-detection in ZnO nanostructured thin films via simple tuning of solution method. *Sci Rep* 2017;7:15032. <https://doi.org/10.1038/s41598-017-15125-x>.
- [82] Adler BL, DeLeo VA. Sunscreen Safety: a Review of Recent Studies on Humans and the Environment. *Curr Dermatol Rep* 2020;9. <https://doi.org/10.1007/s13671-020-00284-4>.
- [83] Vecht A, Gibbons C, Davies D, Jing X, Marsh P, Ireland T, et al. Engineering phosphors for field emission displays. *J Vac Sci Technol B Microelectron Nanom Struct* 1999;17:750. <https://doi.org/10.1116/1.590633>.
- [84] Seager CH, Warren WL, Tallant DR. Electron-beam-induced charging of phosphors for low voltage display applications. *J Appl Phys* 1997;81:7994–8001. <https://doi.org/10.1063/1.365403>.
- [85] Ono S, Murakami H, Quema A, Diwa G, Sarukura N, Nagasaka R, et al. Generation of terahertz radiation using zinc oxide as photoconductive material excited by ultraviolet pulses. *Appl Phys Lett* 2005;87:1–3. <https://doi.org/10.1063/1.2158514>.
- [86] Kim Y, Ahn J, Kim BG, Yee DS. Terahertz birefringence in zinc oxide. *Jpn J Appl Phys* 2011;50:2–4. <https://doi.org/10.1143/JJAP.50.030203>.
- [87] Li G, Mikhaylovskiy R V., Grishunin KA, Costa JD, Rasing T, Kimel A V. Laser induced THz emission from femtosecond photocurrents in Co/ZnO/Pt and Co/Cu/Pt multilayers. *J Phys D Appl Phys* 2018;51. <https://doi.org/10.1088/1361-6463/aaab8f>.
- [88] ONO S, SARUKURA N, FUKUDA T. Generation of Terahertz Radiation Using Zinc Oxide as Photoconductive Material. *Rev Laser Eng* 2011;39:203–6. <https://doi.org/10.2184/ljsj.39.203>.
- [89] Umezawa R, Nagasaka R, Cadatal M, Ono S, Sarukura N, Ichikawa Y. Terahertz-radiation photoconductive antenna in sputtered zinc oxide thin film. *Jpn J Appl Phys* 2009;48:030209. <https://doi.org/10.1143/JJAP.48.030209>.
- [90] Yu X, Cadatal-Raduban M, Kato S, Kase M, Ono S. Femtosecond PLD-grown YF₃ nanoparticle thin films as improved filterless VUV photoconductive detectors. *Nanotechnology* 2021;32:015501. <https://doi.org/10.1088/1361-6528/abb84e>.
- [91] Yu X, Kato S, Ito H, Ono S, Kase M, Cadatal-Raduban M. Filterless tunable photoconductive ultraviolet radiation detector using CeF₃ thin films grown by pulsed laser deposition. *AIP Adv* 2020;10:045309. <https://doi.org/10.1063/1.5140827>.
- [92] Mans T, Dolkemeyer J, Schnitzler C. High Power Femtosecond Lasers. *Laser Tech J* 2014;11:40–3. <https://doi.org/10.1002/latj.201400031>.
- [93] Bernard O, Audouard E, Schöps B, Delaigue M, Dalla-Barba G, Mishchik K, et al. Efficient micro processing with high power femtosecond lasers by beam engineering and modelling. *Procedia CIRP* 2018;74:310–4. <https://doi.org/10.1016/j.procir.2018.08.121>.
- [94] Huang M, Xu Z. Spontaneous scaling down of femtosecond laser-induced apertures towards the 10-nanometer level: The excitation of quasistatic surface plasmons. *Laser Photonics Rev* 2014;8:633–52. <https://doi.org/10.1002/lpor.201300212>.
- [95] Liu J, Jia T, Zhou K, Feng D, Zhang S, Zhang H, et al. Direct writing of 150 nm gratings and squares on ZnO crystal in water by using 800 nm femtosecond laser. *Opt Express*

- 2014;22:32361. <https://doi.org/10.1364/oe.22.032361>.
- [96] Tull BR, Carey JE, Mazur E, McDonald JP, Yalisove SM. Silicon surface morphologies after femtosecond laser irradiation. *MRS Bull* 2006;31:626–33. <https://doi.org/10.1557/mrs2006.160>.
- [97] Yu X, Sudo M, Itoigawa F, Ono S. Patterning Oxidation via Femtosecond Laser Irradiation on Copper Substrate. *CLEO Pacific Rim Conf.*, Washington, D.C.: OSA; 2018, p. W3A.93. <https://doi.org/10.1364/CLEOPR.2018.W3A.93>.
- [98] Pereira A, Cros A, Delaporte P, Georgiou S, Manousaki A, Marine W, et al. Surface nanostructuring of metals by laser irradiation: Effects of pulse duration, wavelength and gas atmosphere. *Appl Phys A Mater Sci Process* 2004;79:1433–7. <https://doi.org/10.1007/s00339-004-2804-x>.
- [99] Liu JM. Simple technique for measurements of pulsed Gaussian-beam spot sizes. *Opt Lett* 1982;7:196. <https://doi.org/10.1364/OL.7.000196>.
- [100] Khosrofian JM, Garetz BA. Measurement of a Gaussian laser beam diameter through the direct inversion of knife-edge data. *Appl Opt* 1983;22:3406. <https://doi.org/10.1364/ao.22.003406>.
- [101] Ben-Yakar A, Byer RL. Femtosecond laser ablation properties of borosilicate glass. *J Appl Phys* 2004;96:5316–23. <https://doi.org/10.1063/1.1787145>.
- [102] Xu S, Qiu J, Jia T, Li C, Sun H, Xu Z. Femtosecond laser ablation of crystals SiO₂ and YAG. *Opt Commun* 2007;274:163–6. <https://doi.org/10.1016/j.optcom.2007.01.079>.
- [103] Sven Döring. *Analysis of the Hole Shape Evolution in Ultrashort Pulse Laser Drilling*. 2014.
- [104] Bäuerle D. *Laser Processing and Chemistry*. Berlin, Heidelberg: Springer Berlin Heidelberg; 2011. <https://doi.org/10.1007/978-3-642-17613-5>.
- [105] Vivas MG, Shih T, Voss T, Mazur E, Mendonca CR. Nonlinear spectra of ZnO: reverse saturable, two- and three-photon absorption. *Opt Express* 2010;18:9628. <https://doi.org/10.1364/oe.18.009628>.
- [106] He J, Qu Y, Li H, Mi J, Ji W. Three-photon absorption in ZnO and ZnS crystals. *Opt Express* 2005;13:9235. <https://doi.org/10.1364/OPEX.13.009235>.
- [107] Boyd R. *Nonlinear Optics*. 3rd Editio. 2008.
- [108] Yates B, Cooper RF, Kreitman MM. Low-temperature thermal expansion of zinc oxide. Vibrations in zinc oxide and sphalerite zinc sulfide. *Phys Rev B* 1971;4:1314–23. <https://doi.org/10.1103/PhysRevB.4.1314>.
- [109] Ibach H. Thermal Expansion of Silicon and Zinc Oxide (II). *Phys Status Solidi* 1969;31:625–34. <https://doi.org/10.1002/pssb.19690310224>.
- [110] CrysTec GmbH 2012. <http://www.crystec.de/datasheets-e.html> (accessed March 21, 2021).
- [111] Emerson et al. Led package with increased feature sizes. US 20100252851A1, n.d.
- [112] Britt et al. Light emitter devices and methods with reduced dimensions and improved light output. US10008637B2, n.d.
- [113] Wu X, Lee J, Varshney V, Wohlwend JL, Roy AK, Luo T. Thermal Conductivity of Wurtzite Zinc-Oxide from First-Principles Lattice Dynamics-a Comparative Study with Gallium Nitride OPEN. *Nat Publ Gr* 2016. <https://doi.org/10.1038/srep22504>.
- [114] Hull R. *Properties of Crystalline Silicon* 1999:1016.
- [115] Middelman T, Walkov A, Bartl G, Schödel R. Thermal expansion coefficient of single-crystal silicon from 7 K to 293 K. *Phys Rev B* 2015;92:174113. <https://doi.org/10.1103/PhysRevB.92.174113>.
- [116] Shanks HR, Maycock PD, Sidles PH, Danielson GC. Thermal Conductivity of Silicon from 300 to 1400°K. *Phys Rev* 1963;130:1743–8. <https://doi.org/10.1103/PhysRev.130.1743>.
- [117] Guo L, Yang S, Yang C, Yu P, Wang J, Ge W, et al. Highly monodisperse polymer-capped ZnO nanoparticles: Preparation and optical properties. *Appl Phys Lett* 2000;76:2901–3. <https://doi.org/10.1063/1.126511>.
- [118] Lin B, Fu Z, Jia Y, Liao G. Defect Photoluminescence of Undoping ZnO Films and Its Dependence on Annealing Conditions. *J Electrochem Soc* 2001;148:G110.

- <https://doi.org/10.1149/1.1346616>.
- [119] Lin B, Fu Z, Jia Y. Green luminescent center in undoped zinc oxide films deposited on silicon substrates. *Appl Phys Lett* 2001;79:943–5. <https://doi.org/10.1063/1.1394173>.
- [120] Zhang SB, Wei SH, Zunger A. Intrinsic n-type versus p-type doping asymmetry and the defect physics of ZnO. *Phys Rev B - Condens Matter Mater Phys* 2001;63:1–7. <https://doi.org/10.1103/PhysRevB.63.075205>.
- [121] Shan FK, Liu GX, Lee WJ, Lee GH, Kim IS, Shin BC. Aging effect and origin of deep-level emission in ZnO thin film deposited by pulsed laser deposition. *Appl Phys Lett* 2005;86:221910. <https://doi.org/10.1063/1.1939078>.
- [122] Wang ZG, Zu XT, Zhu S, Wang LM. Green luminescence originates from surface defects in ZnO nanoparticles. *Phys E Low-Dimensional Syst Nanostructures* 2006;35:199–202. <https://doi.org/10.1016/j.physe.2006.07.022>.
- [123] Ou Q, Matsuda T, Mesko M, Ogino A, Nagatsu M. Cathodoluminescence property of ZnO nanophosphors prepared by laser ablation. *Jpn J Appl Phys* 2008;47:389–93. <https://doi.org/10.1143/JJAP.47.389>.
- [124] Zeng H, Duan G, Li Y, Yang S, Xu X, Cai W. Blue luminescence of ZnO nanoparticles based on non-equilibrium processes: Defect origins and emission controls. *Adv Funct Mater* 2010;20:561–72. <https://doi.org/10.1002/adfm.200901884>.
- [125] Camarda P, Messina F, Vaccaro L, Agnello S, Buscarino G, Schneider R, et al. Luminescence mechanisms of defective ZnO nanoparticles. *Phys Chem Chem Phys* 2016;18:16237–44. <https://doi.org/10.1039/c6cp01513a>.
- [126] Shalish I, Temkin H, Narayanamurti V. Size-dependent surface luminescence in ZnO nanowires. *Phys Rev B - Condens Matter Mater Phys* 2004;69:1–4. <https://doi.org/10.1103/PhysRevB.69.245401>.
- [127] Provisional Final Acts of World Radiocommunication Conference 2019. 2019.
- [128] The Next Hyper Connected Experience for All. 2020.
- [129] Giordani M, Polese M, Mezzavilla M, Rangan S, Zorzi M. Toward 6G Networks: Use Cases and Technologies. *IEEE Commun Mag* 2020;58:55–61. <https://doi.org/10.1109/MCOM.001.1900411>.
- [130] Alsharif MH, Kelechi AH, Albream MA, Chaudhry SA, Sultan Zia M, Kim S. Sixth generation (6G) wireless networks: Vision, research activities, challenges and potential solutions. *Symmetry (Basel)* 2020;12. <https://doi.org/10.3390/SYM12040676>.
- [131] Perrie W, Gill M, Robinson G, Fox P, O’Neill W. Femtosecond laser micro-structuring of aluminium under helium. *Appl Surf Sci* 2004;230:50–9. <https://doi.org/10.1016/j.apsusc.2003.12.035>.
- [132] Pozar DM. *Microwave Engineering*. 4th ed. John Wiley & Sons; 2011.
- [133] Soeda J, Kawada Y, Satozono H, Takahashi H, Chokai M, Ikeda Y. Broadband Anti-Reflection coating for THz waves developed with Si nanoparticle-polymer composite material. 2020 45th Int. Conf. Infrared, Millimeter, Terahertz Waves, vol. 39, IEEE; 2020, p. 1–1. <https://doi.org/10.1109/IRMMW-THz46771.2020.9370466>.

Acknowledgments

First of all, I would like to express sincere gratitude to associate professor Shingo Ono for his guidance throughout this research and for providing the chance to study at Nagoya Institute of Technology (NIT). From him, I learn not only scientific things such as experiments, presentations, and manuscripts, but also how to work and consider as a researcher. Most of all, the trust relationship between us made me possible to solve lots of difficult problems in this work. As an international student, I must overcome the language barrier for studying and daily life in Japan. Ono sensei always showed enough patience in the conversation between us when I was trapped in Japanese, and he also helps me improve my speaking and writing skills in Japanese. I want to thank professor Jongsuck Bae for his brilliant insights and support made this work possible and made me feel very rewarding during my doctoral tenure. Although Bae sensei retired from NIT in the second year of my doctorate course, he always kindly answered my questions rapidly. I also want to thank Professor Itoigawa for his helpful discussions from a view of mechanical engineering, and he also provides a lot of convenience for the experiment instruments throughout my doctor course.

I would like to offer my token of appreciation to associate professor Takashi Kimura and professor Katsuyoshi Ikeda in NIT, for their careful reviews, worthy comments, and beneficial advice, which brought great improvement to this thesis. I would like to thank Mr. Kazuhisa Mikame and Mr. Nobuhito Takizawa in Tamari Industry Co., LTD for their help with the experiment and discussion in the work of chapters 2 and 4. It is my great pleasure to acknowledge professor Dr. Satoru Tsuchikawa, associate professor Dr. Tetsuya Inagaki, and Ms. Han Wang for their help with the THz-TDS measurements and their fruitful discussions for works in chapters 3–5, as well as some other unpublished works. I also want to thank Dr. Junshi Soeda for providing their coating technology and help in fabricating the hybrid AR structure which showed the best AR performance of this thesis.

I would like to acknowledge Hirose Foundation (ヒロセ財団), Banbuntane Hotokukai (伴文種報徳会), Japan Student Services Organization (JASSO, 日本学生支援機構) for their financial support for research and daily life during my study in Japan. I also want to say thanks to those lovely people who belong to ONOlab from 2014 to 2021. They helped me get used to the Japanese culture, which is very strong support to me to smoothly finish this Ph.D. course. These people not just helped me solve lots of daily problems, they also taught me how to understand Japanese culture and language. These can still support me for the rest of my journey in Japan. I would like to express my appreciation to Mr. Wang Zhang's family for their support to me and my family from the day I came to Japan.

Most of all, special gratitude is owed to my parents, wife, and son, who always gave me endless love and spiritual strength during the education. I could not finish this research work and get a Ph.D. degree without your contributions.

Xi Yu
April 2021
NIT, Nagoya

Publication List

Paper with peer review

- [1] Dejun Liu, **Xi Yu**, Feng Wu, Shuyuan Xiao, Fumihiro Itoigawa, Shingo Ono, “Terahertz high-Q quasi bound states in the continuum in laser-fabricated metallic resonators based on double-slit arrays”, *Optics Express*, under review
- [2] **Xi Yu**, Kazusa Goto, Yuki Yasunaga, Junshi Soeda, Shingo Ono, “Polymer-coated moth-eye hybrid structure for broadband antireflection in the terahertz region”, *Optics Letters*, submitted (**chapter 5 of this dissertation**)
- [3] **Xi Yu**, Fumihiro Itoigawa, Shingo Ono, “Femtosecond laser-pulse-induced surface cleavage of zinc oxide substrate”, *Micromachines* **12**, 596(2021) (**chapter 3 of this dissertation**)
- [4] **Xi Yu**, Yuki Yasunaga, Kazusa Goto, Dejun Liu, Shingo Ono, “Profile control of femtosecond laser-fabricated moth-eye structures on Si substrate”, *Optics and Lasers in Engineering* **142**, 106584, (2021) (**chapter4 of this dissertation**)
- [5] **Xi Yu**, Marilou Cadatal-Raduban, Seiya Kato, Masahiko Kase, and Shingo Ono, “Femtosecond PLD-grown YF₃ nanoparticle thin films as improved filterless VUV photoconductive detectors”, *Nanotechnology* **32**, 015501(2020)
- [6] **Xi Yu**, Seiya Kato, Shingo Ono, Masahiko Kase, Marilou Cadatal-Raduban, “Filterless tunable photoconductive ultraviolet radiation detector using CeF₃ thin films grown by pulsed laser deposition”, *AIP Advances* **10**, 045309 (2020)
- [7] **Xi Yu**, Michiharu Ohta, Nobuhito Takizawa, Kazuhisa Mikame, Shingo Ono, and Jongsuck Bae, “Femtosecond-laser-fabricated periodic tapered structures on a silicon substrate for terahertz antireflection”, *Applied Optics* **58**, pp. 9595-9602(2019) (**chapter 2 of this dissertation**)
- [8] **Xi Yu**, Miho Tanaka, Kohei Toyama, Shusaku Terakawa, Shingo Ono, Masaaki Sudo, Kentaro Fukuda, Yoshiki Makino, Takafumi Hirata, “Evaluation of Ce³⁺: LiCaAlF₆ single crystal by Multi-Photon Luminescence Measurement”, *Optical Materials* **86**, pp. 394-397 (2018)
- [9] **Xi Yu**, Shusaku Terakawa, Shunsuke Hayashi, Toru, Asaka, Fumihiro Itoigawa, Shingo Ono, Jun Takayanagi, “Carbonization of Silicon Nanoparticles via Ablation Induced by Femtosecond Laser Pulses in Hexane”, *Arabian Journal for Science and Engineering* **42**, pp. 4421-4226 (2017)

International Conference

(*: Presenter)

- [1] Shingo Ono, Miho Tanaka, **Xi Yu***, Kentaro Fukuda, Shunsuke Kurosawa, “Evaluation of Scintillator Single Crystal by Multi-photon Luminescence and LA-

- ICPMS”, Akira Yoshikawa, NMS-XII 2016, IL31-J, 14-19 October 2016, Changsha, China (**Oral, invited**)
- [2] **Xi Yu***, Shunsuke Hayashi, Fumihito Itoigawa, Shingo Ono, Jun Takayanagi, “Carbonization of Silicon Nanoparticles by Ablation of Femtosecond Laser Pulses in Hexane”, NMS-XII 2016, P28, 14-19 October 2016, Changsha, China (**Poster**)
- [3] Shingo Ono*, Miho Tanaka, **Xi Yu**, Kentaro Fukuda, Shunsuke Kurosawa, Akira Yoshikawa, “Evaluation of Optical Crystals by Multi-photon Luminescence”, EMN 3CG & Metallic Glasses Meeting 2017, A06, 7-11 August 2017, Berlin, Germany (**Oral, invited**)
- [4] **Xi Yu***, Mahiro Takeuchi, Masaaki Sudo, Shingo Ono, Jongsuck Bae, “Fabrication of THz Antireflective Structures on Silicon Substrates by Femtosecond Laser”, IUMRS-ICAM 2017, B6-O28-012, August 27-September 1, Kyoto, Japan (**Oral, Awarded**)
- [5] **Xi Yu***, Shusaku Terakawa, Toru Asaka, Fumihito Itoigawa, Shingo Ono, Masaaki Sudo, “Synthesis of Silicon Carbide Nanoparticles by Femtosecond Laser Ablation of Silicon in Hexane”, IUMRS-ICAM 2017, C5-P31-004, August 27-September 1, Kyoto, Japan (**Poster**)
- [6] Shusaku Terakawa*, **Xi Yu**, Toru Asaka, Fumihito Itoigawa, Shingo Ono, “Fabrication of Molybdenum Carbide Nanoparticles by Femtosecond Laser Ablation of Molybdenum in Hexane”, Masaaki Sudo, IUMRS-ICAM 2017, C5-O31-006, August 27-September 1, Kyoto, Japan (**Oral**)
- [7] **Xi Yu***, Mahiro Takeuchi, Shingo Ono, Jongsuck Bae, “THz Antireflective Structures Fabricated by Femtosecond Laser Processing”, The 7th Advanced Lasers and Photon Sources, ALPS11-G2-4, 17-24 April 2018, Yokohama, Japan (**Oral**)
- [8] **Xi Yu***, Masaaki Sudo, Fumihito Itoigawa, Shingo Ono, “Patterning Oxidation of Copper Substrate by Femtosecond Laser Irradiation”, The 7th Advanced Lasers and Photon Sources, ALPSp-14, 17-24 April 2018, Yokohama, Japan (**Poster**)
- [9] **Xi Yu***, Mahiro Takeuchi, Shingo Ono, Jongsuck Bae, “Terahertz Antireflective Structures Fabricated via Femtosecond Laser Ablation”, The 13th Pacific Rim Conference on Lasers and Electro-Optics, W3A.66, July 29-3 August 2018, HongKong, China (**Poster**)
- [10] **Xi Yu***, Masaaki Sudo, Fumihito Itoigawa, Shingo Ono, “Patterning Oxidation via Femtosecond Laser Irradiation on Copper Substrate”, The 13th Pacific Rim Conference on Lasers and Electro-Optics, W3A.93, July 29-August 3 2018, HongKong, China (**Poster**)
- [11] Naoki Horita*, **Xi Yu**, Mahiro, Takeuchi, Shingo Ono, Jongsuck Bae, “Anti-reflection Characteristics of Laser Drilling Subwavelength Tapered Structures at Terahertz Frequencies”, 43rd International Conference on Infrared, Millimeter and Terahertz Waves, Tu-POS-61, 9-14 September 2018, Nagoya, Japan (**Poster**)

- [12] **Xi Yu***, Naoki Horita, Mahiro Takeuchi, Masaaki Sudo, Shingo Ono, Jongsuck Bae, “Studying of Thermal Influence for Improving Anti-Reflective Characteristics of Moth-Eye Structures Fabricated by Femtosecond Laser Processing”, 43rd International Conference on Infrared, Millimeter and Terahertz Waves, Tu-POS-62, 9-14 September 2018, Nagoya, Japan (**Poster**)
- [13] **Xi Yu***, Naoki Horita, Motoki Bessho, Masaaki Sudo, Shingo Ono, Jongsuck Bae, “Shape dependence of anti-reflective characteristic of terahertz moth-eye structures fabricated by femtosecond laser processing”, SPIE Photonics West 2019, 10906-55, 2-7 February 2019, San Francisco, United States (**Poster**)
- [14] **Xi Yu***, Shusaku Terakawa, Masaaki Sudo, Toru Asaka, Fumihito Itoigawa, Shingo Ono, “Carbide nanoparticles fabrication of silicon and molybdenum by femtosecond laser ablation in hexane”, SPIE Photonics West 2019, 10906-56, 2-7 February 2019, San Francisco, United States (**Poster**)
- [15] **Xi Yu***, Seiya Kato, Shingo Ono, Michiharu Ota, Nobuhito Takizawa, Kazuhisa Mikame, “Terahertz Tapered Antireflective Structures Fabricated by Femtosecond Laser Processing”, The 8th International Congress on Laser Advanced Materials Processing, Th1-L13, 21-24 May 2019, Hiroshima, Japan (**Oral**)
- [16] **Xi Yu***, Michiharu Ota, Fumihito Itoigawa, Shingo Ono, “Micro-pattern Oxidation of Copper by Femtosecond Laser Direct Writing”, The 8th International Congress on Laser Advanced Materials Processing, P-LPM33, 21-24 May 2019, Hiroshima, Japan (**Poster**)
- [17] **Xi Yu***, Hiroyuki Kawai, Fumihito Itoigawa, Shingo Ono. Nobuhito Takizawa, Kazuhisa Mikame, “Femtosecond Laser Dimpling on SUS Substrate for Improving Tribological Properties”, The 8th International Congress on Laser Advanced Materials Processing, P-LPM15, 21-24 May 2019, Hiroshima, Japan (**Poster**)
- [18] Yoshiki Tanaka*, Shusaku Terakawa, **Xi Yu**, Toru Asaka, Michiharu Ota, Fumihito Itoigawa, Shingo Ono, “Fabrication of Molybdenum Carbide Nanoparticles by Femtosecond Laser Ablation in Hexane”, The 8th International Congress on Laser Advanced Materials Processing, FrM-L4, 21-24 May 2019, Hiroshima, Japan (**Oral**)
- [19] Yoshiki Tanaka*, Masato Hishiki, Taihei Watanabe, **Xi Yu**, Michiharu Ota, Fumihito Itoigawa, Shingo Ono, “Control of Wettability by microstructure fabrication on carbon surface with femtosecond laser”, The 8th International Congress on Laser Advanced Materials Processing, P-LPM30, 21-24 May 2019, Hiroshima, Japan (**Poster**)
- [20] **Xi Yu***, Jongsuck Bae, Shingo Ono, “Profile Control of One-dimensional Terahertz Moth-eye Structure Fabricated by Femtosecond Laser Processing”, The 44th International Conference on Infrared, Millimeter and Terahertz Waves, Tu-Po2-37, 1-6 September 2019, Paris, France (**Poster**)
- [21] **Xi Yu***, Shingo Ono, Jongsuck Bae, “Application of Laser Generated Moth-eye Structure for A Periodic Terahertz-wave Generator”, The 44th International

Domestic conferences

- [1] 竹内 真皓*、余 希、伊藤 亮祐、伊藤 圭介、小野 晋吾、裴 鐘石，“超短パルスレーザー加工によるテラヘルツ帯反射防止構造の評価”，**Evaluation of THz antireflective structures fabricated by ultrashort pulse laser ablation**，第 77 回応用物理学会秋季学術講演会，**16a-B2-5**，2016 年 9 月 13 日（火）~16 日（金），朱鷺メッセ、新潟市(口頭)
- [2] 余 希*、寺川 周作、浅香 透、糸魚川 文広、小野 晋吾、須藤 正明，“ヘキサシアン中 Si のレーザーアブレーションによる SiC ナノ粒子の合成”，第 5 回応用物理学会名古屋大学学生チューデントチャプター東海地区学術講演会，**PA26**，2017 年 10 月 28 日（土）~29 日（日），名古屋大学 IB 電子情報館、名古屋(ポスター)
- [3] 余 希*、竹内 真皓、小野 晋吾、裴 鐘石，“フェムト秒レーザー加工によるテラヘルツ波反射防止構造の作製”，平成 29 年度レーザー学会中部支部若手研究発表会，**9**，2017 年 12 月 1 日（金），静岡大学、浜松市(口頭)
- [4] 余 希*、堀田 尚輝、須藤 正明、小野 晋吾、裴 鐘石，“フェムト秒レーザー加工による作製したモスアイ型 THz 反射防止構造の特性向上”，第 79 回応用物理学会秋季学術講演会，**20p-212A-11**，2018 年 9 月 18 日~21 日，名古屋国際会議場、名古屋(口頭)
- [5] 余 希*、須藤 正明、糸魚川 文広、小野 晋吾，“フェムト秒レーザー照射による Cu 基板表面のパターニング酸化”，第 79 回応用物理学会秋季学術講演会，**19a-PA4-4**，2018 年 9 月 18 日~21 日，名古屋国際会議場、名古屋(ポスター)
- [6] 寺川 周作*、余 希、浅香 透、糸魚川 文広、小野 晋吾、須藤 正明，“ヘキサシアン中レーザーアブレーションによる炭化モリブデンナノ粒子作製”，第 79 回応用物理学会秋季学術講演会，**18p-136-13**，2018 年 9 月 18 日~21 日，名古屋国際会議場、名古屋(口頭)
- [7] 日紫喜 雅人*、余 希、須藤 正明、糸魚川 文広、小野 晋吾，“モリブデン表面におけるフェムト秒レーザー誘起微細構造の作製”，第 79 回応用物理学会秋季学術講演会，**19a-PA4-2**，2018 年 9 月 18 日~21 日，名古屋国際会議場、名古屋(ポスター)
- [8] 余 希*、田中 良樹、三瓶 和久、滝沢 宣人、糸魚川 文広、小野 晋吾，“モスアイ型 THz 反射防止構造の断面形状制御”，第 80 回応用物理学会秋季学術講演会，**19a-PA2-2**，2019 年 9 月 18 日~21 日，北海道大学、札幌市(ポスター)

Awards and Funding

Awards

- [1] 2021/3, Vice-president's Award for Students in 2020
- [2] 2020/3, President's Award for Students in 2019
- [3] 2019/3, President's Award for Students in 2018
- [4] 2018/3, Vice-president's Award for Students in 2017
- [5] 2017/11, Award for Encouragement of Research in IUMRS-ICAM 2017 Symposium B-6

Funding

- [1] 2018-2019 The Sasakawa Scientific Research Grant (No. 2018-2031) from the Japan Science Society (790,000 JPY), Title: Fabrication of moth-eye structure for terahertz waves by ultrafast laser processing